

Label-free Biodetection with Individual Plasmonic Nanoparticles

by

Gregory J. Nusz

Department of Biomedical Engineering  
Duke University

Date: \_\_\_\_\_

Approved:

\_\_\_\_\_  
Ashutosh Chilkoti, Supervisor

\_\_\_\_\_  
Adam P. Wax

\_\_\_\_\_  
David J. Brady

\_\_\_\_\_  
Anne Lazarides

\_\_\_\_\_  
William Reichert

\_\_\_\_\_  
David R. Smith

Dissertation submitted in partial fulfillment of  
the requirements for the degree of Doctor of Philosophy in the Department of  
Biomedical Engineering in the Graduate School  
of Duke University

2010

ABSTRACT

Label-free Biodetection with Individual Plasmonic Nanoparticles

by

Gregory J. Nusz

Department of Biomedical Engineering  
Duke University

Date: \_\_\_\_\_

Approved: \_\_\_\_\_

\_\_\_\_\_  
Ashutosh Chilkoti, Supervisor

\_\_\_\_\_  
Adam P. Wax

\_\_\_\_\_  
David J. Brady

\_\_\_\_\_  
Anne Lazarides

\_\_\_\_\_  
William Reichert

\_\_\_\_\_  
David R. Smith

An abstract of a dissertation submitted in partial fulfillment of the requirements for the degree of Doctor of Philosophy in the Department of Biomedical Engineering in the Graduate School of Duke University

2010

Copyright by  
Gregory J. Nusz  
2010

## **Abstract**

The refractive index sensitivity of plasmonic nanoparticles is utilized in the development of real-time, label-free biodetection. Analyte molecules that bind to receptor-conjugated nanoparticles cause an increase in local refractive index that in turn induces an energy shift in the optical resonance of the particle. Biomolecular binding is quantified by quantitatively measuring these resonance shifts. This work describes the application and optimization of a biomolecular detection system based on gold nanorods as an optical transducer.

A microspectroscopy system was developed to collect scattering spectra of single nanoparticles, and measure shifts of the spectra as a function of biomolecular binding. The measurement uncertainty of LSPR peak shifts of the system was demonstrated to be 0.3 nm. An analytical model was also developed that provides the optimal gold nanorod geometry for detection with specified receptor-analyte pair. The model was applied to the model biotin-streptavidin system, which resulted in sensing system with a detection limit of 130 pM – an improvement by four orders of magnitude over any other single-particle biodetection previously presented in the literature.

Alternative optical detection schemes were also investigated that could facilitate multiplexed biosensing. A theoretical model was built to investigate the efficacy of using a multi-channel detector analogous to a conventional RGB camera. The results of the model indicated that even in the best case, the detection capabilities of such a system did not provide advantages over the microspectroscopic approach.

We presented a novel hyperspectral detection scheme we term Dual-Order Spectral Imaging (DOSI) which is capable of simultaneously measuring spectra of up to

160 individual regions within a microscope's field of view. This technique was applied to measuring shifts of individual nanoparticles and was found to have a peak measurement uncertainty of 1.29 nm, at a measurement rate of 2-5 Hz.

## **Dedication**

This work is dedicated to Dr. Hans Hallen and Dr. Eric Ayars for showing me into the world of scientific research, and to my parents Tom and Elaine for never telling me what to be when I grow up.

# Contents

Abstract .....	iv
List of Tables .....	xi
List of Figures .....	xii
Acknowledgements .....	iv
1 Background on Biomolecular Detection .....	1
1.1 Label-free Sensors .....	1
1.1.1 Acoustic Transduction .....	3
1.1.2 Microelectromechanical Sensors .....	4
1.1.3 Electrochemical Transduction .....	4
1.1.4 Optical Transduction .....	5
1.1.4.1 Surface Enhanced Raman Scattering .....	5
1.1.4.2 Surface Plasmon Resonance .....	6
1.1.4.3 Localized Surface Plasmon Resonance .....	9
1.2 LSPR Biosensing .....	9
1.2.1 Operating Principles .....	9
1.2.2 Comparison with SPR .....	12
1.2.3 Application/Fabrication .....	18
1.2.3.1 Chemical Synthesis .....	19
1.2.3.2 Top-Down Lithography .....	21
1.2.3.3 Non-Specific Adsorption Prevention .....	22
1.3 Nanoparticle Detection .....	24
1.3.1 Ensemble Analysis .....	25

1.3.2 Single Nanostructure Analysis.....	28
1.3.3 Biodetection with Single Nanostructures.....	30
1.4 Plasmonic Imaging.....	31
2 Darkfield Microspectroscopy System.....	36
2.1 Experimental Preparation.....	36
2.1.1 Materials.....	36
2.1.2 Substrate Preparation.....	36
2.2 Darkfield Imaging.....	37
2.3 Microspectroscopy.....	41
2.3.1 System Description.....	41
2.3.2. Spectral Data Processing.....	42
2.3.3 Spectral Measurement Analysis.....	45
3 Gold Nanorod Biosensor.....	49
3.1 Sensor Fabrication and Detection Methods.....	50
3.1.1 Materials.....	50
3.1.2 Nanorod Synthesis.....	50
3.1.3 Substrate Preparation.....	51
3.1.4 Receptor Conjugation.....	52
3.1.5 Experimental Methods.....	52
3.2 Gold Nanorod Spectral Analysis.....	53
3.2.1 Bulk Refractive Index Sensitivity.....	54
3.2.2 Time-Resolved Spectroscopy.....	56
3.2.3 Polarization Dependence of Nanorod LSPR.....	57
3.3 Biodetection with Individual Gold Rods.....	59

3.3.1 Static Biodetection.....	60
3.3.2 Time-Resolved Biodetection.....	62
3.4 Conclusions.....	63
4 Gold Nanorod Optimization.....	65
4.1 Model Development.....	66
4.1.1 Estimation of minimum detectable LSPR shift.....	68
4.1.2 Quantification of Bound Molecules.....	71
4.1.3 Nanoparticle Geometry Dependence.....	73
4.1.3.1 Scattering Cross-Section.....	73
4.1.3.2 Distance Dependent Sensitivity.....	74
4.2 Complete Analytical Model.....	81
4.3 Experimental Application of Model.....	84
4.3.1 Quantitative Analysis of Molecular Detection Limit.....	86
4.3.2 Quantitative Analysis of Molecular Dynamic Range.....	88
4.4 Prospects for Single Molecule Detection.....	89
4.5 Significance of Results.....	94
5 Plasmonic Imaging.....	96
5.1 Multispectral Imaging.....	99
5.1.1 Preliminary Work: RGB Camera.....	100
5.1.2 Multispectral Imaging Simulation.....	103
5.1.2.1 Data Cube Generation.....	103
5.1.2.2 Detection Simulation.....	105
5.1.2.3 Calibration.....	106
5.1.2.4 Simulation Results.....	110

5.1.2.5 Discussion .....	114
5.2 Dual-Order Spectral Imaging.....	115
5.2.1 DOSI Technique Description .....	116
5.2.2 Experimental Results.....	120
5.2.3 Discussion and Implications .....	125
6 Conclusions and Future Directions .....	128
6.1 Conclusions.....	128
6.2 Future Directions.....	129
6.2.1 Transducer Considerations .....	129
6.2.2 DOSI Development .....	132
6.2.2.1 Multiplexed detection.....	132
6.2.2.2 DOSI Data Analysis.....	133
Appendix A.....	135
References.....	136
Biography .....	156

## List of Tables

Table 1. Theoretical improvement factors that can reduce the molecular detection limit of a label-free, single particle LSPR sensor .....	94
---	----

## List of Figures

Figure 1: Schematics of darkfield illumination techniques.....	39
Figure 2: Darkfield micrograph of 80 nm diameter gold spheres. ....	41
Figure 3: Illustration of intrinsic source correction.....	44
Figure 4: Normalized scattering spectra of the same 80 nm diameter gold sphere measured 30 times.....	45
Figure 5: TEM of gold nanorods used in the characterization of the microspectroscopy system.....	51
Figure 6: A) Darkfield micrograph of gold nanorods. B) Scattering spectra of an ensemble of gold nanorods on a glass substrate (blue) and of a single gold nanorod (red).....	53
Figure 7: Normalized scattering spectra of a single gold nanorod as the refractive index of the surrounding medium is changed .....	55
Figure 8: LSPR peak centroid of a single gold nanorod as the surrounding refractive index is increased incrementally every 20 minutes.....	57
Figure 9: Scattering spectra of a single nanorod exhibiting the polarization dependence of each resonance. ....	59
Figure 10: (a,b) Scattering spectra of a single gold nanorod after sequential incubation in EG3SH/MHA (c,d) Scattering spectra of a single gold nanorod in EG3SH/MHA (blue), biotin (red) and 100 nM streptavidin pre-saturated with free biotin (black). ....	62
Figure 11: Real-time measurement of the LSPR scattering peak centroid shifts of single biotin-conjugated gold nanorods .....	63
Figure 12: Comparison of simulated versus experimental spectra .....	74
Figure 13: Right axis - experimental wavelength shift of a nanorod ( $63.3 \pm 8.2$ nm x $24.9 \pm 4.9$ nm) as a function of deposited polyelectrolyte thickness (red dots) and shifts predicted by equation 7 (green line). Left axis - corresponding calculated distance dependence of the nanorod LSPR sensitivity (blue line).....	80
Figure 14: A) Calculated molecular limits of detection for gold nanorods of arbitrary dimension based on equation 4.17. ....	84
Figure 15: A) TEM of rods used in this study. ....	85

Figure 16: Fits to scattering spectra of a single nanorod in water (blue), after biotin conjugation (green), and subsequently in 100pM streptavidin (red). .....	87
Figure 17: A) Response curves for the red (R), green (G), and blue (B) channel of the CCD camera used to measure LSPR shifts of 60 nm gold nanospheres. B) Theoretically expected trend .....	101
Figure 18: A) RGB image of 60nm gold nanospheres in water. B) Blue squares denote the mean and standard deviations (blue error bars) of regression values of 60nm nanospheres (n~250) under 0, 40 and 80 percent glycerol in water.....	102
Figure 19: Model generated darkfield image.....	104
Figure 20: Simulation of detector response. ....	106
Figure 21: Shifts in CIELAB XYZ colorspace of nanorods with different resonance wavelengths. ....	108
Figure 22: A) False color image of a calibration image. B) Schematic illustration of how calibration images are applied .....	109
Figure 23: A) Probability density function of gold nanorods used in this study. B) Scattering spectra of 40 nanorods randomly selected from this geometry distribution. ....	111
Figure 24: Experimentally collected image (A) and simulated image (B) of gold nanorods at low coverage. High coverage experimental image (C) and simulation (D). ....	112
Figure 25: A) Regression results of the KLM filter scheme applied to simulated low coverage images of nanorods. B) Regression results from high coverage simulations .....	114
Figure 26: Raw DOSI micrograph of gold nanorods under darkfield illumination. ....	118
Figure 27: Zero-order (left) and first-order diffracted mode (right) of a source-corrected DOSI image.....	119
Figure 28: Line scan of a DOSI image. ....	122
Figure 29: DOSI spectra of two nanorods under five solutions with increasing refractive index.....	123
Figure 30: Mean peak shift recorded for DOSI imaging of gold nanorods as a function of refractive index.....	125

## Acknowledgements

My brother Jeff once mused (as he often does), that no one really "invents" anything new, they just figure out neat new ways to put already existing things together. In much the same way, my part in the work described in this thesis feels more like a node, drawing in the contributions of tons of other people. Which was nice, because in the end I didn't have to do too much work.

I'd like to thank Tosh for the trust he placed in me to do good work, and offering the freedom to explore the research as I saw fit. I'd also like to thank him for supporting my traveling habit while at Duke. While I realize that sending me to conference just makes good sense from an economic standpoint (what's an extra 2k for a ride to Switzerland to light a research-attaining fire under my ass, compared to my total cost as a grad student?), it did not have to be that way and I appreciate it. I also appreciate how he only scoffs a little bit when I mention I'm not going straight into academia.

More thanks to: Stella Marinakos for holding my hand at the lab bench and for answering all my questions that I asked three times before already, even though I have nothing to offer in return other than physical labor and Googling abilities when hands are gloved. The Tosh lab moto gang of Ryan Hill and Angus Hucknall. The Duke intramural sports program for keeping me on campus even more hours of the day. The Duke physical therapy team for keeping me healthy, active and therefore more sane. Kathy Barbour and Marianne Hassan for running the BME department. Fredrik Höök and his whole gang for showing me a good time and following me to pirate bars in Spain, Switzerland and in Sweden. Cristina Fernandez for working on all the CASSI stuff and asking for nothing in return (except my defense date). Doo Doo Brown, for always being

there for a game and a beer. And Josie Bamford who still claims she likes me even after I've spent the last entire month in solitary confinement compiling this literary treasure.

Enjoy.

# 1 Background on Biomolecular Detection

## 1.1 Label-free Sensors

In the development of biomolecular sensors, several attributes are considered that contribute to the overall effectiveness of the sensor. Of primary consideration are the detection limits and dynamic range of the sensor. The detection limit of a sensor is generally considered to be the minimum amount of target analyte required in a test sample for a statistically significant response to be generated. The dynamic range is the range of analyte concentrations over which statistically significant responses can be generated – that is, the range between the detection limit and sensor saturation. Robustness is also an essential characteristic of biosensors. A robust sensor is one that generates reproducible signals based only on detected analyte, avoiding false signals generated by non-specific interactions of non-target material. Another important consideration in the assessment of a biosensor is cost. This includes direct costs such as the detector instrumentation and per-use cost of consumables as well as indirect costs such as sample preparation and training requirements of the end-user. Finally, some characteristics that can add to the value of a sensor, but are not essential are parallelizability and addressability. A parallelizable sensor is one that can be readily adapted so that numerous detections can be performed concurrently. An addressable sensor is one that provides spatial resolution of biomolecular interactions in addition to the quantity.

Label-free sensors are one particular sub-class of biosensors that are characterized as those that generate their response directly from the presence of the target analyte. This is as opposed to a labeled detection system where a contrast agent, such as a fluorescent or radioactive reporter, is linked to the target. It is this

contrast agent that is detected by the sensor and is thus responsible for generating the system response. While labeled systems tend to be more sensitive as a whole, label-free systems offer several unique advantages especially in the detection of analytes in the food industry and medicine<sup>1-3</sup>. This is because label-free sensors avoid the process of chemically linking a labeling moiety to the biomolecule of interest. This process can potentially affect its conformational state potentially altering binding affinities and related kinetic rates in a manner that typically cannot be predicted beforehand. It is also possible that the attached label can sterically occlude the binding sight leading to false negatives. Further, false positives can be generated by the presence of nonspecifically bound labels adhering to the test substrate. In addition to avoiding this problem, label-free approaches do not require the lengthy preprocessing steps generally required to conjugate labels to the detection sample. This can reduce the cost of sensors by reducing sample preparation steps such as target-label conjugation, and also reduce potential error that can be introduced in these additional steps. This also enables label-free systems to be more suited to point-of-care medicine and for use in areas without access to demanding support infrastructure such as combat zones and developing nations. Additionally, a label-free approach offers the potential of multiplexed screening without significantly increasing the work load of the end-user. This is because the transduction modality is embedded in the sensor itself, and is not part of the sample processing steps.

In general, in a label-free biosensor the binding of the target analyte by the sensor is directly transduced to a measurable signal. Therefore, the development of a label-free sensor focuses on two primary areas: the means of transduction and the processing of the generated signal into a useful metric of analyte presence. In pursuit of

the goals listed above for a successful label-free sensor, many different transduction modalities have been investigated. The following section summarizes the most widely studied transduction modalities in the field of label-free biodetection with special emphasis on planar surface plasmon resonance as it has become the gold-standard in the field of label-free biosensing.

### **1.1.1 Acoustic Transduction**

Acoustic transduction schemes are those in which a vibrational mode of an oscillator is influenced by bound mass of target analyte. As the bound mass increases, the resonant frequency of the oscillator shifts. Thus, the measured quantity in such sensors is the change in resonant frequency. The quartz crystal microbalance (QCM) is the most common implementation of this transduction method. In QCM, a piezoelectric quartz crystal electrode is the oscillator. First developed and applied to biosensing in 1988<sup>4</sup>, more recent improvements of the technique allow for determination of the adsorbed material's viscosity as well as mass<sup>5</sup>. This is performed by observing the energy dissipation of the vibrational mode after the driving force is removed and is known as quartz crystal microbalance with dissipation (QCM-D). In addition to the providing viscosity measurements, which is a unique attribute of QCM-D among label free sensors, QCM-D also offers the distinct advantage that only material that is physically bound to the crystal surface is measured. This offers a degree of discrimination as compared to other label-free – principally optical– methods that typically detect the presence of any material close to the transducer and do not require that the material be physically bound to the substrate. QCM has been applied to the characterization of proteins<sup>6</sup>, oligonucleotides<sup>7</sup>, immunoassays<sup>8</sup> as well as many other biomolecular interactions<sup>9</sup>.

### **1.1.2 Microelectromechanical Sensors**

Another class of transduction schemes utilized for label-free biodetection is microelectrical mechanical systems (MEMS). While this label covers a wide range of devices, the most common deployed biosensors in this class are based on microcantilevers, which deflect or deform upon biomolecular interactions that occur on the surface of the microcantilever. Microcantilever systems have been demonstrated for antibody-antigen interactions<sup>10</sup>. An attractive attribute of MEMS-based systems is that they can be easily integrated into existing semiconductor fabrication techniques, allowing for on-chip integration of signal processing systems. Recently a MOSFET-embedded microcantilever biosensor was demonstrated<sup>11</sup>. Another advantage of MEMS-based systems is that in principle they require a very small amount and volume of target analyte for operation, so that cost of materials and the processing time can be reduced, as the processing time is typically controlled by the diffusion distance of the analyte to the receptor<sup>12</sup>.

### **1.1.3 Electrochemical Transduction**

Label-free electrochemical sensors are based on observed changes in an electric current or electric potential resulting from specific interactions at a transducer interface<sup>13</sup>. In a label-free configuration, they tend to be most successful in detection schemes involving molecular interactions that involve electron transfer such as chemical oxidation or by utilizing electroactive enzymes as a detector substrate, as demonstrated in the highly successful blood-glucose monitoring systems<sup>14</sup>. In typical immunosensors, however, there exists no direct electron exchange between the target analyte and its receptor, so that detection is generally indirect<sup>13</sup>. For example, recent electrochemical immunoassay systems have been developed that utilize enzyme-linked antibodies as

receptors that in turn generate an electrochemical response upon ligand binding<sup>15</sup>. Recent electrochemical biodetection has been reported using nanomaterials such as carbon nanotubes<sup>16</sup>, colloidal gold nanoparticles<sup>17</sup> and nanowires<sup>18</sup>. Despite current limitations on detectable species, label-free electrochemical sensors enjoy success partly because of the ease of manufacture and parallelizability as the technology is compatible with existing semiconductor fabrication techniques.

## **1.1.4 Optical Transduction**

### **1.1.4.1 Surface Enhanced Raman Scattering**

Surface enhanced Raman scattering (SERS) is another optically based, label-free technique that can be used to detect and identify surface-adsorbed molecules. Conventional Raman spectroscopy is performed by illuminating a sample and collecting the fraction of photons that were inelastically scattered by the sample. The slight energy shifts in these photons are due to energy that was coupled into molecular vibrational modes. The spectrum of these energy transfers is referred to as a molecule's spontaneous Raman spectrum and is uniquely characteristic of that molecule. In this way, Raman spectroscopy offers a label-free means of identifying molecular targets. Spontaneous Raman spectra are collected by exciting a target sample with a light source and comparing the scattered light with the spectrum of the incident light to detect Raman shifts. The amount of Raman-scattered photons is directly proportional to the intensity of the incident light and the number of excited molecules. However, because of the low probability of Raman interactions, typical molecules exhibit scattering cross sections of  $10^{-30}$  to  $10^{-25}$  cm<sup>2</sup> <sup>19</sup>. So historically, Raman spectroscopy had been limited to relatively large sample concentrations under high intensity illumination, although recent

technological advances in light sources, detectors and scanning probe techniques have significantly reduced sample size requirements and detection limits<sup>20</sup>.

It has been found that Raman scattering can be dramatically enhanced by proximity of the target molecule to roughened metallic substrates as well as near plasmonic nanostructures<sup>20</sup>. First observed in 1977<sup>21</sup> the exact mechanism of SERS is still under investigation, but two contributing factors are generally considered in the literature. A chemical explanation of the SERS effect suggests that the substrate surface electrons act as a charge-transfer mediator, allowing energy to couple from excited electron transitions in the underlying substrate to the excited molecule<sup>22</sup>. The electromagnetic explanation suggests that large electric field enhancements caused by plasmonic coupling of incident light to substrate surface features greatly enhances the local electric field<sup>23</sup>. This explains why SERS generates such large signals for molecules not in direct contact with the substrate, but does not explain the immense magnitude of SERS signals observed in certain instances as they can greatly exceed the expected electric field enhancements. Signal enhancement factors of up to  $10^{14}$  have been reported<sup>19, 24</sup> which has opened the door to applying Raman scattering techniques to bioanalytical methods, for example, the detection of glucose<sup>25, 26</sup>, genes<sup>27</sup>, and proteins<sup>28, 29</sup>. In addition, detection of individual molecules by SERS has also been reported<sup>30, 31</sup>.

#### **1.1.4.2 Surface Plasmon Resonance**

Planar Surface Plasmon Resonance (SPR) spectroscopy (also termed conventional SPR to distinguish it from local SPR exhibited by noble metal nanoparticles, a modality that is discussed later in this Chapter) is, at the present time, the most commonly deployed label-free detection scheme. In fact, an exhaustive survey of all

literature published in 2007 describing work utilizing commercial optical biosensors found that 96% of the work in this field was performed using “SPR or related technologies<sup>32</sup>.” Initially developed in the early eighties<sup>33</sup>, SPR was later applied to quantify biomolecular interactions at surfaces<sup>34, 35</sup>. Since then, the technology has been commercialized by several companies; Biacore (now part of GE LifeTechnologies) has the largest number of instruments in use. Recent advances in SPR technology include fiber and wave-guided resonances, SPR on silicon material, and SPR imaging<sup>36</sup>.

In a typical planar SPR measurement, light is incident through a prism or grating on to a thin gold film. The surface of the gold opposite the prism acts as the detector surface. The grating or prism is necessary to modify the momentum of the incident light such that its electromagnetic field components are at a proper frequency to act as a driving force for the conduction electrons on the gold surface. The oscillation of these electrons at optical frequencies generates a standing wave on the surface of the gold that extends ~200 nm into the medium above the gold film. Any dielectric within this region will alter the energy of the oscillating field, thus changing the natural frequency of the oscillation. This phenomenon can be utilized for label-free sensing as any material within the sensing range of the film will cause a resonant energy shift. This shift can be measured by either collecting a full-wavelength reflection or transmission spectrum of the SPR surface and monitoring resonant peak shifts, or by monitoring the incident angle-dependent reflection or transmission of a monochromatic source. For biomolecular interactions, the surface of the gold film can be modified with a binding moiety that targets the analyte of interest. Upon incubation with a sample containing the target of interest, the increased dielectric caused by presence of the target analyte induces a resonant shift in the SPR.

SPR detection techniques offer highly sensitive, real time detection of material down to the pM concentration of target analyte. The commercial success of Biacore provides well-characterized devices and a wide knowledge base for researchers in this field. In 2007 alone, at least 1050 peer-reviewed articles were published using SPR detection (89% using Biacore technology). These include reports on the functional characterization of proteins, antibodies, peptides, oligonucleotides, and small molecules such as lipids and carbohydrates<sup>32</sup>. Despite the success of SPR systems, there remain some limitations to its application. First, because the sensing distance is on the order of a few hundred nanometers from the film surface, the detection of small molecules can be problematic as they occupy a relatively small fraction of the overall sensing volume. Additionally, the sensor area typically queried in an SPR device is on the order of square millimeters with no spatial resolution. Thus, the data is collected as an ensemble measurement of the entire surface, limiting parallelizability and detection with patterned substrates for spatial registration.

Developments in a technique known as surface plasmon resonance imaging (SPRI) have been reported as a means to address the parallelizability and spatial registration limitations of conventional SPR. The imaging aspect of the technique is obtained by replacing the single light detector with an arrayed detector such as a CCD or photodiode array<sup>37</sup>. In addition to increasing spatial resolution, research has been conducted in increasing the number of excitation wavelengths employed to allow for more additional concurrent measurements, increasing overall sensitivity<sup>38</sup>. More recently, this technique has been applied to micro-arrays, exhibiting full parallelizability of SPR biomolecular detection<sup>39, 40</sup>.

### **1.1.4.3 Localized Surface Plasmon Resonance**

Sensors based on the phenomenon of localized surface plasmon resonance (LSPR) utilize optically-active, metallic structures as their primary sensing mechanism. Such structures exhibit wavelength-dependent light interaction that is modulated by the nanostructure's local environment. As sensors of this type are the primary focus of this thesis, the following section will provide further details into the specifics of LSPR-based biosensors.

## ***1.2 LSPR Biosensing***

### **1.2.1 Operating Principles**

The unique optical properties that lend noble metal nanoparticles their extraordinary sensing properties are derived from their surface conduction electrons. The electric field from incident light provides an oscillating driving force that pushes the conduction electrons away from the metal lattice core. A restoring force is then provided by the coulomb attraction between the displaced electrons and the positively charged metal lattice. When driven at resonance, the oscillating electrons behave as a single dipole, emitting photons as it oscillates. Thus, individual nanoparticles behave as elastic light scatterers, preferentially scattering light which couples resonantly with the oscillating electrons. This oscillation of electrons on the surface of a nanoparticle is known as localized surface plasmon resonance (LSPR). Any change in the system that alters the resonant energy of the plasmon will therefore change the scattering characteristics of the nanoparticle. In particular, nanoparticle composition, geometry, proximity to other conductors, chemical bonds to lattice atoms, and the local refractive index (RI) are all parameters that have been shown to alter the resonance of a plasmonic system.

The LSPR of a nanostructure is unique to its material composition because the resonant conditions are a function of its complex refractive index<sup>41</sup>. In fact, only a few materials exhibit plasmonic behavior at optical frequencies. Many of the materials that exhibit plasmonic behavior are noble metals such as gold<sup>42</sup>, silver<sup>43</sup> and platinum<sup>44</sup>, although plasmonic behavior has been observed in copper<sup>45</sup> and aluminum as well.

The shape and size of a nanoparticle determines the number of oscillating electrons, the direction and magnitude of the restoring force, which together define the polarization and physical extent of the plasmon. For example, cylindrical nanorods have been shown to exhibit two distinct resonances when illuminated with unpolarized light—corresponding to excitation along the longitudinal and transverse dimension<sup>46</sup>. It has further been shown that the orientation of individual nanorods can be determined by observing the relative magnitude of these resonances<sup>47</sup>. Efforts have been made to synthesize and characterize a wide variety of nanostructures<sup>48</sup> including spheres<sup>49</sup>, rods<sup>50, 51</sup>, cubes<sup>52, 53</sup>, triangular prisms<sup>54</sup>, shells<sup>55, 56</sup>, crescents<sup>57</sup> by both chemical synthesis as well as by top-down manufacturing such as by electron or ion beam lithography and nano-imprinting<sup>58</sup>.

Additionally, their proximity to other nanoparticles or conductive films will alter LSPR behavior of a nanoparticle. For nanoparticles in close proximity, resonances from one or more nanoparticles couple, producing more complex resonance modes. The simplest case, dimers of nanospheres, has been extensively studied, both theoretically<sup>59</sup> and experimentally<sup>60</sup>. A large shift in LSPR is induced when resonant nanoparticles become proximal<sup>61</sup>. This effect was cleverly demonstrated by Prikulis et al. who observed a visible and reversible distance-dependent LSPR shift of two isolated nanoparticles, by immobilizing one and controlling the distance between the two

nanoparticles by trapping the second nanoparticle by an optical tweezer<sup>62</sup>. One LSPR sensing modality that exploits this effect involves chemically modifying the surface of the nanoparticles so that they will aggregate in the presence of a target molecule. For example, the interparticle distance-dependent LSPR shift of gold nanoparticles due to aggregation in solution has been used to detect oligonucleotide hybridization by Mirkin and co-workers with single base mismatch discrimination<sup>63</sup>. Similar to coupled nanoparticles, the presence of a conducting film also affects a distance-dependent modulation on the LSPR of nanoparticles. We have recently published findings observing this phenomenon and describing its potential application in biosensing<sup>64</sup>.

Another phenomenon regarding LSPR that has been used for molecular detection is known as charge-transfer or chemical interface damping. When anions (SH<sup>-</sup> in particular) are adsorbed to the surface, the electron distribution of the nanoparticle is altered. This results in the damping of LSPR which can be observed as a widening of LSPR spectra and a blue shift in the resonant wavelength<sup>65, 66</sup>. While this means of modulating the LSPR signal of a nanoparticle has interesting photochemical implications<sup>67</sup>, its application to biodetection has taken a more secondary role most often as a side-effect of surface modification applied to nanoparticles towards other detection schemes<sup>54</sup>.

The RI of the medium surrounding the nanostructure is another factor that modulates the plasmonic behavior of nanoparticle and which has been profitably exploited as a transduction modality in LSPR based biosensing. The electric field of the resonantly oscillating electrons extends into the volume beyond the surface of the particle. Changing the dielectric properties of this region alter the energy associated with the electric field oscillation. As most biological materials are relatively non-

absorbing and non-magnetic, a change in dielectric can be directly translated to a change in RI. Generally this effect is observed as a red shift in the LSPR peak of a nanostructure upon an increase in the local RI. This is the operating principle responsible for detection with a conventional planar SPR system (such as Biacore). This scheme has been extended to the use of nanoparticles usually by functionalizing the nanoparticle surface with a specific receptor, and observing the LSPR change as the local RI increases upon binding of the target analyte<sup>68</sup>. Ensemble measurements of this sort were first demonstrated using gold nanospheres in suspension to infer affinity constants of protein specific interactions<sup>69</sup>. This approach was then extended to gold spheres immobilized on a surface in a chip-based format allowing for easier nanoparticle functionalization<sup>70, 71</sup>. Since then, several groups have reported studying biomolecular interactions by observing ensemble LSPR shifts of particles immobilized to a surface using gold rods<sup>72</sup>, silver triangular prisms<sup>73</sup>, silicon-gold core-shell nanoparticles<sup>56</sup> and others. Biomolecular detection limits in the sub-nanomolar range have been reported for ensemble-based LSPR sensors with a dynamic range of four to five orders of magnitude of analyte concentration<sup>72, 74</sup>. Additionally, this methodology has been further extended down to the single nanoparticle scale by our group<sup>75</sup> and others<sup>56, 76, 77</sup>.

### **1.2.2 Comparison with SPR**

The operating principles behind biomolecular detection with conventional planar SPR and with LSPR using nanostructured materials are phenomenologically similar in that both approaches utilize resonant oscillations in surface conduction electrons. There are however, several fundamental differences that merit discussion since they influence how each technique is implemented as biosensing modality.

Both techniques are most commonly used to detect the presence of target molecules by the corresponding increase in local refractive index. In both cases, this change causes a shift in the overall plasmon resonance of the system, but how this is measured in each case is fundamentally different. In the case of planar SPR, the Kretschmann configuration is the most commonly employed. In this setup, monochromatic light is coupled into the surface plasmon through a prism at an angle such that total internal reflection is achieved. The prism must be of a higher refractive index than the detection medium so that the momentum of the incident light is sufficient to excite a surface plasmon on the metal surface. The photons which most strongly couple into the plasmon are those that are incident at the specific angle such that the component of their momentum vector perpendicular to the surface matches the frequency of the surface plasmon resonance. As the resonance shifts as a function of a change in the local refractive index due to binding of an analyte to receptor that is immobilized at the transducer surface, the corresponding optimum resonant angle will also change. Thus, biomolecular binding is converted to an angle-dependent measurement. Commonly, this is quantified by observing the intensity changes of the incident beam after it impinges on the SPR surface. Stronger coupling into the plasmon means less light is reflected to the collecting detector. In their simplest form, SPR detectors measure reflected light intensity at a fixed angle on a point in the angularly-resolved spectrum where intensity changes are linear with respect to SPR shifts. As this curve is only linear over a relatively short angle range (the spectrum curves), the dynamic range of the sensor is limited to only measuring small shifts that remain within the linear region.

By contrast, the LSPR excitation can typically be excited in a nanostructure by light incident at any angle. This is because the entire structure is necessarily smaller than the wavelength of excitation light and as a result, the entire nanostructure experiences electric field oscillations that are generally in phase. Thus, it is generally the polarization of the incident light that has the greatest effect on which resonances can be excited in a plasmonically active nanostructure, since this determines the physical direction that the surface electrons are driven. Thus, the differentiation of light energy from which electron resonances can be driven comes directly from the photon energy of the incident light. Therefore, LSPR measurements are generally wavelength-resolved and involve monitoring spectral shifts of resonance peaks in the wavelength dimension. Typically this is performed by exciting the nanostructure with white light and monitoring the corresponding interaction in a wavelength resolved manner. One method commonly used for interrogating larger areas of a nanostructured substrate is to monitor the extinction of the sample by analyzing light that has passed through the sample. Light that couples strongly into the LSPR will be both absorbed and scattered by the sample, creating a subsequent decrease in transmitted light at the resonant frequencies. Another method which is commonly used to interrogate less densely packed nanostructured systems is to analyze only the scattered light. This is an effective means of interrogating samples that have relatively low extinction cross-sections when scattered light can be isolated, such as in darkfield microscopy, which is discussed in chapter 2. These wavelength-resolved measurements are typically measured by some sort of optical spectrometer. Most often, the light to be analyzed is incident to a dispersive element (generally a prism or grating), which spatially separates the light as a function of its wavelength. If only a single light intensity detector is used, this dispersive

element can be rotated so a series of measurements can be made with each ascertaining the light intensity at a certain wavelength. Alternatively, many detectors can be arrayed such that each single detector can be used in concert to determine the complete wavelength resolved LSPR spectrum of the nanoparticle.

This difference in the dimensionality of resonance spectra –incident angle for planar SPR versus incident wavelength for LSPR– does not in itself fundamentally confer restrictions of the utility of either sensor. However, the technological means by which each method is implemented does have an effect on sensor performance. For example, in the case of SPR imaging, adding two further spatial dimensions to a data set offers the challenge of three-dimensional data collection. The practicalities of this approach are discussed in detail in chapter 5. It must also be noted that some approaches for SPR-based detection have converted angular resolution to wavelength resolution, for example by employing a gold film grating instead of planar gold as the underlying substrate<sup>78</sup>.

One aspect that is fundamentally different between LSPR and SPR detection systems is the physical extent of the electric field enhancement resulting from the respective plasmon resonances. The sensitivity of the resonance to the local RI is a result of the direct dependence of the resonant energy on the dielectric of medium in which the oscillation occurs. Therefore, the so-called “sensing volume” of a plasmonic system is described by the region of electric field enhancement. Further, the relative sensitivity of the overall resonance to refractive index in a particular region is proportional to the square of the electric field intensity in that region<sup>79, 80</sup>. Thus, the electric field distribution of a plasmonic sensor is critical to its performance as a label-free sensor. In planar SPR, the excited plasmon is essentially a standing wave of the

conduction electrons of the substrate surface. This creates an electric field enhancement that is highest nearest the surface and decreases exponentially further from the surface<sup>81</sup>. A characteristic distance known as a plasmonic system's decay length or sensing distance is typically defined as a metric to describe this effect. Typically, this is defined as the distance at which the electric field enhancement has decreased 95% from its value at the metal surface<sup>80</sup>. For planar gold, this distance is approximately 300nm<sup>79</sup>. As most biomolecules have physical dimensions smaller than ~10nm, only a small fraction of the available sensing volume can consequently be utilized, if we assume that binding is restricted to a two-dimensional surface. This restricts the relative magnitude of resonance shifts that can be achieved by molecular binding. However, because of the uniform nature of the field enhancement across the surface and the relatively slow field enhancement decay in the direction perpendicular to the surface, every bound molecule will be in a region of similar field magnitude. Thus, the corresponding resonant shift will be similar for each bound molecule, resulting in highly linear dose-response characteristics.

By contrast, the electric field enhancement of plasmonic nanostructures tends to be more locally confined. For example, the field enhancement of noble metal nanospheres generally extends about a particle radius beyond the metal surface, and that of gold nanorods extends approximately one diameter<sup>80</sup>. Thus, nanostructures that are plasmonically active in the visible wavelength range have sensing distances that are typically 10-40nm. This tighter field enhancement distribution means that a larger proportion of a nanostructure's sensing volume will be occupied by bound biomolecules resulting in a higher fraction of the full potential resonance shift. However, the spatial distribution of field enhancement around plasmonic nanostructures is highly non-uniform.

For example, nanorods have been shown to exhibit much larger field enhancements at the ends of the rod as compared to its periphery<sup>46, 82</sup>. Consequently, molecules that bind to a gold nanorod near the end-caps will generate a larger resonance shift than those bound along its sides, which can compromise the linearity of the system's dose-response characteristics. Some investigators have attempted to purposely design structures with high non-uniform field distribution with the goal of utilizing those regions of highest enhancement as highly sensitive detection areas. Examples include so called "bow-tie" structures<sup>83</sup>, crescent shaped structures<sup>57, 84</sup>, and coupled dimers of individual spheres<sup>59</sup>.

The consequence of this difference in electric field enhancement localization is more apparent in regards to the sizes of materials detected than overall detection limits. For example, protein detection limits of both planar SPR and LSPR techniques is in the 0.02 – 2ng/mL range<sup>73, 85-89</sup>. However, SPR sensors have been shown to be challenged by detection of small or sparsely bound molecules<sup>19</sup> but LSPR sensors have been shown to be limited in detecting larger objects such as bacterial cells<sup>90</sup>.

Recently, there have been increased efforts towards combining LSPR and SPR systems in a way that complements the advantages of each system. Some of these techniques include an SPR-based labeling scheme in which target molecules are labeled with plasmonically active nanoparticles. The resonances of the coupled nanoparticles interacts with the surface plasmon of the gold surface resulting in an increased SPR signal<sup>91</sup>. This approach has been demonstrated as a means to amplify SPR detection of proteins<sup>92</sup>, oligonucleotides<sup>93</sup> and chemical sensing<sup>94</sup>. In a label-free approach, sensor substrates have been studied that are composed of an underlying gold film decorated with nanoparticles<sup>95, 96</sup>. This system then forms the label-free SPR

substrate in which shifts in the composite plasmon resonance is observed with an increase in overall refractive index sensitivity<sup>97</sup>. Improvements in sensitivity by as much as 57% have been reported for these composite substrates over conventional SPR<sup>98</sup>. Further reports investigate the use of a spacer layer of silicon between the gold film and the nanoparticles to optimize resonant shifts for both nanoparticle-labeled<sup>99</sup> and label-free biomolecular detection<sup>100</sup>.

### **1.2.3 Application/Fabrication**

As mentioned previously, the composition and geometry of a plasmonic nanostructure determines the properties of its corresponding electron resonance and therefore its overall properties as a sensor. Of practical concern regarding nanoparticle implementation is the manufacturability of a desired geometry. In order to query the space of nanostructures available for diagnostic applications, many approaches have been developed that utilize various means of nanostructure assembly. An ideal production methodology is low cost, generates robust, highly reproducible structures and is scalable. Obviously, the goal of selecting an optimized nanostructure is not always achievable due to manufacturing limitations and practical production strategies require some compromise of these four characteristics. Additionally, most optical detection modalities (with the exception of single-nanostructure detection schemes), query illumination areas that are relatively large in comparison to the size of the nanostructures themselves. For example, the first surface-based LSPR detection scheme reported nanoparticle coverage of  $1.5 \times 10^{11}/\text{cm}^2$ <sup>70</sup>. So a 1 mm<sup>2</sup> detection area is simultaneously scanning over a billion particles. Thus, the production method must be able to simultaneously cover large areas with many nanostructures because serial production would be prohibitively time consuming. The two primary means of achieving this sort of

production are chemical synthesis of nanoparticles, and various top-down lithographic techniques. Many reviews are available in the literature that explore diagnostic applications of nanostructures<sup>19, 86, 101-103</sup>. In the following section, the discussion is limited to optical techniques in which biomolecules were actively detected in a label-free format. Detection limits from the literature have been converted to concentration units of bound mass per total analyte volume (e.g. grams/liter) as opposed to units of number of analyte molecules per volume (e.g. molar). This was done to allow direct comparison across studies of detecting analytes with different mass because LSPR detection schemes generate signal based on total bound optical mass, not the number of bound analytes.

#### **1.2.3.1 Chemical Synthesis**

Chemical synthesis of noble metal nanoparticles is one method of fabricating plasmonically active biosensing substrates. Englebienne reported the use of chemically synthesized gold nanospheres as a biomolecular sensor in a colloidal suspension<sup>69</sup>. In these experiments, gold nanoparticles were chemically synthesized by the reduction of a chloroauric acid in the presence of an ionic stabilizer. While this process has been performed for centuries to create dyes for glass and pottery, it was formally reported by Turkevich and co-workers in 1951<sup>104</sup>. For biodetection in solution, Englebienne employed the gold nanoparticles as sensors by conjugating antibodies for the target analyte to the nanoparticles while they remained in suspension. High concentrations of the target analyte caused the nanoparticles to aggregate resulting in large LSPR shifts as the resonances coupled as measured by a conventional spectrophotometer. However, smaller LSPR shifts were noted at lower analyte concentrations which were caused simply by the increased refractive index caused by the bound analyte. Since this

experiment, the field exploded with reports of novel plasmonically active nanoparticles stabilized in a colloidal suspension. Several recent reviews cover the wide array of synthesis techniques<sup>105, 106</sup>. Similar biodetection experiments based on LSPR shifts induced by increased local refractive index near particles remaining in suspension has been reported for silica-gold core-shell nanoparticles in whole blood samples<sup>107</sup>. More recently, a protein marker for Alzheimer's disease was detected at limits near 20 pg/mL with a similar aggregation assay employing two-photon excitation to quantify resonance shifts.<sup>88</sup> The multiplexed potential of suspension LSPR-based assays was recently demonstrated by Yu and Irudayaraj, who demonstrated selective detection of three different species of protein by utilizing three separate nanorod geometries – each with conjugated with a specific antibody and a different resonant wavelength<sup>108</sup>. The resonances were spaced across the visible spectrum such that the LSPR peaks of each population could be simultaneously identified. In this manner, three species of protein could be independently measured from the same detection suspension in parallel.

The approach whereby LSPR shifts are caused by simply the increased local RI, and not interparticle coupling, was then extended to a surface-based format by our group in which a monolayer of gold nanospheres were chemically bound to a glass slide before being conjugated with antibodies for detection<sup>70, 109</sup>. This surface-based format allowed for reduced reaction volumes and increased the versatility of the system by removing the need for the gold nanoparticles to remain stable and non-aggregated – a challenge for nanoparticle modification in solution-phase applications, particularly for ionically stabilized particles as biologically relevant test samples will have ionic constituents. This initial experiment using gold nanospheres was demonstrated to detect the protein streptavidin at a concentration of 1  $\mu\text{g/mL}$ <sup>70</sup>. A similar approach was

subsequently using silver spheres to detect antibodies at 140  $\mu\text{g}/\text{mL}$ <sup>49</sup>. Recently, a sensor was demonstrated that detected the anabolic steroid stanozolol to a detection limit of 0.7ng/mL by using gold nanospheres on glass<sup>89</sup>. Other chemically synthesized nanoparticles used in a similar format for biodetection are gold bipyramids<sup>110</sup> and gold nanorods<sup>72</sup>.

### 1.2.3.2 Top-Down Lithography

Top down fabrication approaches are those which use lithographic techniques to directly build plasmonic structures on a substrate. For example, a silver film sputtered onto a glass slide at sub-monolayer coverage has been shown to coalesce into plasmonically active nanoscale islands, which were used to detect the selective binding of streptavidin at a concentration of 20 ng/mL<sup>111</sup>. A substrate formed by evaporative coating of gold onto a porous alumina substrate was similarly demonstrated to detect binding of thrombin at 2 ng/mL concentration to the aptamer-functionalized surface<sup>112</sup>. Most recently, detection of protein at a concentration of 10 pg/mL was demonstrated using a wavelength resolved system using gold-coated silica nanoparticles as the plasmonic substrate<sup>113</sup>. Other top-down lithographic techniques require multi-step processes to build large regions of individually separated nanostructures. For example, evaporating thin metallic films onto layers of previously deposited silica nanospheres can yield a gold film with plasmonically active nanometric holes after removal of the silica spheres. These substrates have been demonstrated to detect biomolecules by using receptor molecules bound to both the gold surface and to lipid bilayers deposited within the holes themselves<sup>114-116</sup>. Nanoscale triangular pyramidal structures have been fabricated using a similar fabrication methodology. If the silica nanospheres used as masks for the holes are deposited at a higher coverage - to the extent that a closely

packed monolayer is formed – subsequent metal deposition will only reach the underlying substrate in the triangular regions between adjacent spheres. Silver triangular pyramids formed in this manner have been extensively studied by Van Duyne and coworkers<sup>74, 117-119</sup>. These structures were functionalized with biotin and could detect streptavidin at a concentration of 250 pg/mL<sup>73</sup> and a peptide linked to Alzheimer's disease using a sandwich assay at an initial concentration of 100 fM<sup>120</sup>. Gold nanorings have also been fabricated and utilized for biosensing using two distinct synthesis techniques. The first synthesis method is similar to the synthesis of gold nanoholes described previously. However, after gold has been deposited over the entire substrate (that consists of sparsely spaced silica nanospheres on glass), a reactive ion etching of the surface is carried out. During the etching process, the gold atoms scatter in all directions by the high-energy ions. Some of the gold is subsequently re-deposited around the base of the silica nanospheres where they are shadowed from further etching leading to the formation of gold rings. These nanostructures were functionalized with biotin, and were shown to detect neutravidin at a concentration of 10 µg/mL<sup>121</sup>.

### **1.2.3.3 Non-Specific Adsorption Prevention**

In any study involving the specific interaction between biological molecules on a surface, significant noise can be generated from the propensity of most biomolecules – especially proteins– to avidly adsorb on to most solid substrates. Non-specific binding is a problem that limits the performance of biosensors for many reasons.. First, binding of non-target analytes that non-specifically bind or adsorb to the surface can generate false-positive signals. Another problem can arise when molecules non-specifically bind to the target receptor, blocking binding sites and potentially generating false-negative signals because the target species was sterically prevented from binding. Also, if target

analyte binds to the sensor at interfaces other than the transducer along the flow-path, the depletion of analyte concentration can be misreported by the detector as a lower measured concentration than the true concentration. Many of these obstacles can be particularly problematic for label-free sensors simply by virtue of their transduction modality – especially in detecting species in complex mixtures such as whole blood. For example, sandwich-based labeling assays generally exhibit higher specificity because of the dual selection of binding to receptor *and* the label. Investigators have explored several means to overcome these challenges for diagnostic devices in general and to the specific application of label-free optical biosensors<sup>122, 123</sup>. In the discussion below, the focus is limited to those strategies that have been successfully applied to LSPR sensor systems.

One strategy employed to prevent non-specific adsorption of sensor structures is the use of ethylene glycol (EG)-containing molecules and polymers. Non-specific adsorption of protein molecules has been shown to be reduced by surface passivation using coatings of poly(ethylene glycol) (PEG)<sup>122</sup>. It has also been shown that self-assembled monolayers of EG-terminated alkanethiols confer protein resistance to gold and silver<sup>124, 125</sup>. In LSPR sensing, detection of streptavidin in whole serum has been reported by utilizing a mixed monolayer of EG-terminated molecules and biotin-conjugated molecules to limit the non-specific adsorption of serum proteins<sup>72</sup>. In this case, the EG-terminated molecules serve to both reduce non-specific adsorption of the non-target proteins in serum, but also as a diluent to optimally space receptor molecules within the mixed monolayer<sup>126</sup>. In this manner, the biotin molecules can be optimally spaced to prevent steric hindrance while preventing adventitious adsorption of material to the remaining surface of the nanoparticle, minimizing false positive signal.

Phospholipid bilayers have also been shown to prevent the adhesion of non-specifically adsorbed biomaterial<sup>123</sup>. Phospholipid bilayers incorporating receptor molecules have been shown to allow the detection of streptavidin using individual gold nanorods<sup>127</sup> and for detecting neutravidin with nanoholes<sup>77, 114</sup>.

Surface passivation issues such as those described above attempt to address the depletion issue by minimizing the available area where the analyte of interest could bind non-detectably. However, in the case of sensors using a fluid handling system of some kind, this area extends throughout the entire system, not just the detector surface. One common tactic employed to contend with the depletion issue is to purposely pre-expose the sensor to a “sticky” material in order to occupy any high-energy surfaces that might otherwise collect target analyte. For example, bovine serum albumin is commonly used as a blocking agent in this manner<sup>128</sup>. Systems capable of continuous flow of detection solution can similarly block non-detectable regions, eventually equilibrating at the initial concentration of analyte<sup>75</sup>.

### ***1.3 Nanoparticle Detection***

As discussed in the previous section, the initial development of such sensors began with systems that interrogated a large ensemble of nanoparticles. However, the true power of a nanoparticle-based sensor comes from the virtue of its size. A single plasmonic nanoparticle has characteristic dimensions in the 10-100 nm size range. Thus, by miniaturizing a detection system down to a single nanoparticle, the entire sensing platform is in the same size regime as the target analyte molecules. This offers advantages to minimizing detection limits and opens the door for label-free detection of individual molecular binding events. It

should be noted that the ability to detect single molecules will not, per se, provide a gain in sensitivity as defined by the lowest concentration of the analyte that can be detected, primarily because of mass transport limitations<sup>129-131</sup>. Rather, miniaturizing the sensor to a single nanoparticle is of interest because it is a useful test of the limits of this technology for biosensing and also because it provides a potentially useful biophysical tool for the interrogation of single binding events that is complementary to other transduction modalities under development for single molecule, stochastic sensing<sup>132-135</sup>. However, certain limitations and constraints are also encountered by virtue of the scale of such biodetection systems. In this chapter we investigate the advantages and disadvantages of biodetection using individual plasmonic nanostructures and discuss recent advances in the field and their potential implications in label-free detection.

To date, all reported studies that employ plasmonic nanostructures on surfaces as signal transduction elements for biodetection can be classified by means of data collection into one of two categories. The first is referred to as ensemble measurements and refers to optical analysis of macroscopic substrates. The second means involves the analysis of individual nanostructures and is herein referred to as single-structure (SS) detection. Each data collection method offers its own advantages and is subject to unique limitations.

### **1.3.1 Ensemble Analysis**

An ensemble measurement is so named because macroscopic regions of plasmonically active substrate are analyzed. This area may contain a large number of

individual plasmonics structures on an underlying substrate, or simply be a substrate engineered to be plasmonically active. In either case, the large composite cross-section of light interaction offers distinct advantages. The large number of LSPR active nanostructures interacting with the incident light produces intense signals with high signal-to-noise ratio (SNR) relative to SS measurements. Higher SNR measurements can be used to detect small magnitude LSPR shifts more accurately<sup>136</sup>. Additionally, higher intensity signals can be sampled more quickly, thus increasing the time resolution of such measurements which is especially important in studies where dynamic effects are monitored such as biomolecular binding. Recent work by Dahlin et al reported SNR of 3000 for ensemble measurements of nanostructured holes in a gold film. These measurements allowed peak shifts to be determined at an uncertainty of  $10^{-3}$  nm measured at a temporal resolution of 2s per measurement<sup>115</sup>. Finally, ensemble measurements have the advantage of making optical measurements of a relatively large area – typically on the order of several square millimeters. Measurements of this sort are relatively simple and can be performed on readily available commercial equipment such as a spectrophotometer.

On the other hand, all nanostructure synthesis techniques result in a distribution of individual nanostructure geometry. From electron beam lithographically-written nanostructures to chemically synthesized colloidal nanoparticles, each synthesis technique yields members with slightly different geometry. Since a plasmonic nanostructure's LSPR peak location is directly determined by nanoparticle shape<sup>48, 137-141</sup>, this geometric distribution results in a distribution of resonant peaks. Thus, when a macroscopic area of nanostructure-decorated substrate is analyzed, the actual measurement is the ensemble spectrum of up to millions of individual LSPR peaks. This

spectrum therefore exhibits heterogeneous broadening compared to the single Lorentzian peak observed for each resonance of a single nanoparticle and therefore has a broader peak linewidth which leads to greater uncertainty in measuring small shifts in LSPR peak position<sup>136</sup>. Further, it has been shown that nanostructure bulk refractive index sensitivity is correlated with the peak wavelength of its LSPR<sup>142</sup>. Specifically, it has been shown that plasmonic nanostructures with LSPR peaks at longer wavelengths will have a higher bulk RI sensitivity. This means that under a given increase in surrounding refractive index, the constituent members of an ensemble system will each experience a shift of differing magnitude. The nanostructures with longer wavelength resonances will shift further than those at shorter wavelengths. The net effect is an asymmetric broadening of the ensemble spectrum as it redshifts. This is observed experimentally as the leading edge of the resonant spectrum appearing to be shifted further than the following edge. This relative magnitude of this effect depends on the heterogeneity of the nanostructures used and can further complicate data interpretation. Additional problems can also arise for nanostructures that exhibit more than one primary LSPR peak. For example, the primary resonance of gold nanorods corresponds to conduction electrons oscillating along its length – known as the longitudinal mode. However, smaller resonant peaks that are blue-shifted with respect to longitudinal mode exist and have been shown to be highly dependent on nanorod end cap geometry and thus tend to vary widely between chemically synthesized nanorods<sup>143</sup>. Thus, the contribution of these secondary peaks can further complicate the direct measurement of ensemble LSPR shifts.

### **1.3.2 Single Nanostructure Analysis**

Many advantages result from the miniaturization of the label-free signal transducer down to the single nanostructure. First, with concomitant miniaturization of the fluid handling system, sample volumes can be greatly reduced, which is likely to be important in the design of clinical diagnostics where analysis is constrained by the available sample volume (e.g., in neonatal diagnosis and archival samples), or by the high cost of reagents. Additionally, the miniaturization of a biosensor down to the nanoscale allows for measurements to be made in regions not accessible by macroscopic sensors, such as within live cells<sup>144</sup>. As SS detection systems advance, the realization of optical, label-free single molecule is becoming a reality<sup>80, 145</sup>. Such detectors offer the chance to study molecular interactions in a real-time, stochastic manner, enabling further exploration into the fundamental nature of these reactions.

Single nanoparticle interrogations also offer a method to bypass LSPR peak broadening present in ensemble studies. By interrogating single nanoparticles, individual resonance peaks are analyzed independently, each with a much narrower line-width, increasing the ability to observe peak shifts and thus overall measurement accuracy<sup>136</sup>. It has even been shown that nanostructures with multiple resonances can be used to gain insight as to where on the structure material is bound. This is possible because each resonant peak in the LSPR spectrum corresponds to a physical oscillation mode that can occur in different physical locations. For example, various resonances have been probed for

individual gold nanocrescents by introducing a silica nanosphere at various locations using an AFM tip<sup>146</sup>. Thus, particles with multiple resonances can offer information regarding binding location as well as just bound amounts.

Just as many of the advantages of SS detection methods are derived from their scale, so are many of their disadvantages. Signals generated by individual nanoparticles are obviously quite small, so highly specialized equipment is typically necessary to perform detection experiments. Typically a microspectroscopy system is employed that requires a microscope as a base platform and a light detection apparatus. In general, the small signals generated by SS detection systems require more sensitive light detection equipment than ensemble measurements. Often, a custom fluid handling system is also involved due to the physical constraints from the optics around the sample detection region. As a result, SS detection systems are typically more expensive and complex than ensemble measurements.

Experimentally, these sorts of detection systems have a few fundamental limitations. First, the incident light intensity that a given nanostructure receives invariably fluctuates as this intensity is a complex function of surface reflections, nearby scatterers, spatial distribution of the incident light, among others which can all in turn change as the medium refractive index, temperature or other physical parameters change. The result is that the intensity of LSPR resonances cannot be reliably measured, limiting dependable measurements to only wavelength<sup>136</sup>. In addition, physical stability of the microspectroscopy system is an issue because the physical relationship between the location of the scatter and the detection system can change how it is perceived by the measuring equipment. For example, focus depth and relative

physical positioning of scattered light spots in relation to an imaging spectrometer slit have been demonstrated to affect LSPR measurements.

Analytically, the small signals generated have negative consequences as well. First and most obvious is the fact that signals with lower signal to noise ratio (SNR) are less statistically reliable and thus smaller resonance shifts are more difficult to measure. In order to increase SNR, most investigator employ a darkfield illumination scheme which illuminates background illumination light that typically overwhelms small signals from individual nanostructures. This dramatically increases the SNR of these measurements but the consequence is that only resonant scattering is measured. This is in contrast to extinction measurements which measure the combined absorption and scattering of the sample which is necessarily a larger signal. Finally, the smaller signals measured in SS detection systems typically require a longer light collection time per measurement. This increases the SNR of each measurement but also reduces the temporal frequency at which measurements can be made, limiting time-resolution of dynamic measurements.

### **1.3.3 Biodetection with Single Nanostructures**

The plasmonic response of individual nanostructures such as gold nanoshells<sup>56</sup>, silver spheres<sup>76</sup> and silver triangular prisms<sup>117</sup> have been previously investigated in response to the self-assembly of alkanethiols on the surface of the noble metal nanostructures. We are aware of only four studies, in addition to our own, that have studied biosensing at the single nanoparticle level. Raschke et al used spherical gold nanoparticles functionalized with biotin to detect streptavidin binding at 50  $\mu\text{g}/\text{mL}$  level<sup>147</sup> in 2004. Rindzevicius et al reported in 2005 on LSPR shifts from single plasmonic nanoholes in response to the binding of 1  $\text{mg}/\text{mL}$  neutravidin to biotin-BSA<sup>77</sup>. This was

followed by our report in 2008 of the detection of streptavidin to biotin-functionalized gold nanorods at a detection concentration of 50 ng/mL<sup>75</sup>. Also in 2008, Bacia et al report the detection of streptavidin at 1 µg/mL on single gold nanorods that have been activated by depositing a biotin-containing lipid bilayer over the entire sensor surface<sup>127</sup>. Then, in March 2009, 1.3 µg/mL detection of avidin was reported using gold spheres decorated with aptamer receptors. One week later our report demonstrating optimization of gold nanorod geometry was published. In this work, we demonstrated the detection of streptavidin from a concentration of 8 ng/mL<sup>80</sup>. It is worth noting, that although this detection limit is over two orders of magnitude better than any other reported SS detection regime, it is still one order of magnitude worse than the same sensor employed in ensemble mode<sup>72</sup>.

#### **1.4 Plasmonic Imaging**

The development of truly scalable multiplexed detection systems using plasmonic systems requires a detection platform capable of simultaneous detection of multiple independent signals. Optical microarrays, the most commonly used multiplexed assays, use spatial separation to distinguish detection signals. Optical microarrays offer high-throughput analysis of large number of targets and have thus seen extensive use in applied to genomics, diagnostics, toxicology, nutrition, pharmacology and many other areas. Several recent reviews describe recent advances and applications of optical microarrays<sup>148-150</sup>. Most microarray detection approaches use labeling strategies to generate sufficiently large signals for the low concentrations of targets. Either the targets themselves will be labeled (such as DNA PCR products incorporating fluorescent molecules), or a sandwich-type assay can be used where secondary labels are attached to captured target molecules (such as a fluorescently labeled antibody for the detection

of protein). While labeled approaches have been very successful, several practical concerns limit their usability. First and foremost, the introduction of labels can affect the behavior of the labeled molecule and potentially alter interactions with other species. The labeling process also increases the cost and complexity of the assays. Additionally, it restricts assays to molecules which have been successfully conjugated to labels. Labeling efficiency can also vary between species which complicates detection quantification<sup>150</sup>. Fluorescent molecules also suffer from photobleaching which can further complicate quantification.

Recent efforts in the field have been towards developing a label-free multiplex detection platform in order to exploit the advantages of parallel detection without the limitations of labels. One promising candidate for such detection is the use of surface plasmon resonance imaging (SPRI). SPRI is performed by collecting a spatially resolved image of a plasmonic substrate so that individual regions can be independently measured. A field of view might be one continuous substrate with independent regions activated with different receptor molecules, or it may contain isolated, plasmonically active regions. This technique was first demonstrated in the late 1980's<sup>37, 151</sup> and since then, SPRI has proven to be a practical alternative to fluorescent labeling techniques, and a useful tool and for the study of biointeractions. Many recent reviews highlight new applications and innovations in SPRI techniques<sup>148, 149, 152, 153</sup>. In the paragraph below we discuss recent innovations in label-free optical detection instrumentation employed and their effect on the detection limits of SPRI systems.

As discussed previously, plasmonic resonance shifts are measured primarily by three means: intensity, spectrally resolved, or angularly resolved. Due to its simplicity, the most common form of data collection for SPRI systems is intensity-based

measurement. This detection scheme is perfectly analogous to the case of quantifying conventional SPR measurements by reflected light intensity discussed above in section 1.2.2. Briefly, images are collected at a fixed incident angle with a low bandwidth light source. The wavelength and angle of excitation are selected to be in a position on the resonance curve that has a steep slope and is relatively linear. As material binds to regions being imaged, the resulting resonance shift in that area causes a change in the light intensity collected by the corresponding CCD pixels. Intensity-based SPRI measurement systems are commercially available (from at least five companies at the time this is written<sup>149</sup>), and the technique has been extensively used to investigate DNA<sup>154-157</sup> and protein<sup>158-161</sup> microarrays. Recent efforts to improve sensitivity of intensity measurements have also shown that monitoring the polarization of the reflected light can enhance system sensitivity<sup>162, 163</sup>. However, current detection limits of intensity-based SPRI is typically about 10-100 times worse than with conventional, non-multiplexed SPR<sup>153</sup>.

Some of this loss of sensitivity can be attributed to inherent limitations of intensity based measurements. The primary problem with intensity systems is their low data resolution. Obviously, an entire spectrum of points describing a system's resonant frequency is more useful in assessing changes than a single point. Another issue is that the plasmon resonance curve is only linear over a relatively short span. As bound material causes the resonance peak to shift, the monitored intensity is no longer within this linear region. This results in a highly constrained dynamic range.

Alternatively, measurements can be spectrally-resolved, or angularly-resolved. Such methods thus involve data that is three-dimensional – two spatial dimensions and one either spectral or angular. Any optical measurement is limited in its acquisition to

only two dimensions, because current CCD's and photodiode arrays have only been built with two dimensions of detectors. Either the dimensionality of the data needs to be reduced, or a third dimension in data collection is needed. In order to collect full 3-D data cubes, time is used to collect a 2-D data series that can be compiled into a full 3-D set. For example, a large increase in dynamic range has been reported by the utilization of a commercially available (Biacore: Uppsala, Sweden) angularly-resolved SPRI scanner. The device uses a scanning mirror to continuously scan the excitation angle, adding angular resolution to the data<sup>164</sup>. The authors report a 10-fold increase in dynamic range over intensity-based SPRI and a 25-100 fold better detection limit than the companion fluorescence studies employed as controls.

Other methods that have been investigated to increase the sensitivity of intensity-based measurements involve the spectral distribution of the plasmon resonance. These techniques are particularly attractive from an instrumentation standpoint because they require no moving parts. Several techniques involve a straightforward multispectral approach. One report describes an increase in sensitivity and dynamic range by illuminating the plasmonic substrate with white light and collecting images with three different color filters<sup>38</sup>. Similar approaches towards spectrally-resolved collection have used either tunable filters<sup>165, 166</sup> or tunable light sources<sup>167</sup> to compile full 3-D data sets by collecting several images over time and then compiling them. Another class of techniques involves using an optical diffractive element to translate one of the spatial dimensions of a CCD detector to either wavelength<sup>168</sup> or incident angle resolution<sup>169</sup>. In these cases, one column of array spots is measured at a time, and the detector is scanned along rows to collect the full 3-D data set. Sensitivity levels of this technique have been shown to be compare to conventional single-detector SPR<sup>168</sup>. One similar

wavelength-resolved SPRI method has been reported that allows for simultaneous spectral investigation of up to 20-vertically isolated plasmonic structures<sup>127, 170</sup>. In these experiments, an electronically addressable liquid crystal device replaces the entrance slit to a line-imaging spectrometer. The detection is fundamentally similar to the previously described method of observing columns and scanning the sample, but in this case the LCD filter allows arbitrary selection of vertically separated sample regions and precludes the need of scanning hardware.

Although these multiplexed methods have been shown to exhibit detection sensitivity at comparable levels to current serial methods, most of these approaches make these gains at the cost of time resolution. One of the primary assets of label-free detection is that molecular interactions can be observed without undue perturbation of the system by introducing labels. However, by reducing the speed at which data can be collected, we severely restrict the ability of the sensor to monitor dynamic phenomena.

## **2 Darkfield Microspectroscopy System**

Initial system characterization experiments of the darkfield microspectroscopy system were performed using gold nanospheres. They are commercially available at narrow size distributions. Their spherical symmetry also simplifies theoretical calculations of resonance peaks and other optical behavior<sup>41</sup>. Additionally, nanospheres with diameter greater than 60 nm offer extremely high scattering cross-sections, allowing for easy visualization of individual nanoparticle spots. Although gold nanospheres have smaller scattering cross-sections than those composed of silver, the gold particles resist oxidation which alters LSPR peak position and intensity. For these reasons, we use 60 and 80 nm diameter gold nanospheres as measurement standard for the microspectroscopy system characterization.

### ***2.1 Experimental Preparation***

#### **2.1.1 Materials**

Glass coverslips, glycerol, ethanol, methanol, and hydrochloric acid were purchased from VWR. Aminopropyltriethoxysilane (APTES) and mercaptopropyltriethoxysilane (MPTES) were purchased from Gelest. Distilled water purified by a reverse-osmosis filtration system (18 M $\Omega$ -cm, Myron L Company, Series 750) was used for all experiments. Citrate-stabilized gold nanospheres with mean diameters 60 nm and 80 nm were purchased from BBI International.

#### **2.1.2 Substrate Preparation**

Gold nanoparticles were immobilized onto 25 mm diameter, round No.1 glass coverslips in a manner similar that previously reported to fabricate nanoparticle sensor chips<sup>70</sup>. First, the coverglasses were cleaned by sonication for 20 min in a 1:1

HCl/methanol mixture. The coverslips were rinsed with ethanol, dried overnight at 65° C. Coverslips for nanospheres were activated with APTES 10% (v/v) MPTES in ethanol for 15 min. The coverslips were rinsed several times with ethanol, and then dried at 120 °C for 3 h. Nanoparticle suspensions were first diluted in water to 1:15 (v/v) and a 20 µl aliquot of the suspension was pipetted onto the center of the coverglass and incubated for 10s before being rinsed off with water. Interparticle spacing has been shown to be a function of nanoparticle concentration and incubation time<sup>51</sup>. This nanoparticle concentration and incubation time have been empirically determined to produce nanoparticle chips with an average interparticle spacing of ~5 µm, which is ideal for interrogation of isolated nanoparticles by the microspectroscopy system because the diffraction limited spots are separated enough as to not overlap.

## ***2.2 Darkfield Imaging***

Darkfield microscopy is a technique commonly used to visualize light scattered by individual nanostructures<sup>42, 76, 137, 147, 171, 172</sup>. Darkfield refers to the illumination conditions of light incident on the target. Under darkfield illumination, the incident light is directed such that it will illuminate the sample area, but will not be collected by the imaging objective. The only light that reaches the collecting optics is that which has been scattered by objects within the sample. There are several experimental configurations which produce darkfield illumination. The first is referred to as reflection mode, and it is achieved by introducing the incident light at a shallow angle to the sample surface<sup>48, 137, 173</sup>. This configuration is illustrated in Figure 1A. Because of the shallow angle, the reflected beam is not collected by the imaging objective, so only light scattered by the sample surface is collected. While relatively simple to assemble, reflection mode darkfield is restricted to samples that have no reflective surfaces above

the scatterers, because this light may be collected by the objective. However, reflection mode does have the advantage of being able to image of samples on opaque substrates. For example, this technique has been used to collect micrographs of scattered light of gold nanospheres on a gold surface<sup>64</sup>. A similar configuration is the well-studied Kretschmann configuration which is commonly used for conventional planar SPR studies. Also known as total internal reflection, the Kretschmann configuration is applied when light is incident at a shallow angle through an index-matched prism on the back side of the sample<sup>172</sup>. Because of the lower refractive index of the medium above the substrate, the incident beam totally internally reflects providing the dark background necessary for darkfield. The evanescent field created at the point of total internal reflection excites nanostructures on the substrate, causing them to scatter light which is collected by the microscope objective as shown in Figure 1B. It is important to note that the purpose of the prism in this configuration is simply to provide a relatively high refractive index medium to facilitate total internal reflection of the incident beam and is not required to modify the momentum of the incident light to allow coupling into the electron resonance as in the case of conventional planar SPR. A third experimental means of achieving darkfield illumination is referred to as epi-illumination which involves using the imaging objective for both direction of the illumination light as well as collecting scattered light. As shown in Figure 1C, this is accomplished by using a beam-splitter to separate incident light with light reflected by the sample, which is then further separated by a field stop to isolate light scattered from the sample surface from reflected illumination light<sup>174</sup>. This approach is particularly useful for imaging structures under a confined environment that does not allow simple access by further optics to the sample surface such as those in flow a system, or an incubator for the imaging of live cells<sup>175</sup>.

The fourth approach that darkfield illumination is commonly achieved is through the use of commercially available darkfield condensers that focus collimated illumination light at an angle steeper than can be collected by the objective. Figure 1D shows an illustration describing transmission darkfield illumination. In this scheme, a darkfield condenser is used that brings in collimated light at an angle steeper than can be collected by the objective. This technique has been used by many groups<sup>76, 147, 165, 176</sup> including ours<sup>75, 80, 136, 171</sup>, to collect scattering spectra of individual nanostructures.

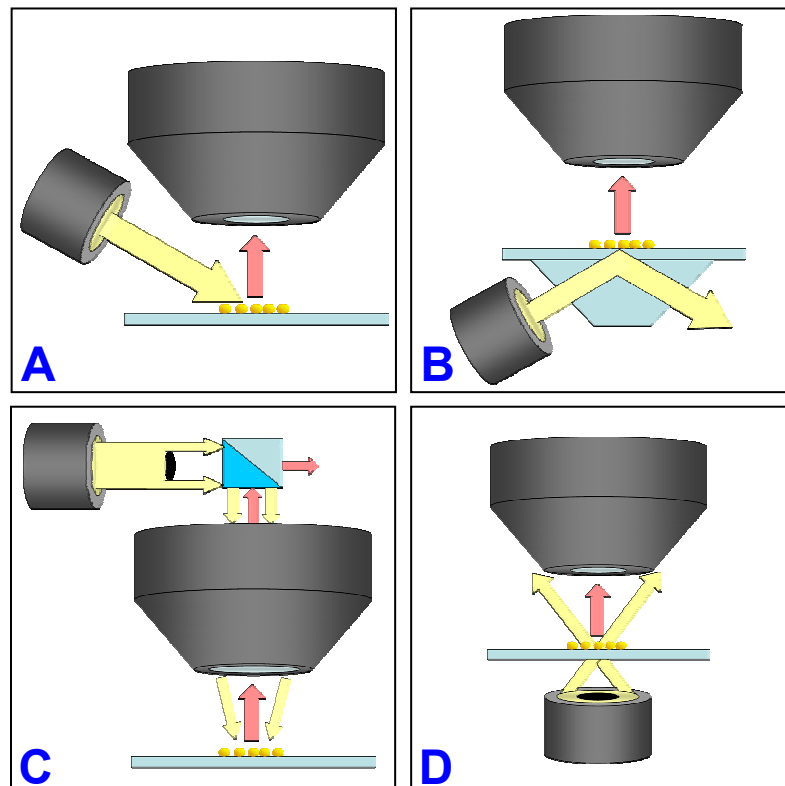


**Figure 1: Schematics of darkfield illumination techniques. Incident light and scattered light are depicted by yellow and red arrows respectively. A) Reflected Darkfield B) Total Internal Reflection (Kretschmann) configuration C) Epi-Illumination Darkfield D) Transmission Darkfield**

Because of their sub-wavelength dimensions, plasmonic nanostructures are imaged as diffraction-limited spots exhibiting the familiar and well-characterized Airy

pattern. Thus the resulting micrographs of nanoplasmonic structures under darkfield illumination are bright spots corresponding to light scattered by individual nanoparticles over a dark background, as seen in Figure 2. Although the nanostructure size is far below the typical resolution limits of optical microscopy, plasmon resonant nanostructures exhibit very large scattering cross sections. A scattering cross section represents a hypothetical disc around a nanoparticle such that all light incident upon that area is scattered. For example, a 30 nm diameter gold nanosphere has a scattering cross section of 90 nm<sup>2</sup> at resonance whereas a polystyrene bead with 30 nm diameter has a scattering cross section of approximately 0.1 nm<sup>2</sup> at visible wavelengths<sup>177</sup>. The large scattering cross section of plasmonic nanostructures is what allows the collection of high signal-to-noise images of individual nanoparticles with darkfield microscopy. In fact, individual nanoparticles scatter enough light that they can be easily visualized by eye through a darkfield microscope. As an example of digital recording, the micrograph of 80 nm diameter spherical gold nanoparticles shown in Figure 2 was collected with an integration time of 200 ms with a typical RGB (red-blue-green) CCD.

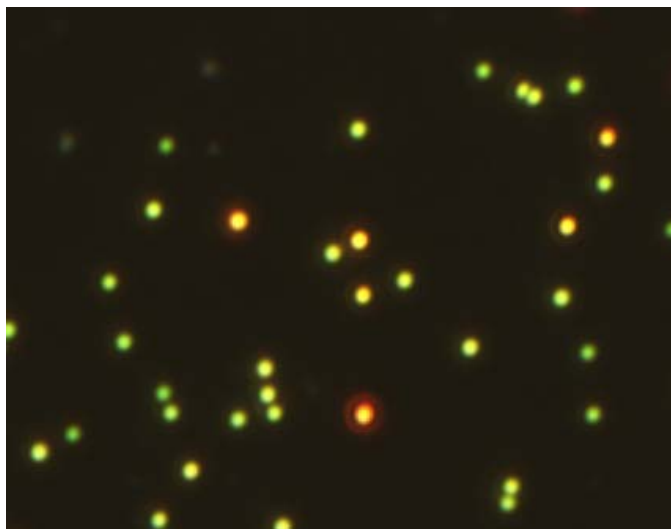


**Figure 2: Darkfield micrograph of 80 nm diameter gold spheres. The green dots are diffraction limited spots of light scattered by single gold nanospheres. The yellow and orange dots are spots from two or more aggregated spheres.**

## ***2.3 Microspectroscopy***

### **2.3.1 System Description**

The foundation of the optical darkfield microscopy system is a Zeiss Axiovert 200 inverted microscope. The system employs an oil immersion ultra-darkfield condenser (numerical aperture=1.2-1.4) and a 100x oil immersion Plan-neofluar® (Zeiss) objective (adjustable numerical aperture, from 0.7 to 1.3). Illumination is provided by an integrated 100W halogen source. A selectable output adapter is connected to the microscope's camera port that allows the field of view to be imaged by either a color digital camera (Photometrics CoolSnap cf) or a line-imaging spectrometer (Acton Research SpectraPro 2150i). The camera records the microscope's field of view for co-registration with the spectrometer. Gold nanoparticles are identified within the field of view as diffraction-limited spots exhibiting a Lorentzian scattering spectrum. A programmable shutter is mounted internal to the spectrometer entrance slit to electronically control exposure times. The slit was opened to 150  $\mu\text{m}$  to ensure that the entire diffraction pattern from a nanoparticle was imaged within the slit width. Further details of the optical setup are available in Appendix A. For time-resolved microspectroscopy measurements, a nanoparticle decorated cover glass was mounted in a flowcell (Biopetechs FCS3). All time-resolved measurements were taken under continuous flow conditions with a flow rate of approximately 1  $\mu\text{L/s}$ , controlled by a peristaltic pump (Rainin, Model RP-1). Temporal resolution of this microspectroscopy system is limited by spectral acquisition time, with a typical integration time of 2 s per spectrum for a gold nanosphere and 10 s for a single nanorod. All time-resolved microspectroscopy experiments employed a peak

centroid-fitting algorithm for precise and efficient data processing<sup>116</sup>. This algorithm performs a polynomial fit to the measured spectrum and then determines the centroid of the resonant scattering peak. This method offers increased precision in measuring LSPR shifts versus simply measuring the scattering peak wavelength, and has been shown to yield a peak position precision of  $< 5 \times 10^{-4}$  nm for bulk ensemble measurements<sup>116</sup>. Application of this technique to the single nanoparticle microspectroscopy system described in this chapter yields a fitting-limited peak measurement precision of 0.02 nm. The total experimental peak uncertainty is  $\sim 0.3$  nm, and is attributed to instrumental factors including spectrometer resolution, microscope focus control and physical stability and analytical factors including spectral source correction, spatial averaging and sample signal-to-noise-ratio (SNR)<sup>136</sup>.

### **2.3.2. Spectral Data Processing**

Spectral processing algorithms were developed in order to translate the raw data from the spectrometer to quantitative nanoparticle spectra. The primary focus of the algorithm was to produce reproducible spectra that can be quantitatively compared across measurements. The primary hurdle in this process was correcting for the spectral density of the light source to excite the particles. The raw nanoparticle scattering spectrum collected by the spectrometer is modulated by the spectral density of the incident light. Commonly, this can be corrected for by simply measuring the spectrum of the light source and dividing the measured spectra element-wise by this source spectrum. However, to ensure accurate, it is necessary to perform this source collection under the exact same conditions as the experiments to be conducted. Darkfield illumination, however by definition, precludes the ability of illumination light to be directly collected by the imaging optics. Scattering standards are commercially

available that can be use to collect source spectra for reflected mode darkfield. However, transmission darkfield would require a standard that both scatters and allows light to be transmitted through the sample. Also, experiments conducted under flow conditions would require different source spectra to be collected for each introduced solution as the changes in refractive index of the solutions can alter transmission and reflectance of the surfaces in the optical path of the illuminating light. For this reason, an intrinsic source correction method was sought that enabled correction internal to each collected spectroscopic image. Also, for an imaging spectroscopic method, it is important that the source spectrum be spatially resolved, as different regions of the field of view could receive a different spectral intensity of illumination light.

Figure 3 illustrates the concept of intrinsic source correction developed and used for the following experiments. The two rainbow-colored spots are spectra of two particles that were images on the spectrometer entrance slit. First, the entire image is dark corrected by subtracting an image acquired for the same amount of time, but with no light incident to the spectrometer. Each bright spot is automatically identified by thresholding the entire image. Each particle spot is analyzed by first identifying which pixel rows correspond to the given particle. In the example in Figure 3, spectral lines within the yellow box were considered as contributing to the top particle spot. Background regions are then identified several pixels away in both directions. The red boxes denote which areas are considered background. The background rows are then averaged and smoothed by running average to decrease noise introduced during the source correction division. This smoothing is justified as the light source is a blackbody radiator, which should have a smooth spectral line-shape. This smoothing is an important requirement of the algorithm because by definition, darkfield imaging has low

signal in the background area. Thus, signal will be low and therefore noisy in this region. However, enough light does make it through the system that a spatially consistent source spectrum can be determined.

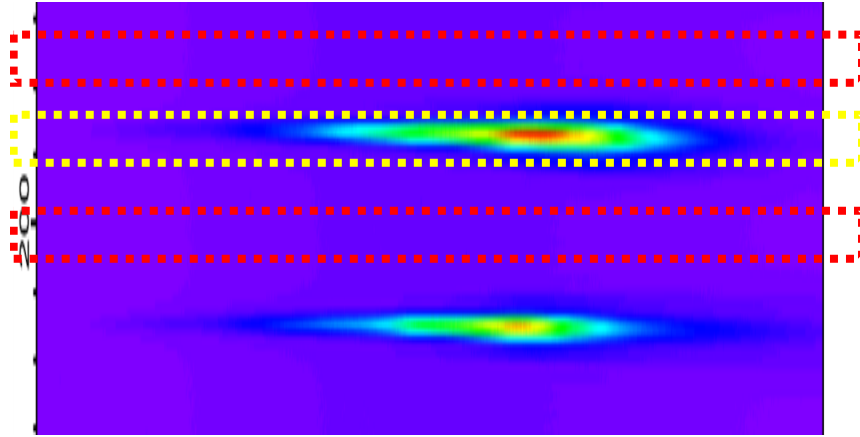


**Figure 3: Illustration of intrinsic source correction. For the top nanoparticle scattering spot, the yellow box denotes which rows are considered part of the spectrum. The red boxes denote which regions would be used to collect a source spectrum for spectral correction.**

To test the effectiveness of the intrinsic source correction algorithm, a single 80 nm diameter gold sphere was measured 30 times on different locations of the entrance slit. All spectra used the same dark image, and each used the intrinsic source spectrum from within its own image as described above. Figure 4 is a plot of all 30 spectra with their intensity normalized. A least-squares fit to a Lorentzian curve was applied to each spectrum. Before further optimization, the standard deviation of the peak wavelength as was 0.5 nm. The SNR of the corrected spectra are ~120.

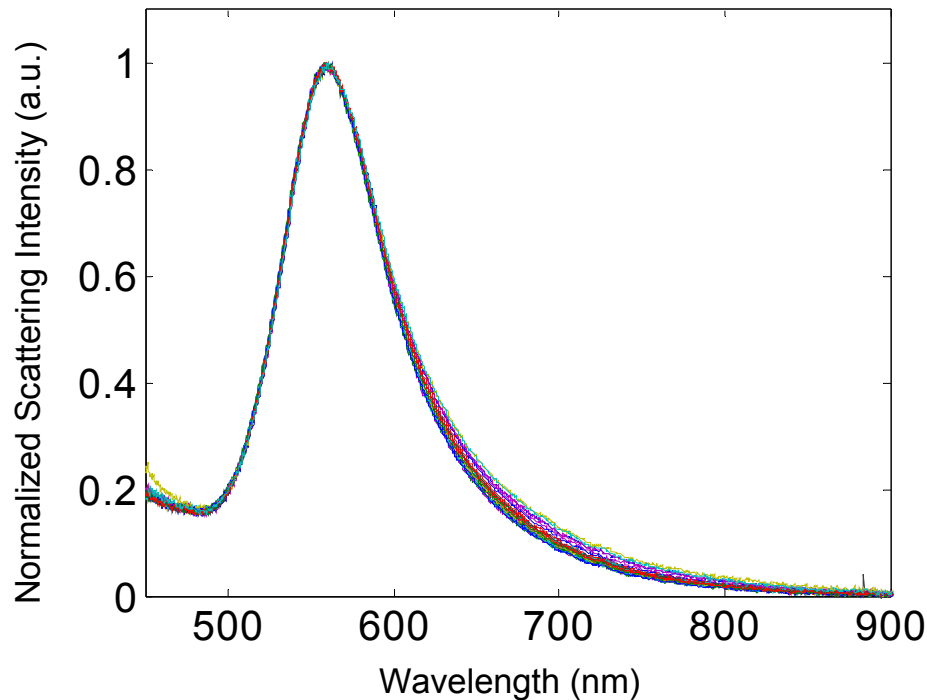


**Figure 4: Normalized scattering spectra of the same 80 nm diameter gold sphere measured 30 times and source corrected using the intrinsic source correction method described above.**

### **2.3.3 Spectral Measurement Analysis**

The goal of the microspectroscopy system is to measure the LSPR spectra as accurately as possible. More specifically, the goal is to measure wavelength shifts in the resonant peaks as accurately as possible as these are the signals directly generated upon analyte binding. A full characterization of factors that contribute to the LSPR peak measurement uncertainty was carried out in order to understand the fundamental limits of the microspectroscopy system and to optimize those system parameters to minimize the measurement uncertainty<sup>136</sup>. This assessment was performed in collaboration with recent graduate Adam Curry. The full details of this work are available in the article first-authored by Curry which is presented in appendix A. In this section, a summary of

these results are presented as they relate to the work presented in this thesis, with a focus on the specific contributions by Nusz.

We considered both instrumental and analytical contributions to peak measurement uncertainty. Instrumental factors include objective NA, objective magnification, spectrometer slit width, NP image position ( $X$ ,  $Y$ ) relative to the spectrometer entrance slit, and objective focus (or  $Z$  position of the particle, relative to the objective). Analytical factors include the extent of spatial averaging within the collecting CCD, the image region used for source spectrum determination, the signal-to-noise ratio (SNR) of the source-corrected spectrum, and the peak fitting algorithm employed.

Many of the instrumental sources of measurement uncertainty are derived from the microscopy components. Nanoparticles can be imaged with conventional optics only as diffraction-limited spots, because of their sub-wavelength dimensions. For a simple lens, the spectral and spatial distributions of diffraction-limited spots are defined by the familiar Airy pattern. Because of the wavelength dependence of diffraction, longer wavelengths have a larger Airy disk, resulting in a radial dependence of the spectral content of the diffraction-limited spot. The size of the spot on the image plane is determined by both the NA and the magnification of the imaging objective. Larger NA values result in smaller spots, while larger magnification values result in larger spots. Additionally, the Airy pattern only results when the subject is perfectly in focus. Deviations in the objective focus distance will also alter the spatial distribution of the spectral density within the spot.

The remaining instrumental sources of uncertainty are derived from components of the spectroscopy portion of the system. In standard spectroscopy applications, the

size of the spectrometer entrance aperture is a determinant of spectral resolution. However, in the case of dark-field imaging of a diffraction-limited spot that is smaller than the aperture, the size of the imaged spot itself acts as the entrance aperture and enters into the calculation of spectral resolution. This is because the regions surrounding the particle are dark, contributing little broadening to the measured peak. However, spectral uncertainty still exists to the degree that there is uncertainty in the spot position relative to the center of the entrance slit which will be measured as an overall wavelength shift of entire spectral peak. But the loss of spectral resolution typically expected from increasing the size of the entrance slit will be less than that predicted by the spectrometer aperture alone. Given these considerations, the spectrometer's entrance aperture size must be optimized to account for spot size, spectrometer resolution, and positioning uncertainty.

In order to quantify the uncertainty to the overall peak position that each potential factor contributes, both theoretical models and empirical measurements were made. Instrumental contributions were analyzed by making 50 repeated measurements of single nanoparticles at configurations in which the following instrumental component was altered at a time: (1) objective magnification; (2) focus height; and (3) entrance slit width. These results were compared to theoretical models generated in Matlab that simulate the effects of each of the three components on the spectral distribution of the point-spread function of a diffraction-limited spot and on how the light within this spot reaches the detector for measurement. The analytical factors of spatial averaging and source correction were optimized by varying these parameters in analysis of experimental data and minimizing output variance. Uncertainty introduced by peak fitting and SNR of the initial spectrum were determined by applying them to computer-generated LSPR spectra

of various nanoparticles and artificially adding noise and comparing the peak location as determined from the fitting algorithm versus the input into the spectrum-generating code.

The results of this assessment are the optimized parameters for the microspectroscopy system. The results indicate that minimum peak location uncertainty is obtained by using a 100X objective with an entrance slit width of 150  $\mu\text{m}$ . The resulting measurement uncertainty is 0.3 nm which presents the fundamental detection of peak shifts that can be reliably measured by the described microspectroscopy system.

### 3 Gold Nanorod Biosensor

In this Chapter, I describe the use of gold nanorods as plasmonic transducers; we chose gold nanorods as plasmonic transducers of biomolecular binding events for two reasons: first, we chose gold over silver, even though silver particles exhibit a higher bulk refractive index sensitivity than gold particles of the same shape and size<sup>178</sup>, because the greater reactivity of silver as compared to gold makes it less suitable for use in biologically relevant media. Second, we chose nanorods over many other possible shapes because gold nanorods can be conveniently synthesized to exhibit plasmon bands with peak wavelengths ranging from 600-900 nm simply by tuning their aspect ratio and size through chemical synthesis methods<sup>179</sup>.

This wavelength range is attractive for optical biosensing for many reasons. Recent simulations by Miller and Lazarides have shown that the bulk refractive index sensitivity of the plasmon band is linearly correlated with the wavelength of the LSPR peak for particles of a specified composition<sup>142</sup>, so that nanoparticles with a plasmon band at higher wavelengths are more sensitive to their local environment than those at shorter wavelengths. In view of this finding, we chemically synthesized nanorods with dimensions of 74 nm x 33 nm ( $l \times w$ ) with a longitudinal plasmon band with a peak wavelength of 780 nm to maximize their sensitivity to their environment while remaining in the visible wavelength range. The choice of rods with a scattering peak wavelength centered at ~780 nm is also advantageous because the background absorption and scattering of endogenous chromophores from biological mixtures (e.g., serum and blood) is minimal in this wavelength range.

## **3.1 Sensor Fabrication and Detection Methods**

### **3.1.1 Materials**

Hydrogen tetrachloroaurate trihydrate (HAuCl<sub>4</sub>), sodium borohydride, ascorbic acid, phosphate buffered saline (PBS) tablets, and mercaptohexadecanoic acid (MHA) were purchased from Sigma. Glass coverslips, sodium citrate, glycerol, sodium hydroxide, ethanol, methanol, sodium chloride (NaCl) and hydrochloric acid were purchased from VWR. Cetyltrimethylammonium bromide (CTAB) was purchased from Fluka. (+)-biotinyl-3,6,9-trioxaundecanediamine (biotin-amine), *d*-biotin, 1-ethyl-3-(3-dimethylaminopropyl) carbodiimide (EDC), N-hydroxysuccinimide (NHS), and streptavidin were purchased from Pierce. (1-mercaptoundec-11-yl)tri(ethylene glycol) (EG3SH) was purchased from Prochimia. Aminopropyltriethoxysilane (APTES) and mercaptopropyltriethoxy-silane (MPTES) were purchased from Gelest. Distilled water purified by a reverse-osmosis filtration system (18 MΩ-cm, Myron L Company, Series 750) was used for all experiments.

### **3.1.2 Nanorod Synthesis**

Gold nanorods were chemically synthesized by a seed-mediated growth procedure<sup>50, 179</sup>. Spherical gold seed particles were synthesized as follows: to a mixture of 7.5 ml of 0.1 M CTAB in water and 0.250 ml of 0.01 M HAuCl<sub>4</sub>, 0.6 ml of ice-cold 0.01 M NaBH<sub>4</sub> were added under vigorous stirring. The yellow solution turned brown in color, and was then stirred over gentle heat for a few minutes. Gold nanorods were synthesized in a water bath at 29°C, as follows. To 95 ml of 0.1M CTAB in water, 4 ml of 0.01M HAuCl<sub>4</sub>, 0.6 ml of silver nitrate, and 0.64 ml of 0.1M ascorbic acid were added. The mixture was swirled after the addition of each reactant to ensure mixing. 50 μl of gold seeds were added, the mixture was swirled and inverted, and then allowed to sit

overnight, resulting in a purple-colored suspension of gold nanorods. Excess CTAB was removed from the gold rod suspension by centrifugation twice at 4500 rpm for 30 min. The gold nanorods were resuspended in water to a total volume of 10 ml and stored at room temperature until further use. The nanorod dimensions used in refractive index sensitivity tests described below were  $74 \pm 9$  nm in length and  $33 \pm 6$  nm in diameter ( $n > 100$ ) as measured by TEM of the nanorods Figure 5 is a transmission electron micrograph of the nanorods used for these studies.

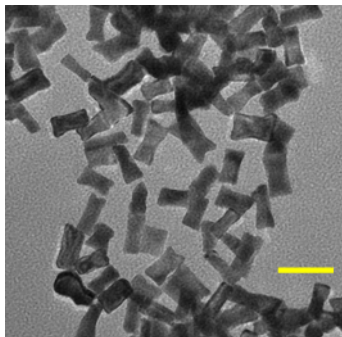


**Figure 5: TEM of gold nanorods used in the characterization of the microspectroscopy system and also used for subsequent biomolecular detection experiments. Scale bar indicates 100 nm.**

### **3.1.3 Substrate Preparation**

Glass substrates were prepared as described in section 3.1. The only difference is that cover glasses intended for nanorod immobilization then incubated in a solution of 10% (v/v) MPTES in ethanol for 15 min. The thiol end-group of the MPTES provides the chemical bond to the gold nanorod surface. In order to compare single nanoparticle measurements to previously reported ensemble measurements<sup>70, 72</sup>, glass slides treated with MPTES were incubated overnight in suspension of the gold nanorods.

### 3.1.4 Receptor Conjugation

First, centrifuged gold nanorods were chemisorbed onto the MPTES-treated glass substrate. The immobilized nanorods were then incubated in an ethanol solution of 0.5 mM (1-mercaptoundec-11-yl)tri(ethylene glycol) (EG<sub>3</sub>SH) and 0.5 mM mercaptohexadecanoic acid (MHA) which forms a mixed SAM with dual functionality: the MHA provides a moiety to which biotin-amine can be conjugated via EDC/NHS coupling and the EG<sub>3</sub>SH prevents non-specific adsorption of protein molecules to the surface of the nanorod. Biotin was conjugated to the nanorods by incubating the SAM functionalized nanorods in an aqueous solution of 0.4 M EDC and 0.1 M NHS for 7 minutes to convert the COOH groups to NHS esters. The chips were rinsed with water, and were then immediately incubated in biotin-amine for 2 h, and rinsed with water again.

### 3.1.5 Experimental Methods

The glass substrate with biotin-conjugated nanorods was mounted in the flow-cell of the microspectroscopy system. Streptavidin solutions at various concentrations in PBS were flowed through the cell at a constant flow rate for 2 h. LSPR shifts were measured as the difference between the  $\lambda^*$  of fits to the measured scattering spectra. To ensure the observed LSPR shifts resulted from specific interaction between biotin and streptavidin, controls for the binding experiments were performed by incubating biotin-functionalized gold nanorods in streptavidin solution that had been pre-saturated with excess (1mM) free biotin.<sup>75</sup> Control binding studies were performed identically as those described above except that pre-saturated streptavidin incubation was also performed in the presence of excess (1mM) free biotin.

### 3.2 Gold Nanorod Spectral Analysis

Figure 6A shows a darkfield micrograph of nanorods immobilized on glass acquired on the microspectroscopy system. The darkfield micrograph shows diffraction limited spots corresponding to light scattered by individual nanoparticles. Figure 6B shows a typical scattering spectrum of a single nanorod that is obtained on the darkfield microspectroscopy system, and shows the high SNR of 80 and low FWHM of ~60 nm that is obtained for an isolated gold nanorod by single particle spectroscopy with an acquisition time of 10 s. The FWHM of 60 nm of these nanorods is narrower than other nanostructures that also have a plasmon band in this wavelength range such as gold nanoshells<sup>180</sup>, which allows for more accurate determination of peak shifts, and is a useful spectral feature of these nanorods as plasmonic transducers.

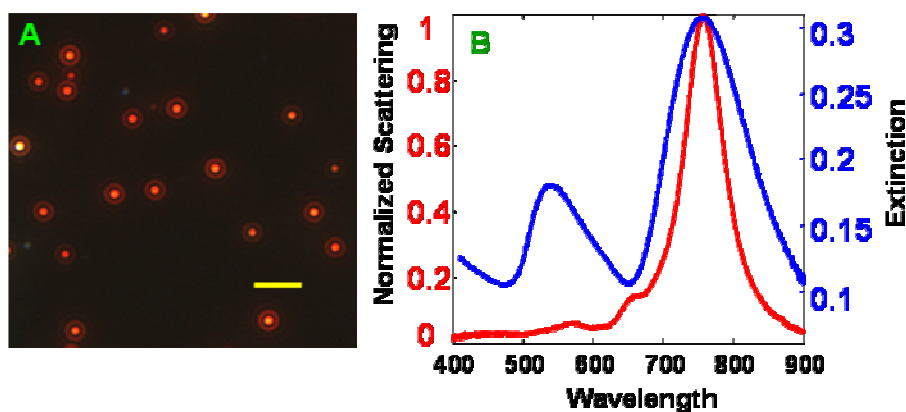


**Figure 6: A) Darkfield micrograph of gold nanorods. B) Scattering spectra of an ensemble of gold nanorods on a glass substrate (blue) and of a single gold nanorod (red).**

This figure also highlights an important spectroscopic advantage (albeit at the cost of more complex instrumentation), by comparing the scattering spectrum of a single immobilized gold nanorod (Figure 6B red curve) with the extinction spectrum of an ensemble of ~108 nanorods from the same synthesis batch immobilized on glass (Figure

6B blue curve), as measured by a UV-vis spectrophotometer (Cary 300-Bio). The ensemble spectrum exhibits heterogeneous broadening compared to the single Lorentzian peak observed for each resonance of a single nanoparticle. This broadening is simply due to the fact that even the most careful chemical synthesis will yield nanoparticles with a distribution of size and shapes, and as the LSPR behavior of a nanoparticle is strongly dependent upon these structural parameters, this structural inhomogeneity leads to a broadening of the ensemble LSPR peaks. Additionally, the location and amplitude of smaller scattering peaks corresponding plasmonic resonances other than the longitudinal resonance of the nanorod are observed. The location and magnitude of these minor peaks has been shown to be highly dependent on nanorod end cap geometry and thus tends to vary widely between chemically synthesized nanorods<sup>143</sup>.

### **3.2.1 Bulk Refractive Index Sensitivity**

The bulk refractive index sensitivity of a plasmonic nanostructure is defined as the wavelength shift of a LSPR peak in response to the change of the refractive index (RI) of the surrounding bulk medium in units of nm/RIU (RIU: refractive index unit). Single nanoparticle bulk refractive index sensitivities are experimentally determined by the slope of a linear fit to a plot of LSPR peak wavelength versus surrounding RI. This parameter was determined by measuring the scattering spectrum from a single nanorod that was immobilized on glass in water and in solutions containing 0, 20, 40, 60, and 80 percent glycerol (v/v) in water. The refractive index of these solutions is 1.33, 1.36, 1.38, 1.40, and 1.42 respectively. Figure 7 shows spectra of an individual gold nanorod as the refractive index is increased.

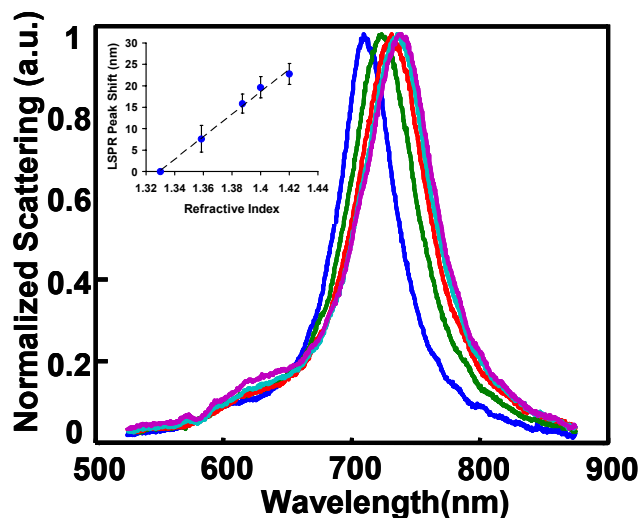


**Figure 7: Normalized scattering spectra of a single gold nanorod as the refractive index of the surrounding medium is changed to 1.33 (blue), 1.36 (green), 1.38 (red), 1.40 (cyan) and 1.42 (purple). Inset shows a plot of LSPR peak shift versus surrounding RI for 15 nanorods (error bars represent 95% confidence interval) yielding a fit with a slope of 262 nm/RIU.**

The LSPR peak wavelength shift of 15 nanorods was averaged and plotted for the five test solutions. The slope of a linear fit to this line is the refractive index sensitivity of gold nanorods and was determined as shown in the inset to Figure 7. The sensitivity of the rods used in this study was  $261.7 \pm 26.9$  nm/RIU ( $n=15$ ). This value determined by single nanorod measurements is in good agreement with the previously reported sensitivity of 252 nm/RIU measurements from an ensemble of gold nanorods with the same nominal dimensions<sup>72</sup>. These data highlight that rods are attractive as optical transducers that work in a wavelength sensing mode, because their mean bulk refractive index sensitivity of 262 nm/RIU is significantly greater than that of 39 nm diameter gold spheres<sup>71</sup> (70 nm/RIU), and gold nanoshells ( $\sim 140$  nm/RIU)<sup>56</sup> that have a similar wavelength maximum of the plasmon band around 700 nm.

The large variability noted in refractive index sensitivity is believed to be caused by several reasons. The largest variations are a result of nanoparticle size variations

resulting from the chemical synthesis technique. These geometric variations result in a corresponding distribution of nanoparticle sensitivities since nanoparticle sensitivity has been shown to be directly correlated to LSPR wavelength<sup>142</sup> and LSPR wavelength is directly determined by nanoparticle shape<sup>48, 137-141</sup>. Additionally, remaining CTAB on the surface of some of the nanorods could affect the measured sensitivity of the nanorod. CTAB was rinsed from the nanorod suspensions by centrifugation and resuspension. If additional rinses cycles were performed, the nanorods would aggregate and fall out of suspension<sup>72</sup>. Thus, a critical amount of CTAB is required to keep the nanorods in stable suspension. We believe that small amounts of CTAB remain on some of the particles, restricting the active sensing volume accessible for sensitivity measurements as well as binding experiments.

### **3.2.2 Time-Resolved Spectroscopy**

Time resolution is an important aspect of a biomolecular detection system. In order to gauge the nanorod LSPR sensor in the time domain, real-time measurements using this microspectroscopy system under dynamic flow conditions by immobilizing gold nanorods on an MPTES-treated coverglass mounted on in a flow cell (Bioptechs FCS3). The scattering spectra were then recorded as a function of time as the medium surrounding the nanorods was exchanged. All time-resolved microspectroscopy experiments employed the intrinsic source correction algorithm discussed above. A centroid-fitting algorithm developed by Dahlin and Hook was employed for precise and efficient data processing of peak shifts<sup>116</sup>. Spectra were collected every 10s as the medium surrounding the nanorods was exchanged from 0, 20, 40, 60 and 80 percent glycerol (v/v). The centroid of the LSPR peak a single gold nanorod is plotted versus time in figure 8. Solution was continuously flowing at a slow rate through the flow cell

over the sample using a peristaltic pump. Every 20 minutes, the source solution was changed. At time  $t = 100$ , water was rapidly flushed through the system. These experiments were a pain in the ass. Plateaus are visible for the 0, 20, 40 and 60 percent glycerol solutions. The exchanges between plateaus mark the transition of the effective refractive index surrounding the nanoparticles. No plateau is reached for the 80 percent glycerol solution because insufficient time was allowed to reach equilibrium before the chamber was washed.

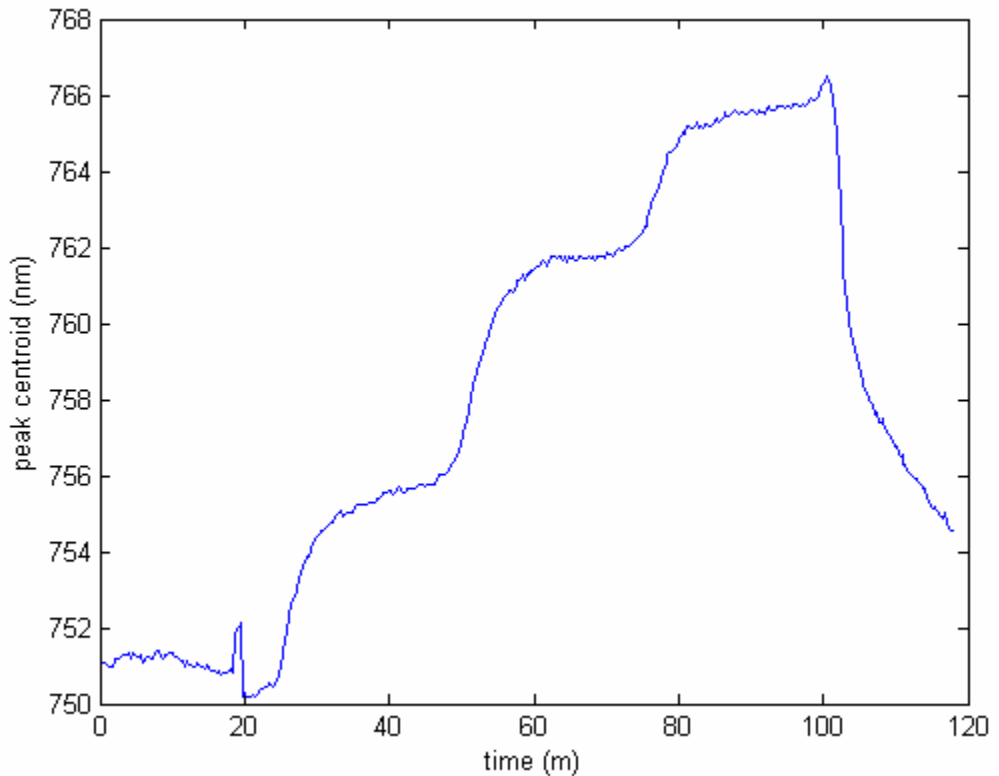


**Figure 8: LSPR peak centroid of a single gold nanorod as the surrounding refractive index is increased incrementally every 20 minutes.**

### **3.2.3 Polarization Dependence of Nanorod LSPR**

The shape and size of a nanoparticle determines the quantity of electrons oscillating, the direction and magnitude of the restoring force, and thus the overall

geometry of the plasmon resonance. Cylindrical nanorods have been shown to exhibit two distinct resonances when illuminated with unpolarized light– corresponding to excitation along the longitudinal and transverse dimension<sup>46</sup>. The light scattered by each resonance is polarized in the dimension over which the dimension occurs. Since these the corresponding resonances occur perpendicularly, their respective scattered photons are polarized perpendicularly to one another. It has been shown that the orientation of individual nanorods can be determined by observing the relative polarization of light scattered by individual nanorods<sup>47</sup>. In the experiments cited, darkfield illumination used to image gold nanorods on a surface. The image is sent through a birefringent crystal such that the resulting final image is actually a superposition of two side-by-side images, each reporting the intensity of perpendicular polarization. Since the scattering intensity is dominated by the longitudinal resonance, the nanorod orientation can be calculated by determination of the relative intensity of the two polarization-dependent spots. In an effort to test the efficacy of the microspectroscopy system, spectra were collected of scattered light from single nanorods that were sent through a rotatable polarizer. Spectra were taken at 15 degree increments of the polarizer rotation. Results from a single nanorod are shown in Figure 9. The blue line shows the spectrum of light scattered by the nanorod without the introduced polarizer. Peaks according to the two primary resonances are clearly visible – longitudinal (along the rod length) at ~ 800 nm and transverse (across the rod diameter) at ~640 nm. The green line is the spectrum from the series collected that had the most intense longitudinal peak. This occurred at an angle of 210 degrees from the system zero rotation. Note the relatively minimal contribution from the transverse peak. The red line shows the spectrum with the polarizer at 300 degrees from normal - 90 degrees with respect to that which generated

the green line. In the red spectrum, the transverse peak is the most pronounced whereas contributions from the longitudinal peak are minimal. Smaller peaks in the resonance result from deviations in the particle from an ideal cylinder such as end-cap geometry<sup>181</sup>. Similar results were noted at 30 degrees and 120 degrees (results not shown) as would be expected.

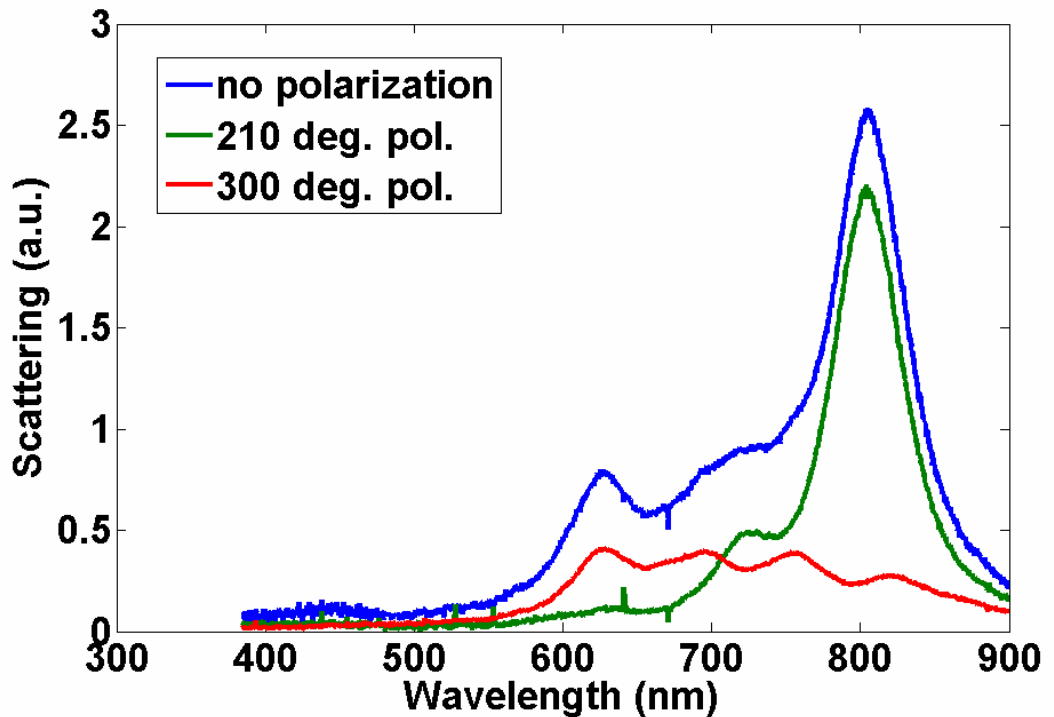


**Figure 9: Scattering spectra of a single nanorod exhibiting the polarization dependence of each resonance. The blue line is the unpolarized scattering showing both the transverse resonance around 640 nm and the longitudinal peak near 800 nm. The green and red lines are the scattering spectra collected with the polarizer at 90 degrees with respect to each other.**

### **3.3 Biodetection with Individual Gold Rods**

This section describes the use of individual gold nanorods as plasmonic transducers to detect the binding of streptavidin to individual biotin-conjugated nanorods in real time on a surface. Label-free detection at the single nanorod level was performed

by tracking the wavelength shift of the nanorod localized surface plasmon resonant scattering spectrum using a darkfield microspectroscopy system. The lowest streptavidin concentration that was experimentally measured in these proof-of-concept experiments was 1 nM which is a factor of 1000-fold lower than the previously reported detection limit for streptavidin binding by biotinylated single plasmonic nanostructures. Binding of streptavidin at 1nM concentration induces a mean resonant wavelength shift of 0.59 nm suggesting that we are currently operating at close to the limit-of-detection of the system.

### **3.3.1 Static Biodetection**

Figures 10a and 10b show three representative spectra collected from a streptavidin binding experiment. The first spectrum was collected before conjugating biotin to the nanorods, and the second spectrum was collected after biotin was conjugated to the nanorods. The first two spectra are useful diagnostics of the efficiency of biotin conjugation to a gold nanorod. From previously reported ensemble studies, it has been observed that successful biotin conjugation onto nanorods increases the refractive index surrounding the nanoparticles and induces a reproducible red shift in the LSPR peak<sup>71, 72</sup>. The 5.6 nm shift observed after biotin conjugation indicates successful coupling of the biotin to the nanorod. The third spectrum was collected after the nanorod was incubated in a solution of 130 nM streptavidin. The resulting 5.2 nm shift indicated that streptavidin binding occurred on the surface of the biotinylated nanorod. We conclude that the nanorod sensor saturated at this concentration because incubation with higher concentrations of streptavidin resulted in identical LSPR shifts (data not shown).

In order to probe the system detect limit, measurements were taken of biotinylated gold nanorods in streptavidin concentrations of 130nM, 10nM and 1nM. A mean LSPR centroid shift of  $5.29 \pm 1.47$  nm (95% CI, n=9) was observed upon introduction of the 130 nM streptavidin solution. A LSPR peak centroid shift of  $1.22 \pm 0.24$  nm (95% CI, n=8) was measured from 10 nM streptavidin, and  $0.588 \pm 0.32$  nm (95% CI, n=9) for 1 nM streptavidin.

Figures 10c and 10d show the results of a control experiment using biotin-saturated streptavidin. The spectra shown are of a single gold nanorod before biotin conjugation, after biotin conjugation, and after incubation with biotin-saturated streptavidin. The characteristic ~5 nm LSPR shift resulting from the biotin coupling was observed, consistent with the previous experiment, which indicated that biotin was successfully conjugated to the gold nanorods. However, there was no further shift in the LSPR peak centroid upon incubation with the biotin-saturated streptavidin (Figure 10a,b), which clearly demonstrated that the saturation of biotin-binding sites on the streptavidin prevents binding of streptavidin to the biotin-functionalized nanoparticle surface. These results also suggest that the mixed SAM on the nanorod surface successfully prevented nonspecific adsorption of streptavidin because the streptavidin molecules did not non-specifically adsorb to the nanorods when their biotin-binding sites were blocked. Together, these results strongly suggest that the measured LSPR shifts observed for streptavidin binding to the biotin-functionalized nanorods are caused by molecular recognition of biotin by streptavidin.

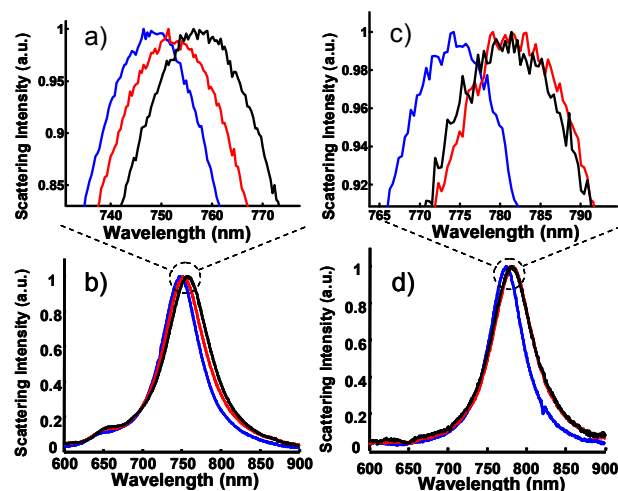


**Figure 10: (a,b) Scattering spectra of a single gold nanorod after sequential incubation in EG3SH/MHA (blue), biotin (red) and 10 nM streptavidin (black). (c,d) Scattering spectra of a single gold nanorod in EG3SH/MHA (blue), biotin (red) and 100 nM streptavidin pre-saturated with free biotin (black).**

### 3.3.2 Time-Resolved Biodetection

The time-resolved spectral acquisition mode of the microspectroscopy system was used to measure the kinetics of streptavidin binding to biotin-conjugated nanorods. Figure 11 shows a plot of the LSPR scattering peak centroid versus time for single biotin-conjugated nanorods incubated in 130 nM, 10 nM, and 1 nM. A rapid 5.10 nm shift in the LSPR scattering peak centroid was observed upon introduction of the 130 nM streptavidin solution. After rinsing with PBS at time  $t = 100$  min, the peak centroid location remained constant, which demonstrated the irreversibility of the biotin-streptavidin binding, and is consistent with the long ( $\sim 35$  h) half-life of the biotin-streptavidin bond<sup>182, 183</sup>. A steady state LSPR peak centroid shift of 1.09 nm was observed for streptavidin binding at a concentration of 10 nM. Finally, a shift of 0.48 nm was observed from a biotin-conjugated nanorod after incubation in streptavidin concentration of 1 nM. This shift is close to the limit of detection of this system, which we estimate to be  $\sim 0.3$  nm<sup>136</sup>.

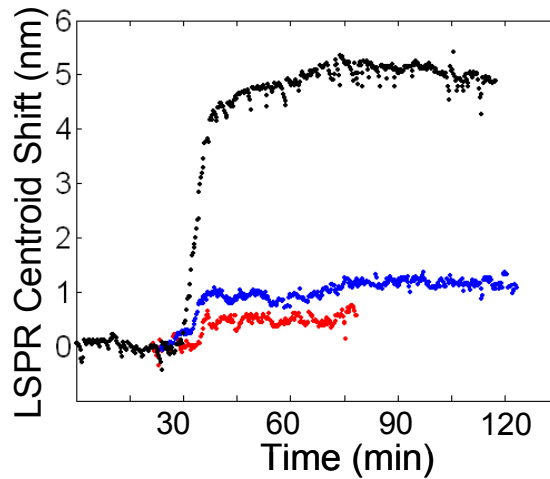


**Figure 11: Real-time measurement of the LSPR scattering peak centroid shifts of single biotin-conjugated gold nanorods incubated in 130 nM (black), 10 nM (blue) and 1nM (red) streptavidin in PBS.**

### **3.4 Conclusions**

This work represents an advance in the field of plasmonic biosensors for three reasons. First, the detection of streptavidin at a concentration of 1 nM, which is a factor of 1000-fold lower than the previously reported minimum detectable streptavidin concentration by single plasmonic nanostructures<sup>147</sup>. The steady state binding of 1 nM streptavidin corresponds to a mean LSPR peak shift of approximately 0.59 nm and we estimate the current limit-of-detection at 0.3 nm. Second, we show the advantages that single nanostructure experiments have over ensemble measurements that offer similar limits of detection in terms of concentration of analyte. This is because ensemble experiments utilizing a conventional spectrophotometer with a beam illumination area of 1 mm<sup>2</sup> provide an averaged signal from approximately 10<sup>8</sup> nanoparticles, making stochastic measurements virtually impossible. Finally, these single nanorod measurements were carried out in a time-resolved mode, which is critical to developing

this technology to the ultimate, and as yet unattained goal of observing the dynamics of single molecule binding events in real-time on a single nanoparticle.

## 4 Gold Nanorod Optimization

To further understand the mechanisms of plasmonic biosensors, investigators have been studying the specific details of plasmonic nanostructures that are responsible for their use in sensors such as the distance dependence of sensitivity<sup>118, 119, 184</sup> and the resonant electric field enhancement distribution.<sup>59, 82</sup> However, to date, these developments have not been integrated into a coherent quantitative framework that allows the effect of these parameters on relevant figures-of-merit of biosensors such as their limit-of-detection and dynamic range to be predicted.

Motivated by the goal of rationally designing LSPR sensors, in this chapter we integrate recent progress in understanding the structural details of metal nanoparticles that control their plasmonic behavior with various measurement system parameters that impact measurement uncertainty into a quantitative model that is capable of predicting the response of a single, receptor-functionalized nanoparticle to discrete analyte binding events. The result is an analytical model that quantifies the LSPR shift of a gold nanorod caused by the local refractive index increase from the presence of a target biomolecule. The principle of this work is similar to that of Stenberg *et al.* who describe an analytical model to quantify the surface concentration of bound protein on plasmon resonant planar gold<sup>185</sup> and to that of Vollmer *et al.* who estimate the surface density of bound proteins based on wavelength shifts of a resonant microcavity.<sup>186</sup>

The utility of this model is two-fold. First, it provides an analytical model that allows *a priori* design of a LSPR sensor with figures-of-merit such as the molecular detection limit (MDL) and dynamic range that can be analytically calculated completely as a function of sensor components for a given receptor-analyte pair. Because the model calculates LSPR shifts for individual bound molecules, the MDL is defined as the

smallest number of bound molecules that is measurable by the system, and the dynamic range is the maximum number of detectable molecules. To illustrate its experimental utility, the model was used to identify the optimal gold nanorod geometry (length and width) that was predicted by the model to yield the lowest MDL for the detection of streptavidin by gold nanorod LSPR sensors. A LSPR sensor was fabricated from biotin-functionalized gold nanorods and the experimental results were compared with the prediction of the model to investigate its accuracy. Second, this model is useful because it allows the contribution of different system parameters to overall sensitivity to be individually parsed. With the ultimate goal of label-free, single molecule detection by LSPR sensors, we conclude with a discussion of optimization of the system within realistic physical and current technological constraints that might allow the fabrication of an LSPR sensor and dark-field microspectrometer that are capable of detecting the binding of individual analyte molecules.

#### ***4.1 Model Development***

As a first approximation, the MDL of nanoparticle sensors is determined by their composition, size, and shape of the NPs. Recognizing that the development of a generalized model that could account for the dependence of the MDL of a LSPR sensor on all of these parameters was likely to prove computationally intensive and possibly intractable, we focused instead on developing a model that was applicable to gold nanorods as plasmonic transducers of binding events for the following reasons. First, although silver particles are more sensitive than gold particles of the same shape and size,<sup>178</sup> the greater reactivity of silver as compared to gold makes it less suitable for use in biologically relevant media as silver can be easily oxidized, altering the plasmonic behavior of the particle. Second, gold nanorods can be conveniently synthesized with a

range of dimensions via established chemical synthesis methods, which allows the model to be experimentally tested –and the sensor optimized– at the structural level.<sup>72, 179, 187</sup> Third, gold nanorods can be conveniently synthesized to exhibit plasmon resonances with peak wavelengths ranging from 700-900 nm and beyond simply by tuning their aspect ratio and size.<sup>179, 188-191</sup> This spectral region is particularly useful for biosensing because the background absorption and scattering of endogenous chromophores from biological mixtures (e.g., serum and blood) and of water are minimal in this wavelength range.<sup>192, 193</sup> We note that LSPR of several other geometries of gold nanoparticles such as nanoshells, nanodiscs<sup>194</sup> and nanorings<sup>195</sup> can also be tuned via synthesis methods to exhibit plasmon bands in the wavelength range of gold nanorods. Nanorods, however, have a higher bulk RI sensitivity<sup>56</sup> and also a narrower linewidth than these geometries<sup>180, 194, 195</sup> which allows more accurate determination of peak shifts as described later in the model details. Additionally, the line-widths of gold nanorod scattering spectra have been shown to be a function of the length and aspect ratio of the gold nanorods<sup>196</sup> as well as end-cap shape<sup>143</sup> - parameters that can be controlled in their chemical synthesis.

We sought to develop an analytical model that estimates the MDL of a LSPR sensor for a specific analyte-receptor pair based on the geometric dimensions of the gold nanorod using the spectral detection system described in Chapter 3. Thus, the model is an equation that predicts the minimum number of detectable analyte molecules based on input parameters that consist of the nanorod dimensions and optical system parameters. Building the model involved several steps; first, the spectral detection system and data analysis algorithms were analyzed to determine the measurement uncertainty in detecting LSPR peak wavelengths. Then, the average number of analyte

molecules that must bind to induce an LSPR shift equal to the measurement uncertainty for a given nanorod geometry was determined. This is the smallest number of bound molecules that can be reliably be detected by the proposed system and is defined as its MDL. It is important to note that we define the MDL by the amount of material bound to the surface of the nanoparticle, and not the concentration of the analyte in the surrounding media. This choice was made so that the focus of model is the interaction of the bound analyte with the plasmonic nanoparticles and the subsequent LSPR signal generated, and not the mass transport kinetics of the sensor system. Therefore, the optimal nanoparticle can be determined for a proposed analyte strictly by using the model to predict which geometry will offer the lowest MDL.

#### 4.1.1 Estimation of minimum detectable LSPR shift

The first step in the derivation of the model was estimation of the minimum LSPR shift that can be reliably measured for a particular detection system. We assumed that the total uncertainty is the sum of uncertainties induced by two factors as represented in Eq. 4.1: uncertainty introduced by the detection system  $U_{system}$ , and uncertainty introduced by the peak fitting to the gathered nanoparticle scattering spectrum,  $U_{fit}$ .

$$\text{Eq. 4.1} \quad U = \sqrt{U_{system}^2 + U_{fit}^2}$$

A thorough discussion of the  $U_{system}$  of the microspectroscopy system utilized in this work was briefly discussed in Section 3.3, and was reported based on analysis of silver nanospheres<sup>136</sup>. That study, which incorporates considerations of image focus, physical sample stability, and overall measurement repeatability of the measurements concluded that  $U_{system}$  was ~0.3 nm for the optical detection system described in that

work. The same experimental setup was used in this study; hence we assume that  $U_{\text{system}}$  is 0.3 nm.

Next, uncertainty due to the data analysis method must to be considered. The measurement noise was modeled as a Gaussian distribution. Although the physical model of noise in an optical measurement is a Poisson distribution due to shot noise, it can be accurately and conveniently modeled by a Gaussian distribution for a large number of photons because it is merely a counting problem. This yields the following relationship for  $U_{\text{fit}}$

$$\text{Eq. 4.2} \quad U_{\text{fit}} = \frac{1}{2} \frac{FWHM}{2.35 \cdot SNR}$$

where FWHM is the linewidth of the spectrum being fit and SNR is the signal-to-noise ratio of the data being fit.<sup>136</sup> The SNR depends on photoelectron signal magnitude  $M$ , the integration time  $t$ , and the spectrometer camera's dark current specification  $N_d$  and read noise  $N_r$  according to the following:

$$\text{Eq. 4.3} \quad SNR = \frac{M}{\sqrt{M + N_d t + N_r^2}}$$

For a shot noise-limited measurement ( $SNR = \sqrt{M}$ ), the shot noise dominates over the dark and read noise. The system used for this study has a dark current of less than 0.0025 electrons · pixel<sup>-1</sup> · second<sup>-1</sup> and read noise of less than 4 electrons RMS such that a shot noise-limited measurement (defined here as a measurement for which shot noise exceeds dark and read noise sources by an order of magnitude) will have an  $SNR > 13$  for a typical integration time of ten seconds. The role of the nanoparticle geometry in affecting measurement uncertainty becomes apparent as the signal level, that is the amount of light scattered, is proportional to the nanoparticle's scattering cross

section,  $C_{sca}$ . Thus in the shot noise-limited regime the following relationship holds for SNR:

$$\text{Eq. 4.4} \quad SNR_{SNL} = \sqrt{M} = \sqrt{A \cdot C_{sca}}$$

where  $A$  is a constant that accounts for the input photon flux, the integration time, and the quantum efficiency of the measurement system. The parameter  $A$  can be calculated for a microspectroscopy system by making a shot noise-limited measurement of the SNR of a nanoparticle with known  $C_{sca}$ .<sup>171</sup> We measured the scattering spectra of an 80 nm diameter gold sphere under typical operating parameters and observed a SNR of 100. Using the  $C_{sca}$  predicted by Mie theory of the sphere, a value of 0.385 is determined for  $A$  for the microspectroscopy system described in this work. With the value for  $A$  known, the SNR for an arbitrary nanoparticle of known  $C_{sca}$  may be calculated by rewriting Eq 4.3 as follows:

$$\text{Eq. 4.5} \quad SNR = \frac{A \cdot C_{sca}}{\sqrt{A \cdot C_{sca} + N_d t + N_r^2}}$$

Now, with Equations 4.2 and 4.5, it is possible to calculate total peak measurement uncertainty for an arbitrary particle based on the FWHM and  $C_{sca}$  of the particle, even if the measurement is not shot noise-limited.  $C_{sca}$  can be determined analytically as a function of nanorod geometry by applying the model developed by Kuwata *et al.*<sup>197</sup> Further details of the specific application of this model are reported below. Therefore,  $U$  can now be calculated entirely as a function of nanorod length and diameter. It is worth noting that the constant  $A$  is dependent upon the measurement system, but not upon the measured nanoparticle. Thus, it must only be empirically determined once for a specific experimental setup.

### 4.1.2 Quantification of Bound Molecules

The next step in the development of the model was to analytically translate this uncertainty limit from units of wavelength shift to number of bound molecules as a function of nanorod geometry. In order to formulate this relationship in a manner that is analytically simple, several approximations and assumptions were made. First, we assumed that the nanorods are cylindrical in shape with a length ( $l$ ) and diameter ( $d$ ). We recognize that the assumption that the nanorods are perfect cylinders is an approximation because transmission electron microscopy (TEM) images of chemically synthesized nanorods indicate that the nanorods are only approximately cylindrical, as they have “end-caps” with visible curvature on their ends. This approximation will introduce some error as it has been shown that end-cap geometry has an impact on the optical scattering spectra of nanorods.<sup>143, 198</sup> We also assumed that the LSPR peak shift,  $\Delta\lambda_{LSPR}$ , resulting from a bound analyte is proportional to the total LSPR shift that is expected if the entire surrounding medium increased to the RI of the analyte. The proportionality constant is the ratio of the analyte volume to the total sensing volume of the nanorod. This assumption yields the following relationship:

$$\text{Eq. 4.6} \quad \frac{\Delta\lambda_{LSPR}}{\Delta RI \cdot S(r)} = \frac{V_D}{V_S}$$

where  $V_S$  is the total sensing volume of the nanorod,  $V_D$  is the volume of the detected analyte,  $S(r)$  is the spatially-dependent RI sensitivity of the nanoparticle, and  $r$  is the distance of the bound molecule from the surface of the nanorod. Because the RI sensitivity decreases away from the nanoparticle surface, the sensing volume is defined as the fixed volume surrounding the nanorod that contains 95% of its sensitivity. Recognizing that the optical mass of the bound molecules is responsible for inducing the

observed LSPR shifts, the optical mass increase induced by bound analyte is defined as the product  $V_D \cdot \Delta RI$  where  $V_D$  is the volume of analyte bound to the nanorod and  $\Delta RI$  is the difference between the RI of the analyte and that of the surrounding medium. In the case where the approximate size of the analyte is known, the detection volume  $V_D$  can be replaced with the product  $N \cdot V_A$  where  $V_A$  is the volume of the analyte molecule and  $N$  is the number of bound molecules to the nanorod. Substituting this parameter in Eq. 6 and rearranging for  $\Delta\lambda_{LSPR}$  yields an expression relating the measured peak shift of the LSPR spectrum to the optical detection mass:

$$\text{Eq. 4.7} \quad \Delta\lambda_{LSPR} = \frac{S(r)}{V_S} \Delta RI \cdot N \cdot V_D$$

Solving Eq. 4.7 for  $N$  yields an expression that can be used to translate an observed LSPR peak shift into the number of bound molecules.

$$\text{Eq 4.8} \quad N = \frac{\Delta\lambda_{LSPR}}{\Delta RI \cdot S(r)} \cdot \frac{V_S}{V_D}$$

In order to determine the MDL of the system, we replace  $\Delta\lambda_{LSPR}$  in Eq. 4.8 with  $U$ , the uncertainty of the optical system in detecting wavelength shifts. Thus, the right hand side of Equation 4.8 becomes an expression of the bound optical mass that would induce the minimum detectable LSPR wavelength shift. In this case, solving for  $N$  yields an expression for  $L_M$ , the MDL of the system in terms of the minimum detectable number of bound biomolecules.

$$\text{Eq. 4.9} \quad L_M(l, d) = N = \frac{V_S}{V_A} \cdot \frac{U}{S(r) \cdot \Delta RI}$$

where  $L_M$  is a function of the length  $l$  and diameter  $d$  of the nanorod. From equation 9, we observe that the function  $L_M$  is determined by several parameters on the right-hand side. Careful examination of these parameters is required to fully understand

the dependence of each on the nanorod geometry and the effect each has on the overall MDL of the system. We note that  $L_m$  is dependent upon the detection system employed for measuring the LSPR shifts of single nanoparticles because of the dependence on the peak measurement uncertainty  $U$ .  $L_M$  is also a function of the spatially-dependent RI sensitivity  $S(r)$  of the nanoparticle, where  $r$  is the location of the bound molecule with respect to the surface of the nanorod.

### 4.1.3 Nanoparticle Geometry Dependence

#### 4.1.3.1 Scattering Cross-Section

In order to determine the function  $L_M$  analytically, we next sought to define the parameters  $U$  and  $S(r)$  based solely on the length and diameter of the nanorod, as follows: first, we utilized a model developed by Kuwata and co-workers to approximate the wavelength-dependent scattering cross-section ( $C_{sca}$ ) of gold nanorods as a function of nanorod geometry. This model provides the complete LSPR scattering spectrum of the nanorod with a simple analytical formula based on nanorod length and width. The model is based on fits to finite-difference time-domain with the depolarization factor calculated by electrostatic approximation.<sup>197</sup> We employed this formula to determine the location of the LSPR peak ( $\lambda^*$ ) and scattering cross-section  $C_{sca}$  at the peak wavelength for nanorods of arbitrary length and diameter. A second analytical model, based on Gans's extension of Mie theory<sup>46, 199, 200</sup> that simulates LSPR spectra as a function of the nanorod aspect ratio, was also used to simulate spectra as a means of validation. These two models provided consistent results within the geometric range of nanorods studied (length 50-100 nm and diameter 15-50 nm). These predictions were then further verified experimentally by comparison to scattering spectra of individual, chemically-synthesized nanorods as shown in Figure 12. The good agreement between

experimentally collected LSPR spectra and simulated spectra further indicate the utility of the analytical model.

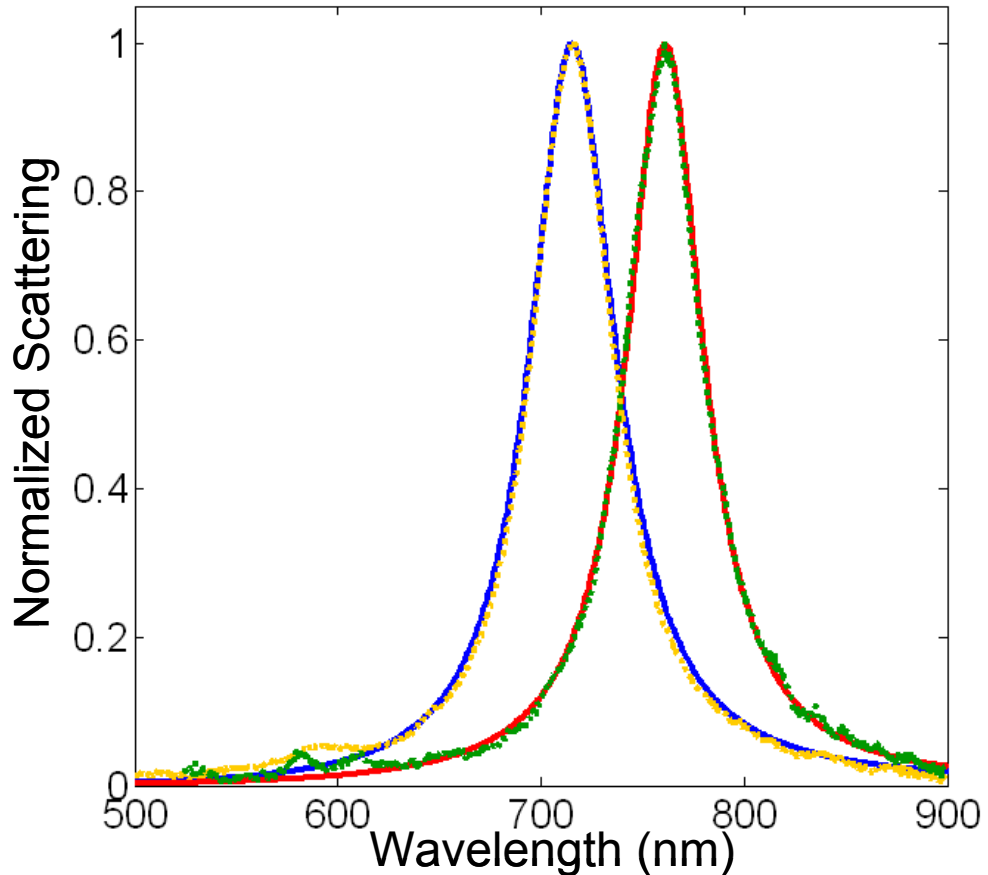


**Figure 12: Comparison of simulated versus experimental spectra. Scattering spectra collected from single nanorods from synthesized batches characterized by TEM to be  $63.3 \pm 8.2 \times 24.9 \pm 4.9$  nm ( $n=319$ , yellow dotted line) and  $74 \pm 9 \times 33 \pm 6$  nm ( $n > 100$  green dotted line). Simulated spectra for nanorods with dimensions  $64.5 \times 24.7$  nm (blue line) and  $75 \times 32$  nm (red line) via the Kuwata method are also shown.**

#### 4.1.3.2 Distance Dependent Sensitivity

It has been shown that LSPR shifts induced by local RI have a strong distance-dependence as a result of the exponential decrease in field enhancement further from the nanoparticle surface.<sup>119</sup> This distance-dependence of sensitivity has been experimentally measured for nanospheres<sup>71</sup> as well as anisotropic triangular

nanoparticles<sup>201</sup>. Additionally, it has been shown that the LSPR associated electric field is enhanced near the ends of nanorods.<sup>59, 82</sup> These observations suggest that the location at which a target analyte binds to the nanorod (i.e., along the sides or at the ends) will affect the magnitude of the induced LSPR shift. The detector-analyte system described in this work provides reasonable certainty in estimating the average binding distance, which is determined by the length of the receptor conjugated to the nanorod (biotin in the experimental case tested herein) and its binding site. Hence, we model sensitivity as being a function solely of the distance  $r$  from the surface of the nanorod  $S(r)$ . The effect of this assumption is that the model effectively outputs the LSPR response of the *average* bound analyte at a fixed distance  $r$  from the surface of the nanorod. This is a simplification of the physical phenomenon because of the known complexity of the electric field enhancement distribution. Nevertheless, this model is the closest representation to the actual detection experiments because the actual binding locations cannot be controlled, nor can the fraction of analytes that bind along the nanorod ends versus sides be accurately estimated.

With these assumptions clarified, we sought to generate an analytical function that describes  $S(r)$  purely as a function of nanorod geometry. This was done by first collecting sensitivity distance-dependence data for many nanorods of various geometry. This data was collected by using a procedure previously reported to probe the sensing volume of gold nanospheres by adsorbing sequential layers of oppositely-charged polyelectrolytes to the nanoparticle surface.<sup>109</sup> From the data, we build an analytical approximation that provides the distance-dependent RI sensitivity  $S(r)$  for a nanorod of arbitrary dimensions. This is accomplished by fitting experimental  $S(r)$  data, identifying

the geometric dependence of the fits, and generating expressions to reproduce a theoretical  $S(r)$  for a nanorod of arbitrary geometry.

First, a fit is applied to the experimentally determined response curves,  $\lambda^*$  versus adsorbed polyelectrolyte thickness. To determine the form that this equation should take, we examine the underlying physical process. Since light energy is driving the detection system, it is reasonable to assume that the proper weighting factor for the distance-dependent response is proportional to the light intensity at that point<sup>79</sup>. The light intensity is the electric field strength squared, and for planar SPR, it has been shown that the field decays with distance  $r$  from the surface. Thus, the distance-dependent response can be modeled to follow the form  $\exp(-2 \cdot r / l_d)$  where  $l_d$  is some characteristic decay length<sup>81</sup>. The overall sensor response can then be calculated as the depth integral of the local RI weighted by the electric field intensity. For a system composed of a single adlayer in the surrounding medium, the response can be written as<sup>79</sup>:

$$\text{Eq. 4.10} \quad R(r) = S_0 \cdot (n_a - n_s) [1 - \exp(-2r / l_d)]$$

where  $n_a$  and  $n_s$  are the refractive indices of adlayer and solvent respectively,  $S_0$  is the bulk RI sensitivity, and  $l_d$  is the decay length characteristic of a particular SPR geometry. This equation has also been shown to be reliably extended to modeling LSPR response of individual nanoparticles<sup>74, 119</sup>.

In order to provide an analytic form of equation S1 in terms of nanoparticle geometry, the overall bulk RI sensitivity  $S_0$  must first be determined in regard to

nanoparticle length and diameter. The value of  $S_0$  is in units of nm/RIU and it is a measure of how much  $\lambda^*$  will shift (in nm) upon a given RI increase of the entire medium surrounding the nanorod.  $S_0$  can be approximated by taking advantage of the linear correlation in visible wavelength range between  $S_0$  and  $\lambda^*$  for nanoparticles of similar composition described by Miller et al<sup>142</sup>. For single-component nanoparticles, the bulk sensitivity  $S_0$  is given by:

$$\text{Eq. 4.11} \quad S_0 = \frac{2}{n} \left( \lambda_0 + \frac{\epsilon_0}{m} \right)$$

where  $n$  is the RI of the ambient environment,  $\lambda_0$  is the LSPR peak in vacuum, and  $m$  is the slope of is a linear fit to the real part of the metal's dielectric function ( $\epsilon' \approx m\lambda_0 + \epsilon_0$ ). This function describes nanoparticle sensitivity behavior for particles that are in a surrounding medium of homogenous RI. Recently Miller et al. have shown that the correlation can be extended to accommodate particles in intimate contact with a substrate by introducing a scaling factor by replacing  $n$  with  $\beta n$  giving:

$$\text{Eq. 4.12} \quad S_0 = \frac{2}{\beta n} \left( \lambda_0 + \frac{\epsilon_0}{m} \right)$$

where  $\beta$  depends on the nanoparticle geometry and substrate RI. For nanorods on glass, they have shown that  $\beta n = 1.75$  provides excellent agreement with experimental results. Using  $\lambda_0$  determined from the simulated scattering spectra, the bulk sensitivity  $S_0$  can approximated for a nanorod of

arbitrary dimensions. For example, utilizing Equation S3 with  $\beta n = 1.75$  predicts a bulk RI sensitivity of 268.7 nm/RIU for 74.1 x 33.2 nm (length x diameter) nanorods on glass with  $\lambda^*$  of 720 nm, which is in good agreement with the experimentally determined bulk RI sensitivity of 261.7 nm/RIU<sup>75</sup>.

Now  $S_0$  has been determined as a function of nanorod geometry and  $n_a$  and  $n_s$  are known, only the decay length  $l_d$  is yet to be determined to produce an analytical expression for  $R(r)$ . Mathematically, this decay length determines the rate at which the response curve approaches its asymptote. Physically, this represents the confinement of sensitivity to the nanorod surface. So for lower values of  $l_d$ , the response curve approaches its asymptote more quickly, simulating nanorods where the sensing volume is confined closer to the surface. Because  $l_d$  is a function describing electric field enhancement, we assume its dependence on nanorod geometry is of the same form as the shape parameter,  $e$ , employed in the Gans<sup>202</sup> extension of Mie theory<sup>203</sup> describing the scattering cross section of elliptical gold nanoparticles.

$$\text{Eq. 4.13} \quad l_d(l, d) \equiv l_d(e) = l_d \left( \sqrt{1 - \left( \frac{d}{l} \right)^2} \right)$$

To determine the correlation between  $l_d$  and  $e$ , Eq. 4.12 was fit to the experimental response curves of twelve experiments, two each for six different nanorod geometries. Plotting  $l_d$  versus  $e$  for the range of nanorods used, a linear

correlation is observed. A linear fit to this plot yields equation 4.14 with an R-squared value of 0.941. Residuals from the linear fitting exhibit no clear shape.

$$\text{Eq. 4.14} \quad l_d(e) = 228 \cdot e^{-176}$$

This expression provides an approximation for describing  $l_d$  in units of nm based on the geometry of the nanorod. Now that the response curve  $R$  can be determined for arbitrary nanorod geometries, the distance-dependent sensitivity  $S(r)$  and the total sensing volume  $V_S$  are defined. As discussed above, the response is proportional to the square of the decaying electric field strength. Thus, it will be of the form:

$$\text{Eq. 4.15} \quad S(r) \equiv A \cdot \exp(-2r/l_d)$$

The normalization constant  $A$  is chosen to normalize  $S(r)$  such that its average value over the detection range is equal to the bulk sensitivity,  $S_0$ . This normalization is solved when  $A = 3S_0$ , which is then substituted into equation S6 yielding the following.

$$\text{Eq. 4.16} \quad S(r) \equiv 3S_0 \cdot \exp(-2r/l_d)$$

The sensing volume  $V_S$  is defined as the volume of a cylinder with hemispherical endcaps circumscribed by extending a distance  $r_s$  from the nanorod, where  $r_s$  is the distance at which  $S(r)$  drops to 5% of its maximum value. This distance occurs at 1.5 decay lengths. For nanorods on a substrate,

the volume occupied by substrate within the circumscribed cylinder is subtracted to yield the effective  $V_S$ .

From this fit, the sensing volume of the nanorod  $V_s$ , and the decay length of electric field enhancement  $l_d$  were also determined as a function of nanorod geometry.  $V_s$  is defined as the fixed distance from the nanorod surface containing 95% of  $S(r)$  and the decay length is the distance from the nanorod surface at which the electric field enhancement is reduced by a factor of  $e$ . Figure 13 shows the excellent agreement obtained between the model and experimental data.

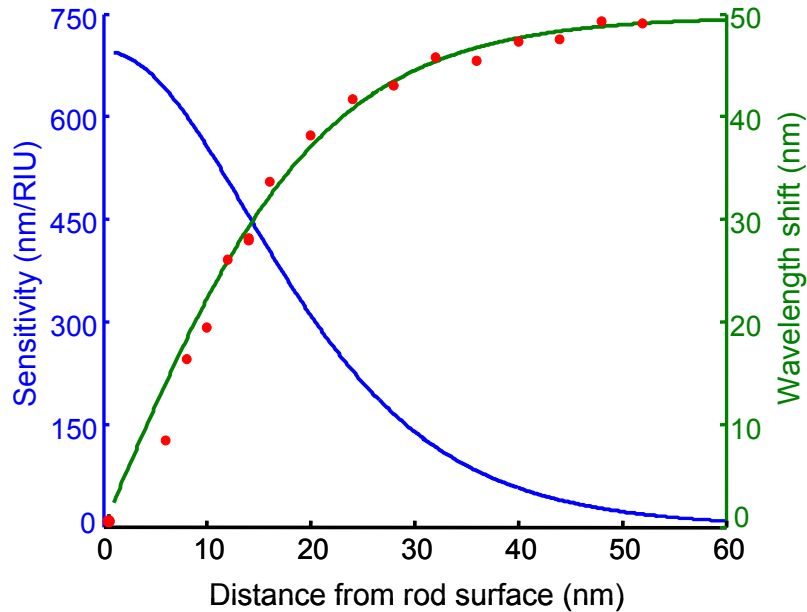


**Figure 13: Right axis - experimental wavelength shift of a nanorod ( $63.3 \pm 8.2$  nm x  $24.9 \pm 4.9$  nm) as a function of deposited polyelectrolyte thickness (red dots) and shifts predicted by equation 7 (green line). Left axis - corresponding calculated distance dependence of the nanorod LSPR sensitivity (blue line).**

## 4.2 Complete Analytical Model

Now that  $V_s$  can be described completely in terms of nanorod geometry, it is possible to write every parameter on the right hand side of equation 4.9 as an analytical function of the length and diameter of the nanorod such that the MDL,  $L_M$  of an arbitrary nanorod can be analytically estimated from the length and diameter of the nanorod.

$$L_M = \frac{V_S}{V_A \cdot \Delta RI} \cdot \frac{\sqrt{U_{SYSTEM}^2 + U_{FIT}^2}}{\exp\left(\frac{-2r}{l_d}\right) \cdot (3S_0)}$$

Eq. 4.17

where  $V_S$  is the sensing volume,  $V_A$  is the analyte volume,  $\Delta RI$  is the RI difference between the analyte and the surrounding medium,  $U_{SYSTEM}$  is the peak measurement uncertainty resulting from uncertainty in the physical detection of the LSPR peak,  $U_{FIT}$  is peak determination uncertainty due to data fitting,  $S_0$  is the bulk RI sensitivity,  $r$  is the distance from the nanorod surface that the analyte binds, and  $l_d$  is the decay length of the resonant electric field.

Equation 4.17 is especially useful because it allows an analysis of the overall performance of a single nanoparticle based on a variety of parameters, only one of which is the nanoparticle bulk RI sensitivity  $S_0$ . We emphasize this point because much work in the field has been devoted to synthesizing nanoparticles with different geometries and compositions in order to optimize the RI sensitivity of the nanoparticle.<sup>56,</sup>

<sup>74, 204</sup> Clearly, the nanoparticle bulk sensitivity is an important contributor to the overall MDL; however it is not necessarily the most important. In fact, Miller *et al* have shown that the bulk RI sensitivities of nanoparticles can be predicted from the wavelength of the LSPR peak, independent of nanoparticle shape.<sup>142, 205</sup> The parameter  $U$  is also clearly important in determining MDL, but has largely been ignored on discussions of MDL.<sup>136</sup>

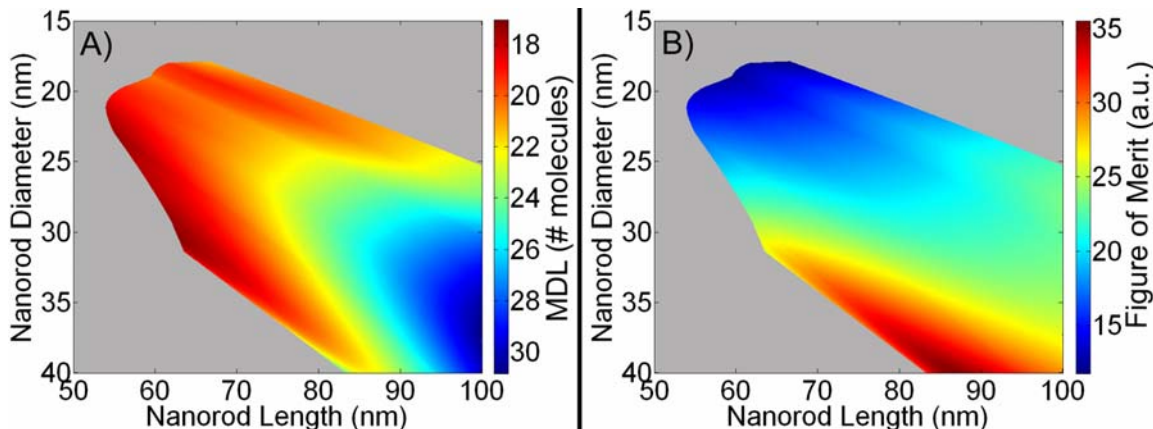
Obviously the sensitivity of the detection system depends not only on the signal generated by the nanoparticles but also how precisely it can be measured. This parameter is primarily dependent on optical detection system parameters and data analysis techniques. However,  $U$  also depends on nanoparticle geometry because spectra for nanoparticles with higher  $C_{SCA}$  can be measured more accurately due to their increased scattering signal as seen in Equation 4.17. Other parameters, such as the effective sensing volume of the nanoparticles (i.e. the electric field enhancement localization) can vary a great deal across geometries and have a large impact on the sensing characteristics of a nanoparticle. Nanoparticles with more confined electric field enhancements maintain smaller sensing volumes, resulting in larger shifts upon analyte binding within the sensing volume. However, nanoparticles with smaller detection volumes have a smaller dynamic range because they saturate upon the binding of fewer analytes. The proposed model offers a means to collectively analyze the effects of these parameters on overall sensor performance to deduce the optimal nanoparticle geometry for a LSPR sensor that is designed for a specific application.

Figure 14A shows the theoretical MDL for streptavidin binding to biotin decorated gold nanorods as predicted by equation 10 for single nanorods of arbitrary dimensions when measured in the described microspectroscopy system for which  $U$  has been previously characterized. We chose this analyte-receptor pair because their interaction is one of the best characterized and most commonly used model receptor-analyte systems. The simulation was restricted to nanoparticles that have LSPR peak wavelengths in the range 300-900 nm because that is the range observable in the microspectroscopy system. We also applied a minimum  $SNR$  threshold of 30 to exclude particles with small  $C_{sca}$  that cannot produce enough scattered light to be visualized in

the darkfield microscopy setup. For this reason, no data are shown for nanorods with LSPR peaks outside of this range or with SNR below the cutoff of 30. We assumed the streptavidin molecules have a volume<sup>206</sup> of 114 nm<sup>3</sup> and RI of 1.57.<sup>79</sup> From Figure 14A, we can see that nanorods with lengths between 55 and 65 nm in length and between 25 and 33 nm in diameter offer the lowest MDL of ~18 streptavidin molecules. It is important to note that the nanorod MDLs predicted by equation 4.17 are a monotonic function of several detection system and analyte parameters. Although the absolute value of the MDL will vary across detection systems and receptor-analyte pairs, the relative performance of a nanorod with a specified geometry will not vary, so that once the optimal rod geometry has been identified for a target analyte, it will always offer the lowest MDL across detection systems and receptor-ligand configurations.

In addition to the absolute MDL, the dynamic range (DR) is an important quantitative performance indicator of a biomolecular sensor. For the purposes of this model, the DR is defined as the theoretical maximum number of analyte molecules that are detectable by a single nanorod. This definition was chosen because it is consistent with the model output, which is quantified as the number of bound molecules. The DR was determined by calculating the total surface area available for binding, and dividing it by the footprint of a bound analyte molecule. This value was then scaled by a factor of 0.9 which assumes a hexagonal packing density of hard spheres which would yield the highest possible coverage that could be achieved in practice. By this definition, a larger nanorod will obviously exhibit a higher DR because of its larger surface area. However, larger nanorods also tend to have higher MDLs because of the increased sensing volume. To balance these considerations, we calculate a composite figure-of-merit (FOM) for nanorods that includes both the DR and MDL of these nanorod plasmonic

sensors operating in the single nanorod mode. The composite FOM is calculated simply as the ratio of the DR versus its MDL. Figure 14B shows the composite FOM for nanorods of arbitrary dimensions. Figure 14B shows that rods with length 85 nm and diameter 40 nm offer the highest composite FOM with the potential to bind ~35 times as many molecules as is required to generate its lowest detectable signal. So although nanorods of those dimensions may exhibit a MDL of ~22, their higher dynamic range indicates they may be more useful as a streptavidin sensor over a wider range of analyte concentrations.



**Figure 14: A) Calculated molecular limits of detection for gold nanorods of arbitrary dimension based on equation 4.17. B) Composite figures of merit (FOM) for nanorods of arbitrary dimensions. The composite FOM is calculated as the maximum number of bound molecules divided by the minimum number of detectable molecules. The surrounding gray regions in both are indicative of nanorod geometries that were not considered in this model because they either had resonances outside the visible spectrum or had scattering cross-sections that are insufficient to collect spectra with SNR greater than 30.**

### ***4.3 Experimental Application of Model***

To experimentally test the results provided by the model, gold nanorods were synthesized with dimensions that were as close to the geometry predicted by Equation 4.17 (and visually represented by Figure 14A) to have the lowest streptavidin MDL. To experimentally test the predictions of the model, streptavidin binding experiments were

performed using biotin-functionalized gold nanorods that were shown by TEM to have a length of  $63.3 \pm 8.2$  nm and a diameter of  $24.9 \pm 4.9$  nm (N=319) (Figure 15A). Equation 4.17 calculates that these rods have a mean MDL of 20 molecules and mean FOM of 22.

A dose-response curve was determined by incubating identical samples of biotin-functionalized gold nanorods that were chemisorbed on glass slides in streptavidin solutions that spanned a range of protein concentration. Sensor preparation and streptavidin incubation were performed identically as described in section 4.3. Figure 15B shows the steady-state LSPR shift of single nanorods as a function of streptavidin concentration. A sigmoidal fit was applied to these data, and the concentration at which the fit crosses the LSPR peak measurement uncertainty of 0.3 nm was defined as the experimental detection limit. For the experiments shown in Figure 15B, the detection limit is 160 pM.

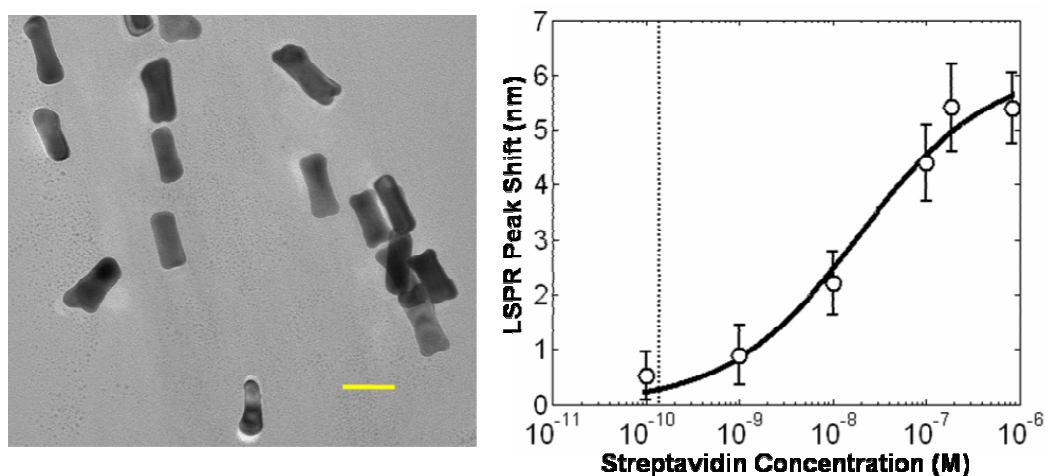


**Figure 15: A) TEM of rods used in this study. Nanorod length is measured to be  $63.3 \pm 8.2$  nm and diameter  $24.9 \pm 4.9$  nm (N=319). Scale bar corresponds to 50nm. B) LSPR peak shift of individual, biotin-activated gold nanorods versus concentration of streptavidin. Open circles are the mean LSPR shift of 15**

**nanorods per measurement at each concentration and the error bars indicate 95% confidence interval. The solid line is a sigmoidal fit to the data. The dotted line indicates where the fit line crosses 0.3 nm shift, the measurement detection uncertainty as calculated above. This occurs at a concentration of 160 pM.**

#### **4.3.1 Quantitative Analysis of Molecular Detection Limit**

To investigate the relationship between the experimental detection limit measured by analyte concentration and the MDL predicted by Equation 4.17, we specifically looked at the detection of 100 pM streptavidin. Figure 16 shows fits to scattering spectra collected from a single nanorod incubated in 100 pM streptavidin. The blue line is the nanorod LSPR scattered spectrum in water, the red line is the spectrum after the binding of biotin, and the black line is the spectrum after incubation in 100 pM streptavidin. The ~3nm shift between the blue and green lines observed upon biotin functionalization is consistent with the adsorption of a thin dielectric layer. The length of the biotin-amine is estimated to be 2.39 nm (Chem3d, CambridgeSoft) and the SAM to which the biotin is conjugated has a thickness of 2.78 nm and RI of 1.464.<sup>207</sup> Using Equation 4.6 to simulate the LSPR response of the addition of dielectric layers yields an expected LSPR peak shift of 3.59 nm. This value is in good agreement with the experimental mean LSPR shift of  $3.23 \pm 1.2$  nm observed upon the incubation of biotin for all nanorods used in the streptavidin detection experiments.

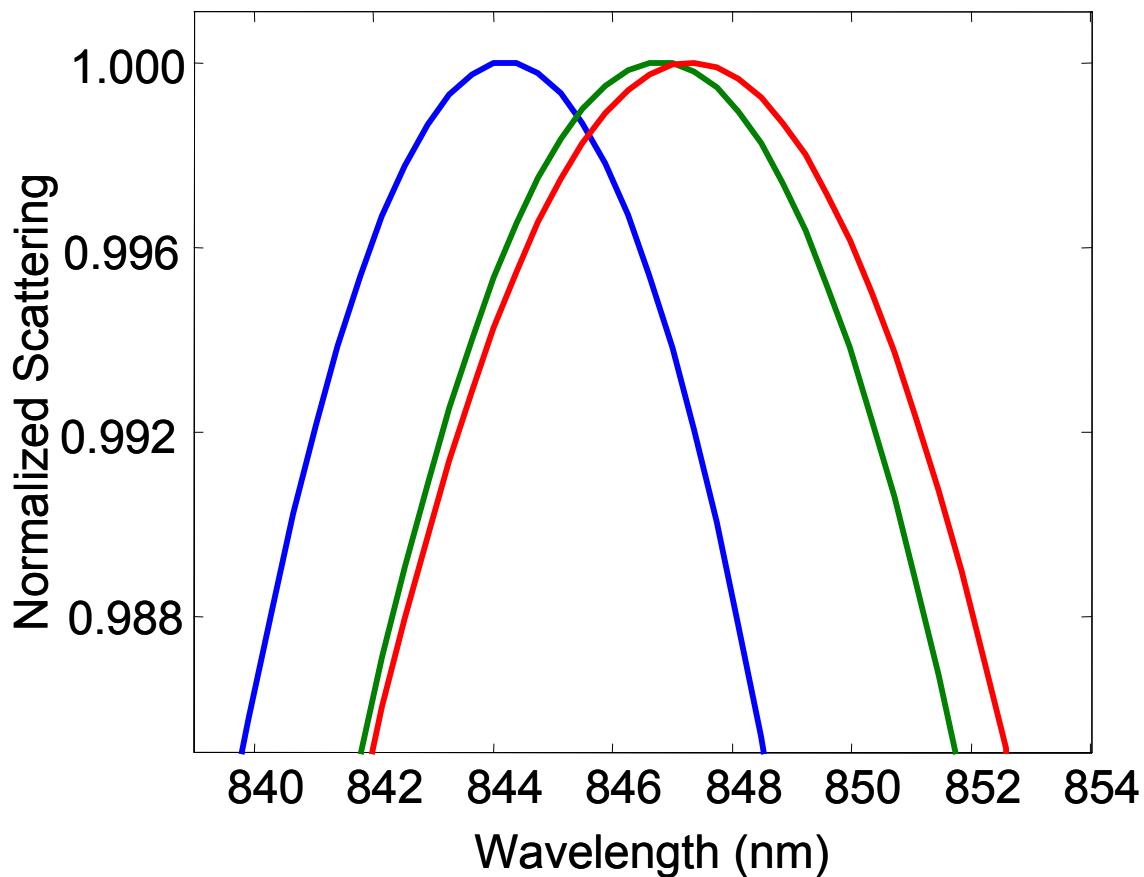


**Figure 16: Fits to scattering spectra of a single nanorod in water (blue), after biotin conjugation (green), and subsequently in 100pM streptavidin (red). The 0.52 nm shift corresponds to approximately 27 streptavidin molecules by Eq 4.8.**

A 0.52 nm shift was observed upon incubation of the bioin-functionalized gold nanorods in 100 pM streptavidin, which translates to ~27 streptavidin molecules bound by a single nanorod, by use of Eq. 4.8. Lower streptavidin concentrations were tested in order to establish the detection limit in terms of concentration, but did not yield results that were statistically significant from negative control experiments<sup>75</sup>, so the lowest streptavidin concentration that was experimentally detected is 100 pM. This experimentally detected minimum of approximately 27 molecules is reasonably close to the theoretical MDL of 20 streptavidin molecules per nanorod predicted by the model for the nanorods used. Thus, by utilizing the proposed model - equation 4.17, specifically -

to select the optimal nanorod geometry for streptavidin detection, we are thus able to observe binding in the pico-molar range. To our knowledge, this is the lowest reported concentration of biomolecule detected with a single particle LSPR sensor.

#### **4.3.2 Quantitative Analysis of Molecular Dynamic Range**

As a further check of the relevance of the MDLs predicted by our model, we observe that the mean LSPR shift at saturation is 4.4 nm (Figure 14B). Using Equation 8, we calculate that this shift arises from the binding of approximately 280 streptavidin molecules to the nanorod surface. For the nanorods used in these experiments, approximately 8000 nm<sup>2</sup> of biotin-activated surface is available for the binding of streptavidin molecules. Each streptavidin molecule is a tetramer of four identical biotin binding subunits, and the entire tetramer is roughly ellipsoidal with axes 5.4 nm x 5.8 nm x 4.8 nm.<sup>208, 209</sup> Thus, the footprint that a streptavidin molecule would occupy on the binding surface is approximately 25 nm<sup>2</sup>. In this orientation, a maximum of only 320 molecules would be expected to fit on the nanorod surface. Approximating the streptavidin molecules as hard spheres, the model of random sequential adsorption<sup>210</sup> predicts a packing ratio of 0.54 which would translate to only 170 bound molecules. Whereas the highly ordered method of hexagonal packing predicts a packing ratio 0.9, allowing for up to 290 streptavidin molecules. Therefore, the 280 molecules bound at saturation as determined by Equation 8 is reasonable and suggests a more ordered arrangement of bound streptavidin molecules.

Additionally, we compare the mass of streptavidin presumed bound at saturation by equation 8 with that of streptavidin adlayers that were experimentally measured. Densities of 240 ng/cm<sup>2</sup> and 231 ng/cm<sup>2</sup> have been experimentally determined for streptavidin layers formed over biotin layers on flat substrates.<sup>211, 212</sup> These binding

densities yield an estimated ~220 bound streptavidin molecules to the available nanorod binding area of 8000 nm<sup>2</sup>. Again, these estimates are slightly lower than the 280 molecules estimated from equation 8 to be responsible for the 5.29 nm shift observed at saturation but are close enough to justify the validity of our calculations.

#### **4.4 Prospects for Single Molecule Detection**

We also used this analytical model to systematically explore the parameters in Eq. 4.17 within physically realistic limits to determine which parameters can be modified in order to develop a LSPR sensor with a single molecule MDL.

The product  $V_A \cdot \Delta RI$  is a parameter of the analyte and of the surrounding medium. For proteins with a RI commonly near 1.57, detection in water (RI = 1.33) yields a typical  $\Delta RI$  of 0.24. By drying the samples and taking measurements in air (RI = 1.00)  $\Delta RI$  can be increased to 0.57. Thus, a factor of 2.4 improvement in MDL is possible through this method. We note that this approach would preclude real-time detection, and require further processing steps of the sample, which detracts from the strength of label-free detection. However, this drying methodology has been successfully utilized by Van Duyne and coworkers.<sup>73</sup>

The total sensing volume  $V_S$  of the nanoparticle is determined by the nanoparticle shape and decay length  $l_d$ . Smaller  $V_S$  and  $l_d$  are indicative of nanostructures with small, intense electric field enhancements. In general, the sensing volume will vary proportionally with the cube of the decay length simply because it is a three dimensional volume subtended by the decay length. In the case of rods, smaller rods have shorter decay lengths. So ideally, one would want to use the smallest nanorods possible. However, smaller rods also exhibit smaller scattering cross-sections  $C_{SCA}$  which means they scatter less light under darkfield illumination. For rods in

particular,  $C_{SCA}$  varies approximately as the square of the rod length and proportionately to rod diameter.<sup>197</sup> So if the length and diameter of a nanorod were both reduced by a factor of 2,  $C_{SCA}$  would be reduced by about a factor of 8. On the other hand, to maintain an adequate SNR of the collected spectra, the intensity of the illumination source must be increased. An upper limit to this intensity exists because at some point the nanorods will melt due to photothermal effects.<sup>213, 214</sup> The use of a broadband illumination source, such as a supercontinuum fiber laser, would allow the complete scattering spectrum to be collected and would provide a light output that is 6-10-fold more intense than the tungsten filament used in the experimental setup used here. Hence, Eq. 4.17 predicts that a physically realistic increase in illumination intensity by a factor of 10 could enable the visualization of smaller nanorods, effectively reducing the size of the rod by about 1.5, thereby reducing the sensing volume and decay length, which would ultimately reduce the MDL by a factor of 7.

The decay length of the electric field enhancement  $l_d$  is determined by the geometry of the nanoparticles. Eq. 4.17 assumes a uniform decay length for nanorods. The actual electric field enhancement has a more complicated geometry and in particular has been shown to exhibit larger enhancements near the ends of the rod.<sup>43, 46, 82</sup> Thus, analyte molecules that bind near the end of the nanorod will cause a greater LSPR shift than those binding on the lateral portion. For this reason, Eq. 4.17 is applicable to a MDL that stems from the LSPR response of individual biomolecules that are spatially-averaged around the nanorod surface. It is reasonable to make this approximation for the experiments described here, because the streptavidin molecules are adsorbed a fixed distance  $r$  from the nanorod surface, but no further spatial localization is possible. It has been shown through finite element modeling that the ends

of nanorods exhibit much higher field enhancement than the spatial average.<sup>215</sup> Thus, if analyte binding can be limited to only within these regions, it is reasonable to assume a concurrent sensitivity increase greater than a factor of ten due to the reduction of sensing volume. A recent paper offers describes selective functionalization of nanoparticle vertices by a thiol-replacement strategy that reportedly provides a route to site-specific functionalization of nanorods<sup>216</sup>. This could lead to significantly higher signals per bound analyte molecule as theoretical models indicate that the electric field enhancement is as much higher at the nanorod ends than along the sides<sup>43, 46, 82</sup>. Initial reports cite a reduction in concentration detection limits by a factor of 500<sup>216</sup>. As a rough estimate as applied to the MDL model, we assume molecular binding can be restricted to only the end-caps of the nanorod while maintaining the same net LSPR shift upon saturation. This results in the reduction of the available binding area, and thus number of molecules bound at saturation by a factor of 4. Further, if we restrict binding to only the end-cap edges, this factor is increased to 9.

The binding distance  $r$  is the physical distance that the analyte binds from the surface of the nanoparticle. It is determined by the length of the receptor which is approximated to be 2.4 nm for the experiments presented herein. EDC-NHS coupling is used to conjugate amine-terminated biotin to the carboxyl-terminated monolayer applied to the gold surface. We employ this binding moiety because it offers easy translation to other amine-terminated receptors, such as antibodies or aptamers.<sup>72</sup> It would be possible to employ a physically shorter receptor that would cause the target analyte to bind closer to the surface of the nanoparticle where the field enhancement, and thus RI sensitivity, is greater. For example, using thiol-terminated biotin has been successfully employed as a receptor for streptavidin detection with single nanoparticles.<sup>116</sup> This

would reduce  $r$  by as much as a factor of 2 which in return reduces the overall MDL by a factor of  $\exp(l_d^{-1})$ . For the case of nanorods with decay length  $l_d$  generally on the order of 10-20 nm, this results in a factor of 1.1 improvement (i.e. 10% decrease in MDL). In most practical situations, however, the size of the receptor-analyte pair is likely to be significantly larger than the model biotin-streptavidin pair used here (e.g., antibody-protein), so that some of the gains realized from the optimization of the parameters discussed here are likely to be offset by the size of the receptor analyte pair. Nevertheless, these results suggest that minimizing the size of the receptor while retaining high binding affinity and specificity for its analyte is an important factor in extracting the minimum MDL of which LSPR sensors are capable. In this regard, the use of smaller receptors such as aptamers<sup>112, 217</sup> or smaller, engineered antibody fragments such as single chain antibodies are preferable to intact antibodies, which to date are the most commonly used class of receptors in biosensors<sup>1, 19, 36, 149</sup>.

The bulk RI sensitivity of a nanostructure  $S_0$  is dependent on its size, shape and material composition. However, Miller and Lazarides have observed that  $S_0$  is correlated with the LSPR peak wavelength, regardless of nanoparticle shape.<sup>142, 205</sup> Thus, for a nanostructure of known material composition, its bulk RI sensitivity can be predicted simply by characterizing its LSPR peak. Because longer wavelength resonances exhibit higher bulk RI sensitivities, the highest sensitivities will be from particles with LSPR peaks in the red end of the spectrum. Assuming the detection is to remain in the visible light spectrum, LSPR peaks at wavelengths up to 800nm could be measured. Thus, bulk RI sensitivities as high as 600 nm/RIU could be expected. This is more than a two-fold improvement over the 260 nm/RIU sensitivity of nanorods used in this study. However it is worth noting that for the case of nanorods, longer resonances correspond

to larger rods with larger sensing volumes and longer decay lengths. Eq. 4.17 was used to balance the contributions for these effects to optimize sensor performance using the nanorod geometry. Thus, for this factor of 2 increase to be realistic, an alternative nanoparticle geometry would be sought that could indeed have a resonance far into the red without such large geometries. Additional sensitivity could be achieved by structuring the sensor to operate in near-IR wavelengths where the bulk RI sensitivities are higher, although the optics and instrumentation could be potentially more challenging. Also, silver nanoparticles exhibit sensitivities typically 1.5-fold higher than gold particles at similar resonant wavelengths. However, as mentioned above the high reactivity of silver makes it less suitable as a sensor for use in biologically relevant media.

The peak measurement uncertainties  $U_{FIT}$  and  $U_{SYSTEM}$  represent the most direct way at improving sensor detection limits. Obviously, the smaller the wavelength shifts that can be reliably detected, the greater the accuracy and lower the overall MDL will be. For the system used in these experiments,  $U_{FIT}$  was found to be approximately 0.02 nm while  $U_{SYSTEM}$  was found to be 0.3 nm. Thus, the contribution to MDL is dominated by  $U_{SYSTEM}$ , whereas  $U_{FIT}$  acts more as an absolute limit for noise levels as discussed above. We performed an in-depth analysis of the contributing factors to  $U_{SYSTEM}$ , and found that a large portion of the uncertainty is the result of physical system stability.<sup>136</sup> In particular, it was found that stability in microscope focus and sample stage drift account for the largest contributions in uncertainty. It is proposed that by using active feedback hardware to control microscope focus and XY-sample location,  $U_{SYSTEM}$  can be reduced to the order of 0.005 nm.<sup>136</sup> Thus, the total uncertainty would then be dominated by  $U_{FIT}$  resulting in a 15-fold decrease in MDL.

These possible enhancement factors are displayed in Table 4.1. From here we see that the estimated possible enhancement factors could potentially provide an 7200-fold improvement over the 18 molecule detection limit described herein. Thus, we show that the ultimate limit of label-free detection of single molecule binding events is theoretically possible within the framework of equation 4.17.

**Table 1. Theoretical improvement factors that can reduce the molecular detection limit of a label-free, single particle LSPR sensor based on the modulation of parameters from equation 4.17.**

Technique Summary	Variable from Eq. 4.17 involved	Potential Enhancement Factor
Drying	$\Delta RI$	2.4
Brighter Illumination Source	$C_{sca}$ , $V_S$ and $I_d$	7
Shorter Binding Moiety	$r$	1.1
LSPR peaks in IR	$S_0$	2
Silver Nanoparticles	$S_0$	1.5
High Spectral Resolution Detection System	$U_{SYSTEM}$	15
Isolation to rod edges	$V_s$	9
	<i>TOTAL</i>	~7200

#### **4.5 Significance of Results**

In conclusion, we have presented a simple mathematical model that analytically relates physical detection parameters of a single nanoparticle LSPR sensor to the minimum number of detectable analyte molecules. The utility of this model is two-fold. It can be used to select the optimum nanoparticle geometry for a desired detection system completely analytically, forgoing otherwise necessary comprehensive, experimental characterization. The minimum number of detectable molecules can be estimated as

well as the number of molecules detected at saturation which provides insight into the dynamic range of the system. Equation 4.17 was used to predict the optimal nanorod geometry to for the detection of streptavidin molecules. A factor of 10 reduction in the minimum detectable concentration was established over previous work using a non-optimized nanorod detection system. Additionally, the first dose-response curve of biomolecular detection using individual nanoparticles as transducers was reported through this work.

The second application of the model is that a framework is provided through which the effects of potential system improvements can be assessed. Analysis of the theoretical limits of the dependent variables of equation 4.17 indicates that a 7200-fold reduction of the MDL for the detection system described herein is possible. Clearly, not all of these potential avenues for MDL reduction can be realized concurrently. However, because our current MDL is 18 streptavidin molecules, we propose it is theoretically possible to design a system capable of detecting single molecule binding events by careful optimization of system parameters, as described herein.

## 5 Plasmonic Imaging

The work described herein proposes to take advantage of the label-free sensing properties of individual noble metal nanoparticles, while avoiding some of the disadvantages typically inherent in such technically demanding detection systems. We explore methods by which a sensor can operate by analyzing a micrograph containing many distinct nanoparticles simultaneously. This approach offers not only the same advantages of single nanoparticle analysis, but also adds several potential advantages. The first and most obvious advantage is the increase in signal accuracy attained simply from the statistical gains of several hundred simultaneous measurements versus a single measurement. Furthermore, the capability of spatially resolved measurement of the plasmonic response of noble metal nanoparticles also opens the door to label-free, on-chip multiplexed sensing. To achieve this, many spatial addresses of plasmonically active structures that are functionalized with different “receptors” need to be queried in parallel. This has been the goal of other more conventional label-free optical microarray techniques such as surface plasmon resonance imaging (SPRI), which is being developed as a label-free alternative to multiplexed fluorescence assays<sup>148</sup>.

Most existing approaches towards spatially-resolved optical detection rely on intensity measurements at a fixed illumination wavelength and incident angle<sup>148, 152</sup>. However, intensity-based techniques do not offer the same sensitivity as measurements that are resolved by wavelength or by the illumination angle as described in section 1.4. In one example, a slit-imaging spectrometer, similar to that which is used for the microspectroscopy system described in this work, was used to query a one dimensional line of plasmonic nanostructures. By shifting one spatial dimension to a spectral dimension, sensitivity was improved by an order of magnitude<sup>168</sup>. Recent reports also

describe results using an optical grating as the underlying sensing substrate to convert on spatial dimension to an angular dimension<sup>169</sup>.

Our approach described herein, is distinct from these approaches as we focus on collecting LSPR data that is resolved in three dimensions: two spatial and one spectral. We chose this approach because LSPR-based detection methods preclude the need for moving parts to measure angular resolution, so that in principle, a simple and robust detection system can be built using existing imaging technology to carry out highly multiplexed measurements of spatially addressable arrays of receptors bound to spatially distinct regions of a nanoparticle decorated surface. Multispectral and hyperspectral imaging are the typical means of collecting optical data that is resolved in both space and wavelength. Multispectral imaging is typically considered when image data is available from several distinct wavelength spans, whereas hyperspectral techniques attempt to completely fill the measured wavelength space. Practical application of both types of imaging presents several obstacles.

Hyperspectral image data is typically collected one of two ways: either by making sequential measurements at varying wavelengths, or by directing the collected light through an optically dispersive element such as a grating. The first method is typical of modern hyperspectral imaging techniques and requires many measurements to be taken. Any optical measurement is limited in its acquisition to only two dimensions, because current CCDs and photodiode arrays have only been built with two dimensions of detectors. A full hyperspectral image is a three dimensional data cube with the three dimensions corresponding to x position, y position and wavelength. In order to generate 3-D data from a 2-D source, a third dimension is needed. Time is the other dimension that is used to generate 3-D hyperspectral images. A tunable light source<sup>165, 167</sup> or

filter<sup>218, 219</sup> can be used to collect images in time, each at a different wavelength to build the full 3-D cube. Alternatively, optically dispersive elements such as gratings, prisms, or mirrors<sup>78, 220</sup> can be used to transfer a spatial dimension to a wavelength dimension, and the sample can be physically rastered in time or with filters<sup>127, 170</sup> to collect the remaining position dimension. The minimum reported time scale at which a full hyperspectral data cube can be acquired is on the order of 5 minutes, which is far too slow to capture kinetic binding data for most biomolecular binding events that are relevant for biosensors.

However, for measurement of LSPR scattering it is often not necessary to collect the entire wavelength-dependent spectrum of nanoparticle samples to determine LSPR shifts because a great deal of *a priori* knowledge is available about the optical response of the nanoparticles. It has long been known that a single plasmon resonant peak exhibits a Lorentzian shape, as originally shown by Mie<sup>203</sup>. It has also been shown that the magnitude of LSPR peak shifts exhibited upon a local refractive index increase can also be reliably predicted based on the initial peak wavelength<sup>142</sup>. Since so much is known about the properties of the LSPR of nanoparticles, it is therefore not necessary to collect the entire wavelength-dependent spectrum. In the simplest case, it is possible to observe LSPR shifts simply by monitoring the extinction at a single wavelength. This technique has been shown to be effective in measuring biological interactions between biotin and streptavidin by using a spectrophotometer to monitor the extinction of a gold nanosphere-covered substrate at a wavelength near the inflection point of the LSPR peak<sup>70</sup>. As the LSPR shifts to the red, extinction at that wavelength increases, which can be easily calibrated to correlated biomolecular binding. This study demonstrated how detection of wavelength-resolved LSPR shifts can be compressed in complexity

from a 1-D spectrum to a 0-D point intensity measurement. In this work, we seek a compressive analogue that will allow reduction of 3-D hyperspectral image data down to two dimensions using *a priori* knowledge of the LSPR behavior of noble metal nanoparticles, so that the data can be quickly and simply collected using a conventional CCD.

Two techniques were explored that enable spatial and spectral resolution of LSPR resonances detected in a single snapshot. The first method that was investigated was a multispectral imaging approach using a CCD with patterned, filtered pixels. An off-the-shelf RGB camera was used to quantify LSPR shifts of gold nanospheres, and a theoretical model was developed to estimate the utility of other pixel filter transmittances on the overall sensitivity of the sensor. The second means investigated was a novel spectral imaging technique that takes advantage of the low background signal of darkfield images. In this method, entire data images are incident to a diffraction grating, and both the zero-order and first-order diffraction modes are collected simultaneously by a CCD. The zero-order image provides information regarding physical alignment of the image, thereby allowing the proper deconstruction of spectral information from the first-order diffracted mode. Further details and the results of each approach are described in the remainder of this chapter.

## **5.1 Multispectral Imaging**

Recent reports describe how data collected with a simple RGB digital CCD camera can be used recover complex spectra by employing computational statistical training and regression methods<sup>221</sup>. Preliminary experiments were conducted to determine if a similar approach can be used to determine if RGB images can indeed be used to determine the spectral changes from LSPR response of individual nanoparticles.

In these experiments, the changes in the LSPR response of individual nanoparticles were caused by modulating the surrounding refractive index (RI) of the medium. The LSPR shift in response to change of the RI of the medium is observed as changes in the color (RGB) distribution within each diffraction-limited-spot. Initial approaches used partial least-squares (PLS) regression to correlate each channel's intensity to of the RI of the surrounding medium. However, further investigation revealed that a linear approach was not appropriate to modeling LSPR color shifts, so a modified look-up table calibration was developed as described below in section 5.1.2.3.

### **5.1.1 Preliminary Work: RGB Camera**

Before any experiments were conducted, a theoretical analysis was performed of the expected shifts that would be observed with an RGB camera. Figure 17A shows the response curves for the blue, green and red channels of the RGB digital CCD camera that we planned to use for these experiments. The red overlay is the scattering spectrum of a single 60 nm diameter gold nanosphere. As its scattering peak shifts to the red due to an increase in the bulk RI, corresponding increases in the value of the red channel and decreasing values in the green and blue channel are expected. PLS regression was applied to these modeled intensity changes. Figure 17B shows the expected shift in the PLS value as a function of the bulk RI.

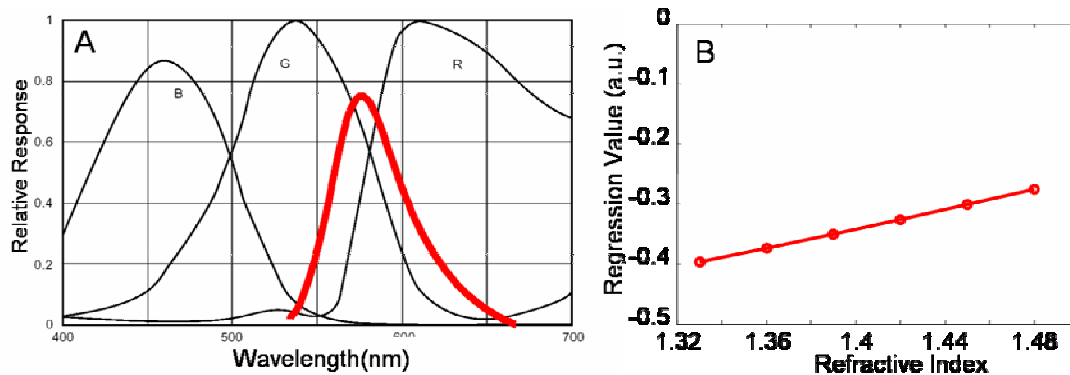


**Figure 17: A) Response curves for the red (R), green (G), and blue (B) channel of the CCD camera used to measure LSPR shifts of 60 nm gold nanospheres. Red overlay is the scattering spectrum of a single nanosphere. B) Theoretically expected trend in the regression value calculated from the RGB intensities as a function of the bulk refractive index.**

Initial experimental tests were performed using a conventional RGB camera. Darkfield images were collected of a field of 60 nm diameter gold nanospheres. Substrates were prepared as described in section 3.3.2. Images were collected of gold nanospheres under 0, 40 and 80 percent (v/v) glycerol in water with refractive indices of 1.333, 1.392, and 1.450 respectively. Figure 18A shows micrograph of the nanospheres in water. Nanoparticle spots were identified by automated image thresholding. Each nanoparticle spot was background corrected by subtracting the mean intensities of the surrounding dark regions. Three intensity values (RGB) were then identified for each particle as the mean of that intensity within the particle spot. The linear regression coefficients, determined from the response curves and used to generate figure 17A, were then applied to these intensities. Figure 18B shows a plot of the resulting regression values as a function of RI. The red boxes indicate the mean regression value of the nanoparticle spots in the image, and the black error bars indicate the standard deviation ( $n \sim 250$  particles). The green line is the predicted trend shown in figure 17A which is included for reference.

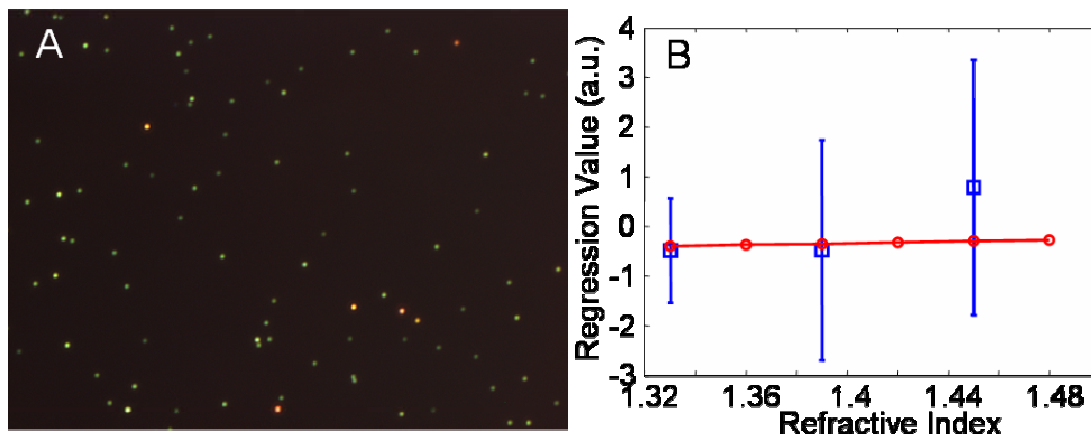


**Figure 18: A) RGB image of 60nm gold nanospheres in water. B) Blue squares denote the mean and standard deviations (blue error bars) of regression values of 60nm nanospheres ( $n \sim 250$ ) under 0, 40 and 80 percent glycerol in water. Red line shows theoretically expected trend of this plot.**

From Figure 18B, it is obvious that the experimental variations wash out any trend that might be observed. In general, a plot that could actually be used to calibrate a sensor would have either a steeper slope, or smaller standard deviations or both. From this experiment, several factors were identified which are thought to contribute to this high variability. First, gold nanospheres exhibit a low RI sensitivity relative to other nanoparticle shapes such as rods. Also, as seen in Figure 17A, the nanosphere scattering spectra have very little overlap with the blue channel of the CCD camera. Thus, this channel contributes very little to discerning the small LSPR shifts of nanosphere spectra. From Figure 18A, it is also obvious that not every spot in the image corresponds to single nanosphere. Dimers and further aggregates appear as yellow or orange spots. Additionally, the inherent variation in nanosphere geometry will lead to a distribution in spectra that was not effectively modeled in the predicted response.

## 5.1.2 Multispectral Imaging Simulation

In order to determine if a multispectral imaging approach is a suitable means for assessing LSPR shifts of nanoparticle images, a theoretical model was developed that seeks to expand upon the above experiments and query a wider range of potential experimental configurations. The primary limitation of the unsuccessful experiments described above was that they were limited by the pre-fabricated spectral channel responses of the RGB camera. In the following model, filter response curves are variable and an optimized configuration is sought. We also switched to gold nanorods (RI of 1.42!! ADDIN EN.CITE <EndNote><Cite><Author>Schief</Author><Year>1999</Year><RecNum>705</RecNum></record><rec-number>705</rec-number>rectra) were included by modeling each nanorod's dimensions as a random member of the normal distribution of particle geometries. Then the geometry-dependent scattering spectra was then calculated for each rod based on its dimensions so that the model more accurately represents experimental conditions. The goal of the model was to simulate images of nanorod samples as a function of RI as observed in darkfield and to determine how accurately LSPR shifts can be measured by these images. This was performed in three steps. First, a full spectrally-resolved data cube was generated of a field of nanorods. Then, simulated detection images were generated as if collected by a CCD with variable three-channel response curves. Finally, these images were analyzed to determine their ability to predict RI shifts.

### 5.1.2.1 Data Cube Generation

The model generates a full data cube consisting of simulated darkfield micrographs of spots with full spectral resolution. The form of the output data cube is a stack of images, each at a specified wavelength, that together contain all spectral

information of the nanorod LSPR. The model generates a data cube based on the following three parameters: number of nanoparticle spots, geometric distribution of the nanorods, and the spectral intensity of the incident light. The number of spots simply determines how many spots will be randomly distributed over the field of view. The nanoparticle geometric distribution determines the observed variation in LSPR peak location and intensity. The spectral intensity of the incident light modulates the final observed spectral distribution of the LSPR spots. To simulate an experiment where nanorods are used to report the bulk RI change, several data cubes were generated – each at a specified RI of the surrounding medium. Figure 19 graphically illustrates the output of the model.

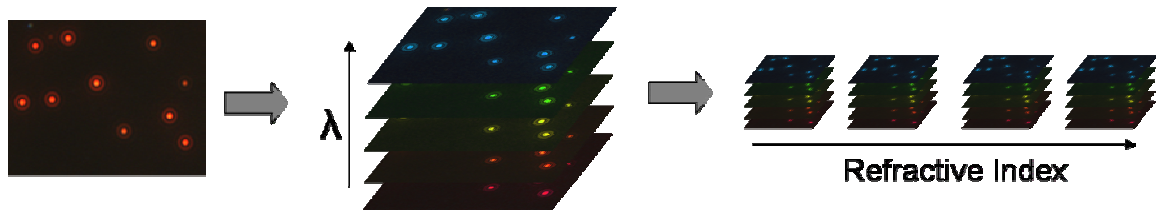


**Figure 19: Model output. First, simulated micrographs are generated at a specified wavelength. These images are stacked, providing a full, spectrally-resolved data cube. Finally, cubes are generated at several surrounding refractive indices.**

The shape of each spot was simulated by calculating the point-spread-function of a diffraction-limited spot. The intensity of each spot depends on the LSPR spectrum of the particle and the intensity of the illumination source at the specified wavelength. Scattering spectra were calculated for each particle, based in its width and length which were assigned corresponding to the expected distribution of nanorod dimensions according to an analytical model<sup>197</sup>. Each simulated image was generated initially at a spatial resolution much higher than the resolution of the detector, as determined by its

pixel dimensions. This was done to account for the fact that each spot is not perfectly centered on a detector pixel.

To simulate LSPR shifts as a function of local RI, several data cubes were generated – each at a specified bulk RI from 1.25 up 1.50. This range of RI was simulated because it fully spans the experimentally relevant range of RI in biosensing. Water, the surrounding environment in the experiments, has an RI of  $n=1.33$  and adsorbed protein adlayers have a maximal RI of  $1.42^{222}$ . The LSPR spectrum of each spot was individually shifted in response to the increased RI according to their respective bulk RI sensitivities. These sensitivities were calculated for each spot based on the physical dimensions of the nanorod it represents using the correlation between LSPR peak position and sensitivity<sup>205</sup>.

#### **5.1.2.2 Detection Simulation**

The model was next used to simulate the LSPR shifts induced by changes in the RI of the surrounding medium. In these simulations, the space of possible filter response curves was explored to determine which arrangement provided the most sensitive detection of RI shifts. This was done by simulating the response of each detector arrangement of the data cubes generated. Then, a calibration algorithm was applied to the response data that relates the color data to the RI. The performance of each sensor arrangement was evaluated by the slope of the regression line and the standard deviations at each RI, which define the sensor sensitivity and uncertainty respectively.

The first step in determining how a specific sensor arrangement would perform was to simulate the darkfield images it generates of nanorod-covered substrates. This was accomplished by translating the high resolution data cubes generated in phase I of

the model development into two-dimensional images based on the physical dimensions and optical response of the detector pixels. The intensity of each pixel in the flattened image was calculated by binning all the pixels in the high-resolution data cube and integrating along the wavelength dimension with the response curve of the applied filter. Then, the data was scaled according to the bit depth and range of the detector. The result of this flattening step was a single, flat image at the resolution of the detector. Figure 20 graphically illustrates how this was done to generate a single, flat image. For a multi-filter detector (such as the common three channel RGB filter set), one image was generated for each filter.

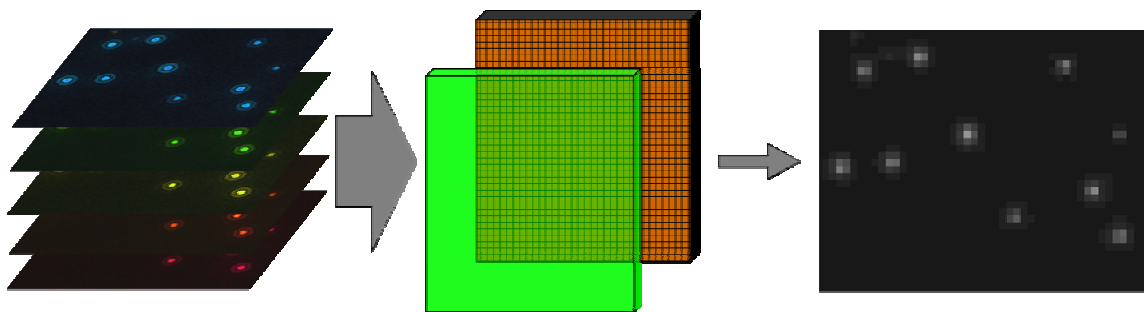


**Figure 20: Simulation of detector response. The full, high resolution data cube is modulated by the filter response and integrated on the detector. The pixels are binned according to their physical dimensions on the detector yielding an intensity image that simulates how the nanorod sample would appear if collected with the specified detector system.**

### 5.1.2.3 Calibration

For each detector system analyzed, a set of images simulating LSPR shifts was assembled by flattening images from each RI data cube. This set of simulated images corresponds directly to the expected experimental data set of observing LSPR shifts by imaging with a CCD detector. As such, the data analysis applied to the simulated data was identical to that which was applied to experimental images. The data analysis

proceeded by first finding the spots on the field of view by thresholding the image. The spots found by thresholding were then filtered to remove particles expected to be outliers. The only excluded spots that exist in the simulated images are spots that are too close together in the image for individual analysis. Once each spot was identified, its intensity data was collected for each filter.

Our initial calibration approach used PLS to generate a calibration curve. This regression minimizes the distance of each point in a least-squares manner and describes the optimal line by which future image data can be interpolated to determine its corresponding RI. The problem with applying this algorithm to LSPR shifts, is that the shifts are not monotonic with respect to starting color. For example, assume that a nanoparticle that has a peak resonance at 650 nm, and exhibits a resonance shift of 20 nm based upon an increase in local refractive index. A nanoparticle with a peak resonance at 630 nm and which experiences the same RI increase will experience a different wavelength shift. It may only shift to 645 nm. Further, if the 630 nm starting particle experiences a refractive index increase sufficient to shift its resonance to 650 nm, its spectrum will still be different than a particle that started at 650nm. There are two reasons for this. First, LSPR shifts induced by an increase in the local RI also slightly increases the scattering cross section of the nanostructure. As a result, the scattering intensity is increased, which in turn will alter the signals measured by the filter response curves. The second reason is that nanoparticle bulk RI sensitivity is correlated with the starting resonance wavelength. Thus, the particle that resonates in water at 650 nm will shift further upon a RI increase than one resonating at 630 nm in water. This effect is illustrated in figure 21. Each series of correspondingly colored dots indicates the color of a gold nanorod as measured in the Cielab XYZ colorspace, a standardized

3-channel colorspace used to measure color. In general, the spots move to greater Y values and lower Z values as the RI increases. However, the trend is not linear and it is not monotonic. The trajectory that a spot takes through the colorspace as RI increases depends on where it started, not just where it is.

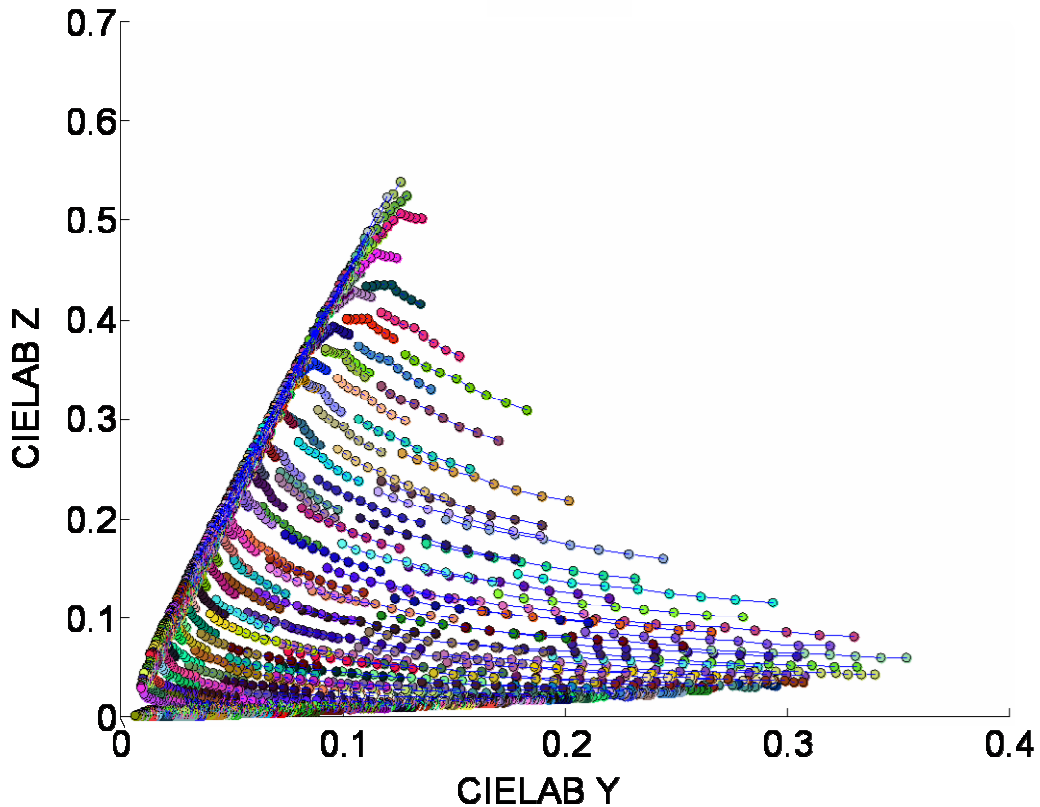


**Figure 21: Shifts in CIELAB XYZ colorspace of nanorods with different resonance wavelengths. Each group of colored spots denotes the color change that a nanoparticle will experience as local refractive index is increased. In general, increased RI moves toward the right.**

To bypass the non-linearity of these shifts, a modified lookup table was instead used to calibrate image data. A calibration data cube was generated by simulating an image of nanorods spaced along a grid. The nanorod length was increased for spots down the columns while the nanorod diameter is increased along the rows, such that the

entire span of geometries expected in the image is covered. Figure 22A shows a false-color image of a calibration data cube.

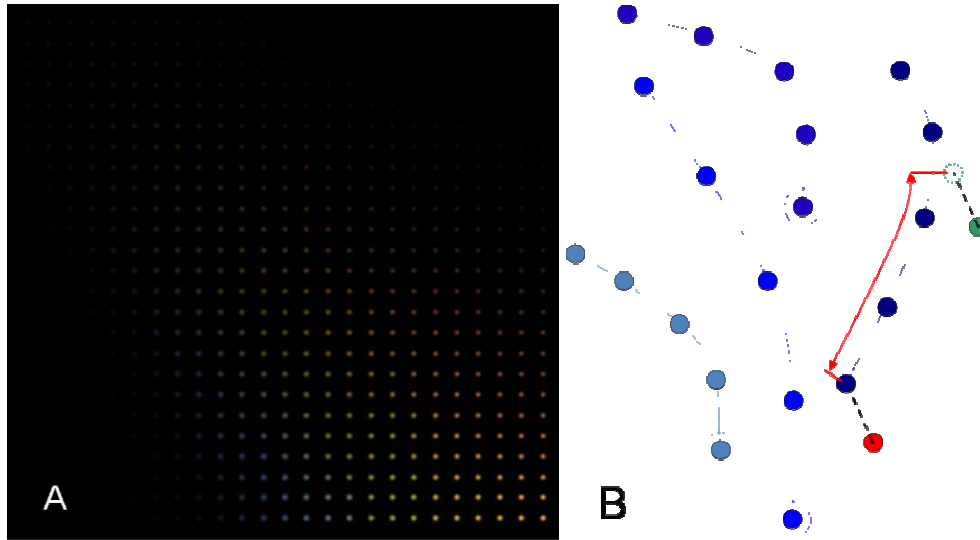


**Figure 22: A) False color image of a calibration image. B) Schematic illustration of how calibration images are applied to determine refractive index shifts of test image data.**

A calibration cube is created for each refractive index. Simulated images of the calibration data cube were then used as calibration standards for a given filter response curve configuration. Figure 22B illustrates a simplified two-dimensional example of how the calibration cube was used to determine the refractive index shift between two image spots. Each line with blue dots corresponds to the path in colorspace that a single nanorod takes as RI is increased, with distance between each spot corresponding to the same RI increment. In this example, increased RI is toward the top of the figure. The calibration lookup table is then used to determine the RI difference between two images of the same nanoparticle. The red dot corresponds to the image data at a known RI and the green dot corresponds to the image data at an unknown higher RI. First, a nearest-neighbor method is used to determine which blue path should be used for RI comparison. The blue dots with rings correspond to calibration images at the same RI

as the initial measurement (red dot). Once the nearest neighbor is found, the test data is shifted to overlap the calibration trajectory. Computationally, this is performed by a simple vector subtraction. Now the total RI increment between the two data points is represented as the distance between the two along the calibration trajectory. This is represented in the figure as the length of the red line, and it is computationally determined as the vector projection of the test spot between the two nearest calibration spots. Finally, the RI increment of the two images is calculated as the mean increment determined for all nanoparticle spots. In the case of high coverage samples, the RI increment was calculated on a pixel-to-pixel basis, as opposed to isolated spots corresponding to light scattered by individual rods.

#### **5.1.2.4 Simulation Results**

The simulated geometric distribution of nanorods was selected to correspond with measurements made by TEM. The nanorods used in this study were from the same optimized batch used in section 5.3. They were measured by TEM to have a length of  $63.3 \pm 8.2$  nm and a width of  $24.9 \pm 4.9$  nm (N=319). Figure 23A graphically illustrates this distribution as a probability density function. The plot in Figure 23B shows the spectra of 40 randomly generated nanorods from the geometric distribution (shown as blue dots on the probability density curve).

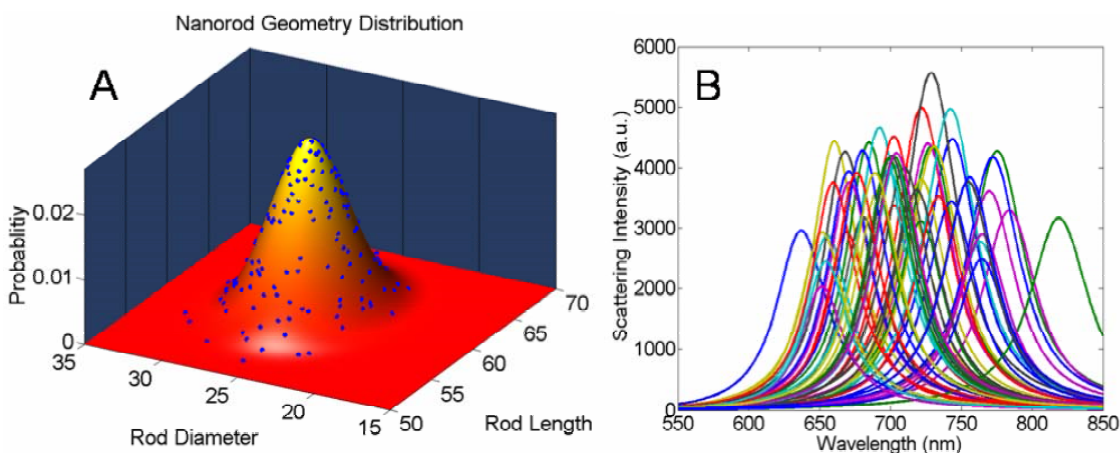


**Figure 23: A) Probability density function of gold nanorods used in this study. B) Scattering spectra of 40 nanorods randomly selected from this geometry distribution.**

The light source spectral density used in the simulations was collected experimentally from a conventional microscope-mounted halogen lamp. As a first test of the model, images were generated simulating the filter responses of the Coolsnap Color RGB camera mounted on the microspectroscopy system. The images were scaled and digitized to eight bits per channel to match the camera bit depth. Figure 24A shows an experimentally collected image of the gold rods and figure 24B shows an image generated using the simulation. The primary difference in the two images is the lack of background illumination in the simulated image which can be observed in the experimental image due to imperfect darkfield illumination. This added background has the spectral density of the illumination light source and thus appears as a yellowish haze in both the background and the particle spots themselves. At this point, no background noise was added to the simulation since we first desire to assess a best-case scenario. Figures 24C shows an experimentally collected image of a nanorod sample incubated overnight, resulting in a much higher density. An experimental sample was measured by AFM and determined to have a surface density coverage of approximately  $1.0 \times 10^8$

nanorods per  $\text{cm}^2$ . This corresponding coverage was simulated and is shown in figure 24D.

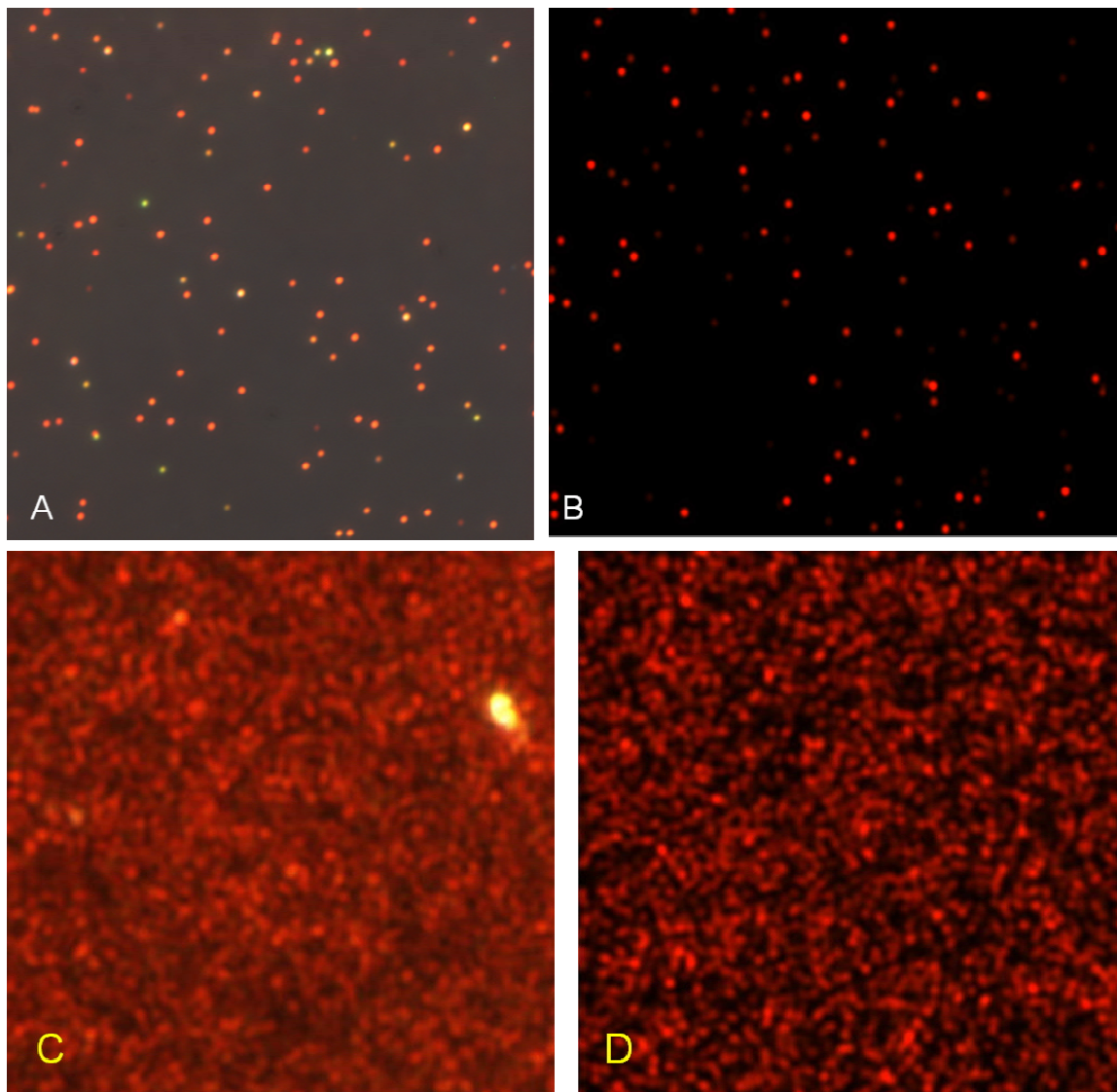


**Figure 24: Experimentally collected image (A) and simulated image (B) of gold nanorods at low coverage. High coverage experimental image (C) and simulation (D).**

Three filter sets were examined through the applied model. First, to provide a baseline comparison standard to commercially available detectors, the response curves of a Nikon D700 color camera was modeled. The CIELAB XYZ colorspace, as specified

by the International Commission on Illumination as a device-independent color comparison standard was also modeled as a filter set. Finally, filter response curves were modeled that have been shown to offer theoretically optimum color discernment - referred to herein as the KLM filter set<sup>223, 224</sup>. Both the KLM and XYZ three channel filtering schemes were rescaled in the wavelength dimension so that the spectral discrimination was strongest in the spectral range where the nanorods resonate. The filtering functions were linearly scaled to range from 600 to 900 nm.

Figure 25A displays the results of the lookup table-based regression applied to simulated images modeled with detection by the scaled KLM detector scheme which was the most successful filter scheme determined by this study. Nine simulated images were generated at each RI in increments of .005 with low nanorod coverage similar to that displayed in Figure 25B. The refractive index of each image was then calculated by the lookup regression scheme. The error bars show the standard deviation within the images at each RI. As an example, the red dots show specifically the RI prediction results of the nine images generated at RI = 1.35. The dotted black line shows the ideal one-to-one case. The mean standard deviation from these plots is 0.004 RIU which corresponds to a theoretically minimal measurement uncertainty of 1.0 nm. Figure 25B shows the corresponding data from a high coverage simulation similar to that shown in Figure 24D. The corresponding measurement uncertainty of the higher coverage samples is 0.0021 RIU which corresponds to 0.55 nm. The commercially available D700 modeled suffered from the same limitations encountered with the Coolsnap Color when trying to measure shifts from gold spheres. Because the filter was designed to separate spectral responses within the entire visible spectrum, small variations within the small window where nanorods resonate could not be observed. In fact, linear fits could not

even be reliably applied to the modeled results as the variation was so high, just as observed in figure 18B.

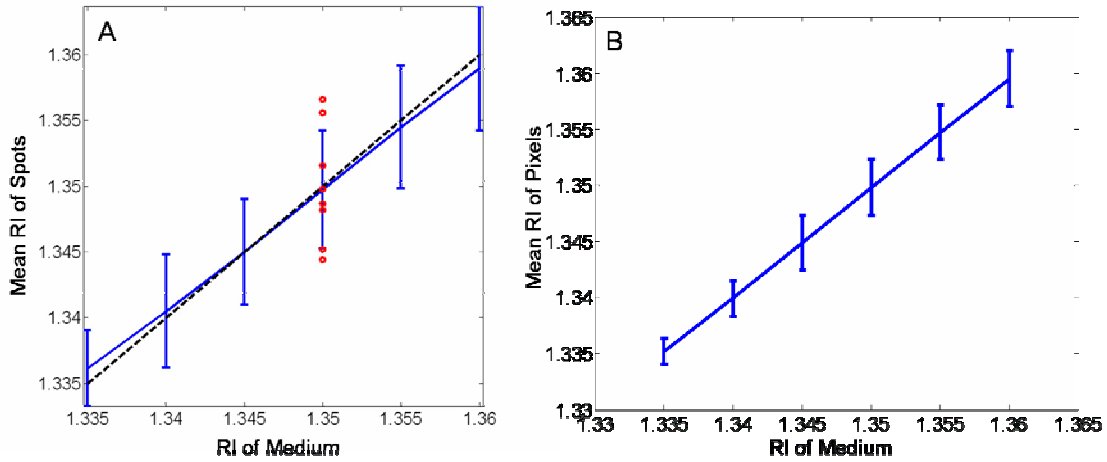


**Figure 25: A) Regression results of the KLM filter scheme applied to simulated low coverage images of nanorods. B) Regression results from high coverage simulations**

### 5.1.2.5 Discussion

The motivation for this work was to explore possible detection methods that could potentially offer gains over existing methods in one or more areas. The first metric of interest is overall LSPR shift detection sensitivity. The goal was to determine how the a detection imaging system that collects many less-precise measurements compares with one that makes a single, high-precision measurement. The results above indicate that even under ideal conditions, the multispectral imaging approach does not lead to any gains in reducing the overall measurement uncertainty over the single particle microspectroscopy described in previous chapters. Most importantly, it must also be noted that the simulations described included no sources of noise. Each resonant peak was modeled as a clean Lorentzian peak with no background or counting noise. A more detailed simulation would include signal-dependent shot noise and background

illumination that is a function of the illumination spectral density. Obviously, simulated and experimental measurements that include such noise will be much less accurate than the ideal case described above. Since the ideal, noiseless case exhibits LSPR peak measurement uncertainties already three-fold higher than the single-particle microspectroscopy system, further refinement of the model was not pursued.

The low resolution of the spectral measurements of each nanoparticle spot also requires that every spot be measured only as a contribution to the total RI, and not as isolated RI measurements. The result is a loss of the spatial registration of spectral information that was also one of the driving motivations of the pursuit of this technique. Finally, we note that the most effective detection scheme employed a filter system that is not commercially available – another initial motivator for the exploration of the multispectral imaging technique. For these reasons, we determined that the multispectral approach as described above does not offer any significant advantages over existing means of querying LSPR resonance shifts and therefore shift our attention to alternative means.

## ***5.2 Dual-Order Spectral Imaging***

Recent publications describe novel methods looking towards rapid, parallelizable or spatially addressed techniques that do not rely on collecting entire three dimensional data cubes. These techniques rely on compressing one or more of the data dimensions in such a way that a two dimensional data set can be collected and used to infer information about the entire cube. Coded aperture snapshot spectral imaging (CASSI) is a compressive detection scheme in which data images are passed through a dispersive element and imaged onto a coded aperture while dispersed in wavelength. The spectral content of the image can then be reconstructed using pre-collected calibration data<sup>225</sup>. In this way, spatially addressed spectral information can be obtained by compressing the

data in the wavelength dimension for detection with a two-dimensional detector. This technique has been proven successful in classifying fluorescent beads<sup>226</sup> from a snapshot image collected under broadband illumination.

In this section, we describe work developing a novel LSPR imaging technique that employs an approach that is similar in spirit to the spectral compressive sensing used in CASSI. However, in this approach instead of compressing the wavelength dimension, we compress along one spatial dimension. This is fundamentally different than simply reducing the content of the data down to two dimensions by cropping the field of view as is done with other LSPRI techniques discussed above. In the approach described below, wavelength-resolved spectra are collected simultaneously from a field of scattered particles.

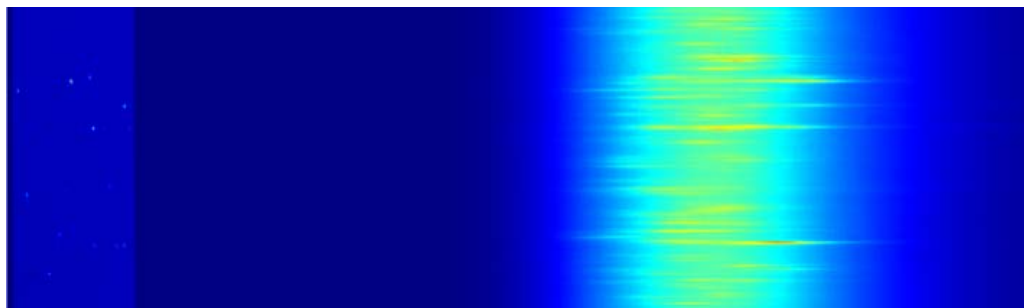
### **5.2.1 DOSI Technique Description**

We term the technique dual-order spectral imaging (DOSI) due to the operating principle responsible for its utility. The setup is similar to a conventional slit imaging spectrometer with two fundamental differences. First, a grating is selected that has a relatively coarse line pitch. This reduces the dispersion of the grating, effectively reducing the spatial extent of the dispersed light when it reaches the CCD detector. Typically, optimal resolution is achieved by using a grating with the finest line pitch possible such that the wavelength range of interest of the first diffracted mode of the image covers the full extent of the detector pixels<sup>136</sup>. By using a coarser grating, we sacrifice the slightly higher spectral resolution to allow concurrent collection of both the zero-order image, and the first order diffracted mode of the image both on the same CCD. The collection of both diffraction orders allows for the spatial registration of the image spectral content and is necessary for accurate reconstruction of LSPR peak

shifts. The grating used in the DOSI setup had 150 lines/mm as compared to the 600 lines/mm grating used in the previous studies.

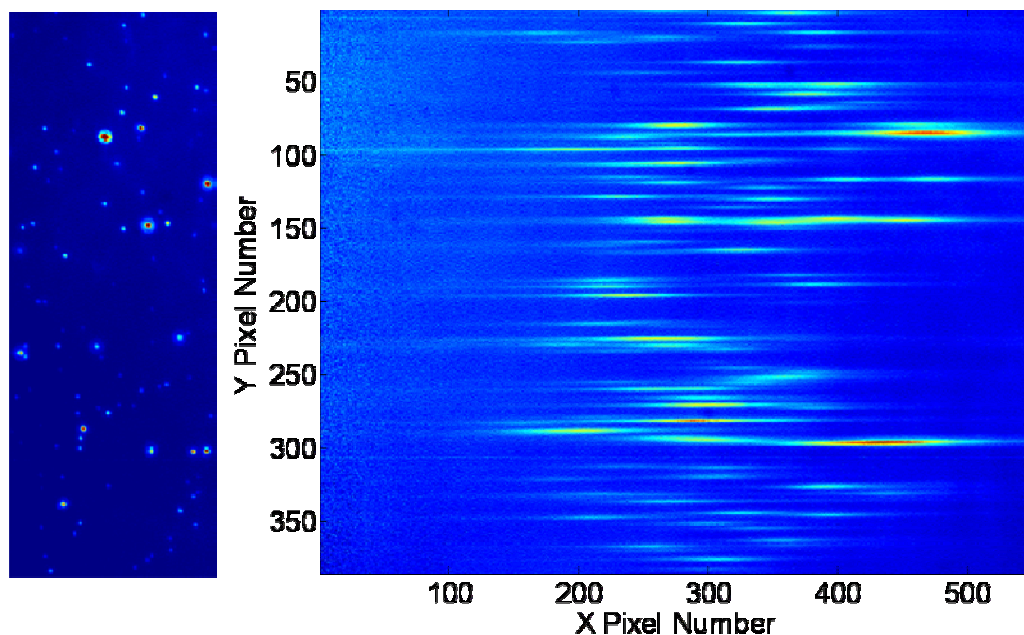
The second essential characteristic of the DOSI setup is that the entrance slit is dramatically widened. In conventional slit-imaging spectroscopy, optimum spectral resolution is achieved by matching the size of the entrance slit to the pixel pitch of the detection CCD. This prevents convolution of measured spectra by the spatial extent of the light imaged. However, we have shown previously that the width of the entrance slit can be a source of error when measuring spectral density of diffraction limited spots in darkfield due to the spatial distribution of light within the spot<sup>136</sup>. The effect this has on overall spectral resolution is mitigated by virtue of imaging sub-wavelength objects under darkfield illumination. The spatial extent of each spot is essentially self-limiting, as the physical extent is determined by the numeric aperture of the collecting optics. For single particle measurements, we showed that the optimal entrance slit width is 150  $\mu\text{m}$ . For DOSI, we opened the entrance slit to its full extent at 2.5 mm. Under 100X illumination, this provides a field of view approximately 25  $\mu\text{m}$  x 70  $\mu\text{m}$  that is spatially and spectrally addressable.

Figure 26 shows a typical raw DOSI micrograph of gold nanorods under darkfield illumination. The zero-order mode is visible in the left-hand portion of the image, with bright spots corresponding to nanorod scattering spots. The right-hand portion of the image is the first-order diffraction mode of the image and contains corresponding nanorod spots that are spread out along the width of the image which is the spots' wavelength dimension. Bright smears in the right-hand portion correspond to spectral peaks of individual particles.



**Figure 26: Raw DOSI micrograph of gold nanorods under darkfield illumination. Collected by a single CCD, the left-hand portion shows the zero-order mode of the nanoparticle field, and the right hand portion shows the first-order diffraction mode of the same field of view. The intensity map is falsely colored for visual ease.**

The first steps of DOSI data interpretation are identical to that of typical microspectroscopy. First, contributions due to dark current are removed by subtracting an image collected for the same integration time, but with no light exposure. Source correction is performed in a similar manner to the intrinsic correction method described in section 3.3.2. For the experiments described below, a single source spectrum was collected for each DOSI image by averaging together lines from the first-order portion of the image that did not exhibit nanoparticle spots. Each row of the first-order image was then divided by that acquired source spectrum. Figure 27 shows a source-corrected DOSI image.



**Figure 27: Zero-order (left) and first-order diffracted mode (right) of a source-corrected DOSI image.**

In this configuration, the position of the spectral peaks in the first-order image is determined by two factors. First, the spectral peak's position is determined by the spot's starting position in the zero-order image. The final position of the peak is determined by the distribution of its spectral content. The dispersion of the grating will shift longer wavelength components further to the right in the first-order image. LSPR shifts are measured as small perturbations in the positions of these peaks in first-order image. In order to observe small shifts in these peak locations due to local refractive index increases, it is necessary that contributions from these sources be decoupled, else mechanical drift caused by physical movement of the microscope stage relative to the detector could be misconstrued as LSPR peak shifts.

LSPR shifts between a test image and a reference image are decoupled from physical sample shifts by an image alignment algorithm<sup>227</sup> applied the zero-order portion

of the DOSI images. Alignment is performed by maximizing the cross correlation of the images. Alignment is calculated to a specified fraction of a pixel by up-sampling the cross-correlation matrix by the inverse of the defined fraction. For the studies described herein, an up-sampling factor of 100 was specified, registering images optimally to within 0.01 pixels. The alignment parameters determined for the zero-order images are then applied to the first-order images.

A peak finding algorithm<sup>228</sup> is applied to each line of the aligned first-order images. The algorithm operates by smoothing the data with a running average, and then locating peaks by thresholding the derivative of the line scan. A least-squares fit to a parabola is applied to the neighborhood around each potential peak. The peaks are then screened by height and width to exclude spectral features not expected arise from nanorod scattering. The peak location is considered the vertex of the fit parabola and has units of pixels but is not restricted to integer values since it was extracted from a least-squares fit. LSPR shifts are calculated in units of pixels as the difference in peak location in a reference image and the test image.

### **5.2.2 Experimental Results**

Nanorod and glass substrates were fabricated as described in section 4.1. Eight DOSI images were collected of the same nanorod substrate under each of five surrounding refractive index solutions containing 0, 20, 40, 60, and 80 percent glycerol (v/v) in water using a flow cell. The refractive index of these solutions is 1.333, 1.355, 1.392, 1.419, and 1.450 respectively. Image acquisition times varied from 0.2 to 0.4 seconds before the detector was saturated. Between each image, the microscope focus was purposely misaligned and then refocused to avoid potential influences of focus drift.

Figure 28 shows a line scan from a DOSI image collected of a nanorod sample in water. The first 200 pixels are from the zero-order mode image, and two peaks corresponding to nanorod scattering spots can be observed. The remainder of the line scan is the source corrected first-order diffraction mode of the image. Two peaks are observed, one corresponding to the LSPR of each particle. The two particles are physically separated by approximately 50 pixels in the zero-order mode. The two peaks in the first-order mode are also separated by approximately 50 pixels, indicating that the two nanoparticles have LSPR peaks at a similar peak wavelength. Figure 29 shows a plot that includes line scans from five images collected while the nanorod sample was under different volume percentages in glycerol. Both peaks can be observed to shift approximately 30 pixels to the right due to the increase in RI.

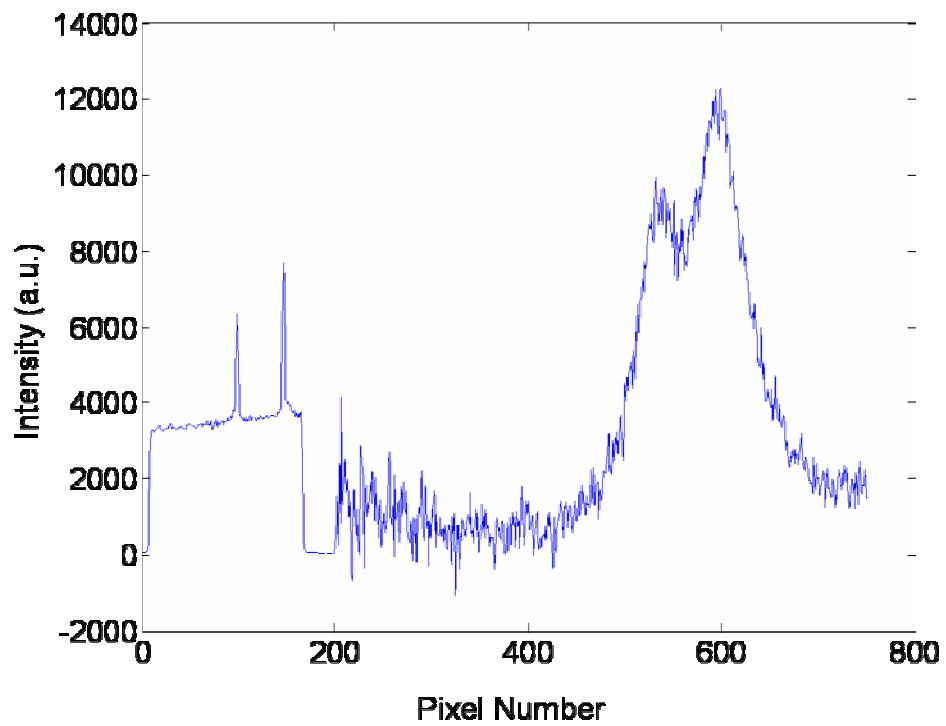


**Figure 28: Line scan of a DOSI image. The first 200 pixels are the zero-order mode and the remaining image is the source corrected first-order mode.**

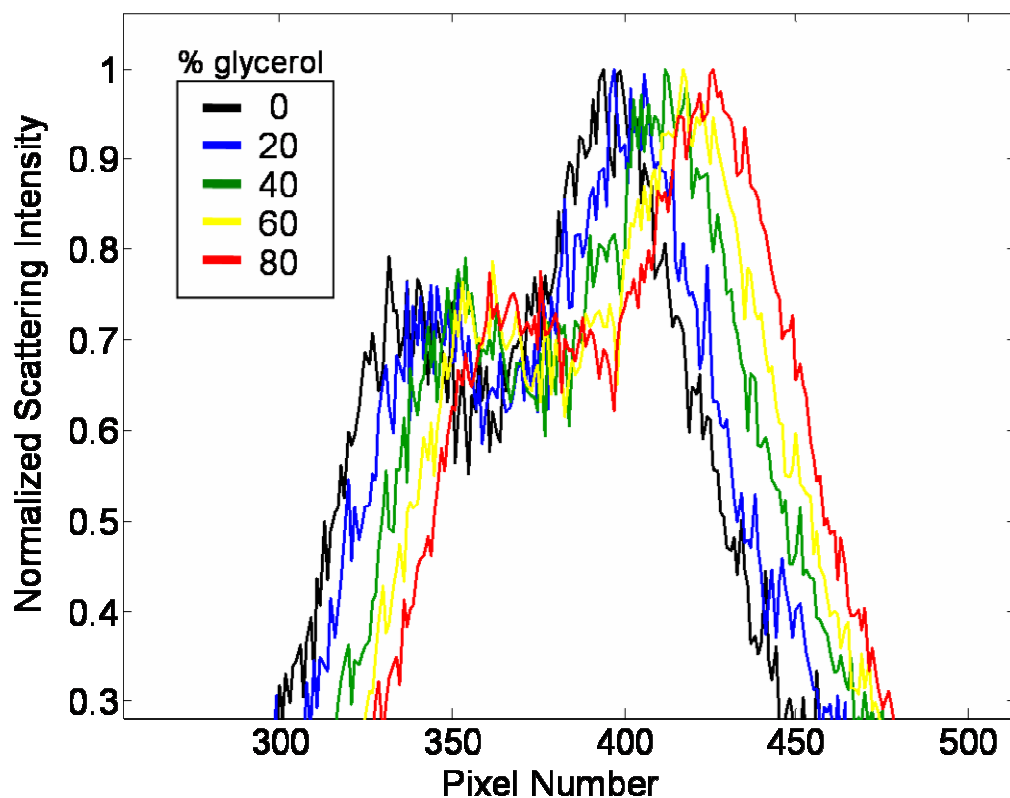


**Figure 29: DOSI spectra of two nanorods under five solutions with increasing refractive index.**

Forty DOSI images were analyzed to generate a statistical assessment of the system – eight at each of five RI solutions. Each first-order image contained approximately 350 peaks. The relationship between peak pixel position and peak wavelength was calculated using the dispersion of the grating to be 1.49 pixels/nm. This value allows the conversion of shifts and uncertainties originally calculated in pixels to be translated to nm for easier comparison. The variability in the measurement of each individual peak was determined by calculating the standard deviation of a peak’s location over the eight images collected under identical refractive index. The average standard deviation of individual peak measurements was 1.92 pixels. Applying the dispersion

relationship, this uncertainty translates to 1.29 nm. We term this value the peak measurement uncertainty.

To determine the overall measured RI shift, the measured shift of each of the approximately 350 peaks is considered. Figure 30 shows a plot of the mean peak pixel shift as a function of refractive index. For this measurement, each peak shift is measured as compared to DOSI images in water. A linear fit to this plot yields a slope that gives an approximate sensitivity of 204 pixels/RIU, which translates to 137 nm/RIU by the dispersion relation. This agrees well with the theoretically predicted value of 141 nm/RIU calculated by the model described in chapter 4 for rods that resonate at 644 nm in water. Error bars in the plot are the standard deviations of the peak mean shifts across the eight images collected at each RI. We term this value the image uncertainty, as it is based on in the total measurement from every peak measured in the DOSI image. The mean image uncertainty for the experiment described is 0.78 pixels, or 0.52 nm.

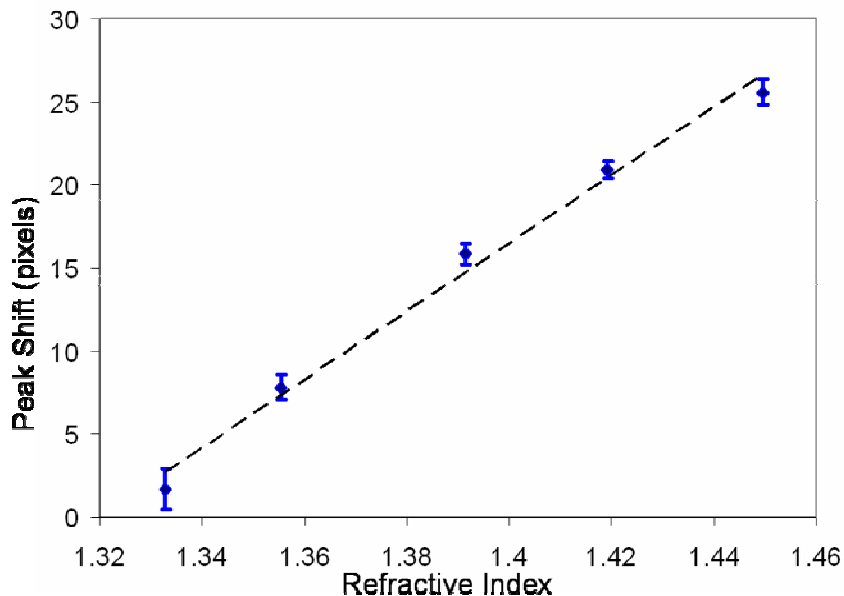


**Figure 30: Mean peak shift recorded for DOSI imaging of gold nanorods as a function of refractive index. Error bars indicate standard deviations from eight images at each RI.**

### 5.2.3 Discussion and Implications

We have shown that the DOSI strategy can be effectively used to measure LSPR peak shifts of gold nanorods as a function of local refractive index. By combining measurements gathered from several hundred peaks in a single image, averaged data from all spots can reliably measure LSPR peak changes as small as 0.52 nm. As a comparison, the measurement uncertainty of the single nanorod measurements described in section 4 is 0.3 nm. Thus, the fundamental sensitivity to refractive index of the system as measured by DOSI is slightly lower than that of the microspectroscopy system described in chapter 2 as a result of the lower spectral resolution. However, the system offers several advantages.

First and foremost, it provides intrinsic spatial registration of measured spectral densities. This would allow true multiplexed detection in an arrayed format. From

Figure 28, we observe that a lateral spatial separation of 50 pixels between detected spots in the zero-order image can be resolved spectroscopically, provided that the spectral line-widths are comparable to the nanorods used. If we assume spots are 5 pixels vertically and separated by 5 pixels between spots, then the 400 x 200 pixel size of the zero-order region of the CCD suggests that a 40 x 4, 160-element grid could be conceivably measured by DOSI. It may also be possible to further widen the entrance slit to enlarge the measured area, although at that point the second-order diffracted image may begin to overlap the first-order as can be barely noticed on the far right of figure 29. These grid elements need not be single nanorods for a parallel test. Each detection spot could be a patterned spot of many particles, or single plasmonic nanostructures as long as the background is dark and the objective magnification is adjusted so that the image is sized appropriately for the detector. In a multiplexed configuration where each peak is measured separately, the peak measurement uncertainty is increased to 1.29 nm per peak since all the measurements are not being pooled together to measure one unifying value.

In the application described in this section, DOSI is limited to measuring shifts in resonance peaks, and does not measure the absolute wavelength. However, this is not a critical limitation, as the dispersion of the grating should be constant across positions on the field of view, so that the 'center' blaze wavelength of each first-order diffracted peak will be the same distance away from its zero-order spot on the CCD. Even if small angular deviations in the ray trace of these spots exist, the system could easily be calibrated to take this effect into account upon data analysis. For example, this could be done by sweeping a monochromatic light source through various positions on the CCD and compiling the trends.

The higher light throughput of the DOSI system allows images to be collected at a faster rate than the single-particle microspectroscopy system. This increase is due to both the widening of the slit allowing more light through, and because the decreased dispersion of the grating directs the same amount of light to a narrower portion of the detector. The 0.2 – 0.4 second acquisition times per image represents a 100-fold increase in time resolution as compared to the 10-30 seconds required for each single nanorod measurement as described in section 4, and over four orders of magnitude faster than contemporary hyperspectral imaging that can take minutes to collect full spectra of a region.

Finally, the DOSI system is comprised entirely of commercially available parts which facilitates its use and development. Additionally, DOSI is less mechanically sensitive than microspectroscopy of a single nanorod. We have previously shown how translational drift of the image with respect to the slit, and focus drift both contribute to peak measurement uncertainty<sup>136</sup>. The translational drift problem is avoided in DOSI because of the self-registration between the zero and first-order images. The focus drift issue can be more readily addressed in DOSI than in the single particle microspectroscopy because of the 100-fold increase in frame rate allows more rapid feedback for focus controls, whether manual or automated. These increases in stability facilitate the ease of use of the detection system and increase its applicability to experiments requiring longer exposures.

## 6 Conclusions and Future Directions

### 6.1 Conclusions

The results described in this work demonstrate that gold nanorods are effective optical transducers and can be utilized in the development of label-free biosensors. A microspectroscopy system was developed to collect scattering spectra of single nanoparticles, and measure shifts of the spectra as a function of biomolecular binding. The measurement uncertainty of LSPR peak shifts of the system was demonstrated to be 0.3 nm. An analytical model was also developed that provides the optimal gold nanorod geometry for detection with specified receptor-analyte pair. The model was applied to the model biotin-streptavidin system, which resulted in sensing system with a detection limit of 130 pM – an improvement by four orders of magnitude over any other single-particle biodetection previously presented in the literature.

Alternative optical detection schemes were also investigated that could facilitate parallel biosensing. A theoretical model was built to investigate the efficacy of using a multi-channel CCD detector analogous to a conventional RGB camera. The results of the model indicated that even in the best case, the detection capabilities of such a system did not provide advantages over the microspectroscopic approach.

We presented a novel hyperspectral detection scheme we term Dual-Order Spectral Imaging (DOSI) which is capable of simultaneously measuring spectra of up to 160 individual regions within a microscope's field of view. This technique was applied to measuring shifts of individual nanoparticles and was found to have a peak measurement uncertainty of 1.29 nm, at a measurement rate of 2-5 Hz.

## 6.2 Future Directions

In section 4.4, several theoretical approaches were outlined that could potentially offer means to increase sensitivity of plasmonic nanoparticle-based biosensors. In this section, specific experiments are suggested that could be undertaken to realize distinctive gains in system sensitivity. These suggestions come from both newly published reports in the literature, and simply new insights on the part of the author.

### 6.2.1 Transducer Considerations

First, we discuss potential changes that can be made to the nanoparticle transducers themselves. In the presented experiments, nanoparticles were used that were composed of gold because although silver particles are more sensitive than gold particles of the same shape and size<sup>178, 205</sup>, the greater reactivity of silver as compared to gold makes it less suitable for use in biologically relevant media as silver can be easily oxidized, altering the plasmonic behavior of the particle. DNA detection studies have been conducted with silver nanoparticles synthesized with thin layer of gold on the outside to stabilize the particle surface<sup>229</sup>. The composite plasmon is dominated by the silver core, and is thus more sensitive than solid gold particles, but they retain the chemical stability of the gold. The use of particles of this type could potentially increase system sensitivity without sacrificing stability. An initial assessment of the gains achievable by such particles could be performed by a distance-dependent sensitivity test by layer-by-layer polyelectrolyte deposition. Comparison of the results of this test versus solid gold nanorods would determine the potential gains in sensitivity.

The final conclusion of the analytical model describing nanorod geometry-dependent sensor sensitivity was an optimized nanoparticle geometry. One constraint within the model was that the nanoparticles be large enough to present a scattering cross-section sufficiently large to achieve a threshold SNR in microspectroscopic images. The effect of this on the model was explicit cutoff of geometries that do not meet this requirement. Upon optimization, the nanorod geometry identified was near this cutoff barrier as shown in figure 14. Chemical synthesis techniques generate particles with geometries that are distributed around the mean values. If we assume that this is a normal distribution about the rod length and diameter, then  $\frac{3}{4}$  of the rods synthesized will have either a smaller diameter, or length or both. As the scattering cross section is positively dependent on these measurements, this means that these  $\frac{3}{4}$  of the particles will scatter less intensely and have a lower SNR when measured. Thus, it is suggested that the target nanorod geometry be shifted slightly towards larger particles, based on the standard deviations of the synthesized geometry. In this way, more particles will have spectra with SNR above the desired threshold.

Another potential gain in sensitivity - one that can potentially push the system over the limit of single molecule detection - is the localization of binding to the regions of highest field enhancement. It has been shown both theoretically<sup>230</sup> and experimentally<sup>146</sup> that there is a direct relationship between local field enhancement and local refractive index sensitivity. Thus, binding material selectively to the rod ends where field enhancement is greater<sup>231</sup> and preventing binding elsewhere will result in a much larger LSPR shift per bound analyte molecule. A recent thiol “replacement” strategy was reported wherein investigators first introduced a monolayer around gold nanorods through a thiol linkage with a glycol end-group to prevent non-specific adsorption. Then

the thiol replacement step consisted of a relatively short incubation with a molecule composed of a thiol end-group, and an end-group to which biotin can be conjugated. The theory is that the mobility of thiol-monolayers on gold allows the molecules on gold surface to be replaced by those in solution over time. Curved areas - such as at the rod ends - provide increased surface accessibility to the molecules in solution so they will be the ones replaced first. This approach has provided initial reductions of detection limits by a factor of 500<sup>216</sup>. However, assessing the effectiveness of this approach is not straightforward, as most means of sensor assessment to date rely on measuring saturation coverage. Therefore it is suggested that a time-resolved study, such as the type described in sections 3.2.2, be applied to “thiol-replaced,” biotin-conjugated nanorod detect streptavidin molecules.

Non-specific adsorption of molecules to sensor surfaces is a recurrent obstacle in the development of biosensing systems. In the nanorod detection system described in this work, the nanoparticle surfaces themselves were shown to resist non-specific adsorption of protein due to the mixed-monolayer of alkane SAM's conjugated to the particle surface. However, the large surface area of the glass substrate between nanoparticles is not similarly functionalized. This can have two effects on sensor performance. First, depletion can occur whereby target molecules are adsorbed to the glass substrate instead of to a nanoparticle, resulting in under-reporting of sample concentrations. Additionally, any material - whether it is target analyte or other constituents of a complex detection - will scatter light reducing SNR of darkfield micrographs. A recent approach employing surface-initiated EG polymer brushes to prevent non-specific adsorption was recently developed in our lab and has been shown to reduce background signals of a fluorescence protein array by a factor of 100

compared to EG monolayers<sup>232, 233</sup>. Applying this same technique to glass substrates on which detection is performed will result in higher SNR and improved detection limits.

## **6.2.2 DOSI Development**

### **6.2.2.1 Multiplexed detection**

The experiments outlined in section 5.2 demonstrate proof-of-concept of the DOSI system. The true power of the technique, however, lies in its capability of measuring multiplexed detection. To demonstrate this capability, an experiment should be performed that highlights this functionality. Ideally, a target substrate would consist of spots activated to bind different target analytes. Each spot could be individual nanoparticles of different geometries activated with different antibodies. For example, gold rods conjugated with an anti-goat IgG and gold spheres conjugated with anti-rabbit IgG could be deposited on a surface. Color images could be taken to first determine which particles are spheres, and which are rods. Then, as control solutions and rabbit and goat IgG are introduced, DOSI images could be collected as a function of time. Of course, each spot need not be an individual particle. Each spot could be nanoparticles patterned in a conventional microarray, with each spot corresponding to an ensemble measurement. Then each spot can be conjugated independently and the entire array can be measured by DOSI as test solutions are introduced. In this case, it is worth noting that it has been shown that LSPR detection schemes using particles at higher coverage measuring extinction spectra have a higher SNR than similar experiments based purely on scattering spectra<sup>115</sup>. However, the dark background required for DOSI might be a bit tricky to realize in an extinction-based illumination scheme.

### 6.2.2.2 DOSI Data Analysis

Through the course of analyzing the proof-of-concept DOSI measurements, several potential sources of error were identified that could potentially increase the accuracy of the technique if properly addressed. Several of these issues are concerning the determination of the source spectrum which is used to correct each measured peak.

In the analysis presented in section 5.2, a single source spectrum is collected from the entire image and is applied to each particle. This source is acquired as the average signal of all those lines which do not seem to exhibit spectral peaks. One improvement would be to iterate which rows are selected to contribute to the source spectrum since they are more easily identified once source correction is applied. Another improvement could allow contributions to the source to just come from the segments of any row that does exhibit a peak. So a single peak to the far right of the first-order image would not exclude the remainder of that row to contribute to the source. Finally, due to chromatic aberrations of the objective and potential misalignment of the entrance slit and detector CCD, the exact spectrum of the incident light could vary across the image. This is the region for using the spatially resolved intrinsic source correction described in section 2.3.1 where the source spectrum used for correction of each nanorod spot is collected only from rows nearby the spot. This is more of a challenge in DOSI because of the increased literal dimensionality reduces the number of rows without any scattering peaks. Perhaps by using some the techniques suggested above, it would be possible to ascertain local source spectra for each spot, increasing the accuracy of the corrected spectra.

Additionally, the source spectrum as measured by DOSI is convoluted by the spatial extent of the entrance slit width. It may be of use to deconvolute this effect before applying it to peaks for source correction.

The spectra of the spots themselves could also potentially benefit by some average across rows. In its current implementation, DOSI analyzes each peak on a row by row basis. So if one spot is large enough to cover pixels on four separate rows, it is currently measured as four separate peaks. By combining peaks across rows, higher SNR data could result in more accurate measures of peak shifts.

# Appendix A

# Analysis of total uncertainty in spectral peak measurements for plasmonic nanoparticle-based biosensors

Adam Curry, Gregory Nusz, Ashutosh Chilkoti, and Adam Wax

One goal of recent research on plasmonic nanoparticle-based sensors is maximizing nanoparticle sensitivity or shift of resonance peak wavelength per refractive index change. Equally important is a measurement system's peak location uncertainty or shift resolution. We provide systematic analyses and discuss optimization of factors that determine peak location uncertainty, reporting values as low as 0.3 nm for the presented scheme. This type of analysis is important, in part, because it provides a means of evaluating detection thresholds for biosensor applications such as analyte binding. We estimate thresholds of 310 streptavidin molecules for the presented scheme and 20 molecules with system improvements. © 2007 Optical Society of America

OCIS codes: 180.0180, 290.0290, 300.0300, 350.4990.

## 1. Introduction

The detection of single molecule binding events with plasmonic nanoparticles (NPs)<sup>1–8</sup> is the ultimate goal of plasmonic, and indeed all, biosensors. One proposed detection scheme depends on determining a shift in the NP's resonance wavelength due to a change in the refractive index (RI) of its local environment, which may be altered by a variety of test variables depending on application.<sup>9–13</sup> For such a scheme, the molecular detection threshold is determined by both the NP sensitivity, the optimization of which has been the goal of much recent research,<sup>2,3,8,14</sup> and the uncertainty in determining a resonance peak shift, or the peak shift resolution. A determination of the peak shift resolution requires careful analysis of experimental and theoretical uncertainties, many of which are specific to single NP microspectroscopy. An analysis of these factors is lacking in the current literature, yet is a critical consideration in NP biosensor design.

---

All the authors are with the Department of Biomedical Engineering, Duke University, Durham, North Carolina 27708. A. Curry (accurry@duke.edu) and A. Wax are also with the Fitzpatrick Institute for Photonics. G. Nusz and A. Chilkoti are also with the Center for Biologically Inspired Materials and Material Systems.

Received 3 July 2006; revised 26 September 2006; accepted 16 October 2006; posted 18 October 2006 (Doc. ID 72563); published 13 March 2007.

0003-6935/07/101931-09\$15.00/0  
© 2007 Optical Society of America

Here we present experimental and theoretical analyses of factors that govern the uncertainty in spectral peak determination for a line-imaging spectrometer, and we discuss the trade-offs inherent in optimizing each factor. The types of factor we consider are instrumental and analytical. Instrumental factors include objective NA, objective magnification, spectrometer slit width, NP image position ( $X, Y$ ) relative to the slit, and objective focus (or  $Z$  position of the particle, relative to the objective). Analytical factors include the extent of spatial averaging, the image region used for source spectrum determination, the signal-to-noise ratio (SNR) of the source-corrected spectrum, and the peak fitting algorithm employed. For the uncertainty determinations presented, we consider the case of a single, spherical, 80 nm diameter Au NP. This NP was chosen because it exhibits typical resonance wavelength and resonance peak width and because its resonance wavelength is in a region of high response for our microspectroscopy system. The NP sensitivity is not a consideration in peak location uncertainty, as these are independent parameters. Finally, we estimate a detection threshold for the current scheme based on the binding of streptavidin molecules to the NP biosensor.

## 2. Methods

### A. Experimental Scheme

The foundation of our microspectroscopy system<sup>14</sup> is a research grade inverted microscope (Axiovert 200,

Zeiss) equipped with 40× dry (Plan-Neofluar, Zeiss, NA of 0.75) and 100× oil immersion (Plan-Neofluar, Zeiss, adjustable NA from 0.7 to 1.4) objectives and a high-NA (1.2 to 1.4) oil immersion dark-field condenser. The microscope illumination is provided by a 100 W tungsten–halogen source. The microscope output can be directed to either a cooled color CCD (CoolSnap cf, Photometrics) for image registration or to a line imaging spectrometer (SpectraPro 2150i, Acton Research) for simultaneous measurement of 400 spectra along a line through the microscope field of view. The color coregistration camera CCD has dimensions of 1392 by 1040 pixels, with pixel dimensions of 4.65 μm × 4.65 μm. The line imaging spectrometer is equipped with a CCD (Spec-10, Roper Scientific), with dimensions of 1340 by 400 pixels and pixel dimensions of 20 μm × 20 μm. The spectrometer employs a slit aperture, the width of which is manually adjustable from 10 μm to 3 mm, and a 300 grooves/mm diffraction grating (reciprocal linear dispersion = 19 nm/mm) providing approximately 500 nm of dispersion over the CCD. The sample stage (KM Series, Semprex) is controlled by a motorized actuator (850G, Newport) and a custom LabVIEW interface for translation perpendicular to the spectrometer slit (*X*), and by a manual actuator for translation in the direction along the slit (*Y*).

**B. Uncertainty in Single Nanoparticle Microspectroscopy**  
Nanoparticles can be imaged with conventional optics only as diffraction-limited spots, because of their subwavelength dimensions. For a simple lens, the spectral and spatial distributions of diffraction-limited spots are defined by the familiar Airy pattern. Because of the wavelength dependence of diffraction, longer wavelengths have a larger Airy disk, resulting in a radial dependence of the spectral content of the diffraction-limited spot. The size of the spot on the image plane is determined by both the NA and the magnification of the imaging objective. Larger NA values result in smaller spots, while larger magnification values result in larger spots.

Determining resolution and uncertainty in the spectral analysis of diffraction-limited spots requires unique considerations. In standard spectroscopy applications, the size of the spectrometer entrance aperture is a determinant of spectral resolution. However, in the case of dark-field imaging of a diffraction-limited spot that is smaller than the aperture, the size of the imaged spot itself acts as the entrance aperture and enters into the calculation of spectral resolution. In this case, spectral uncertainty still exists to the degree that there is uncertainty in the spot position, but the loss of spectral resolution will be less than that predicted by the spectrometer aperture alone. Given these considerations, the spectrometer's entrance aperture size must be optimized to account for spot size, spectrometer resolution, and positioning uncertainty.

The studies described here were carried out to measure the total uncertainty in peak wavelength directly, as well as to isolate the contributions of in-

dividual factors to the total uncertainty. The total uncertainty was measured directly by repeated measurement of the scattering spectrum from a single NP, with experimental factors (*X*, *Y*, and *Z* particle position) varied and redetermined for each measurement. To isolate the contributions of individual factors, we conducted a series of measurements that are described in detail below. The results of the measurements are expressed as differentials,  $\partial\lambda_{\text{pk}}/\partial F$ , which are given as the resonance peak shift per unit change of factor *F* or as measured uncertainties  $U_F$  due to a given factor. The factors' differentials are combined with the factor's expected variabilities *V*, and the measured uncertainties to provide the total uncertainty, as shown by

$$U_{\text{total}}^2 = U_X^2 + U_Z^2 + U_Y^2 + U_{\text{fit}}^2 \\ = [(\partial\lambda/\partial X)V_X]^2 + [(\partial\lambda/\partial Z)V_Z]^2 + U_Y^2 + U_{\text{fit}}^2, \quad (1)$$

where *X*, *Y*, and *Z* represent the positions of the particle in the directions perpendicular to the spectrometer slit, along the slit, and normal to the focal plane (i.e., due to focus), respectively; and  $U_{\text{fit}}$  is the statistical uncertainty in measuring the peak of a spectrum with a given level of SNR. The individual factors are used to determine a calculated total uncertainty, which is compared with the measured total uncertainty to determine if the individual factors provide an accurate description.

#### C. Measurement of Total Uncertainty

For each slit width and objective (Table 1), a single, spherical, 80 nm diameter Au NP was chosen for analysis from a field of NPs bound to a silanated (aminopropyltriethoxysilane, Sigma) coverslip immersed in index-matching oil (*n* = 1.52). To directly measure the total uncertainty in peak wavelength determination, 50 spectra of the same NP were collected at different *Y* positions, and the *X* position was made to coincide with the center of the slit as accurately as possible with the existing scheme. Between each measurement, the NP was moved to an arbitrary intermediate point, and a manual hunt procedure was used to reposition the NP. The focus was monitored and adjusted as the operator deemed necessary.

#### D. Determination of Individual Differential and Variability Factors

To determine the *X* position differential ( $\partial\lambda_{\text{pk}}/\partial X$ ), spectra from single NPs were acquired as the NP was moved incrementally across the slit position (2 pixel

Table 1. Slit Widths Used in Study

Objective	Slit Widths (μm)
40×	20, 40, 60, 80, 100
100×	20, 60, 80, 100, 150

increments, as determined from the coregistration camera) over a 20 pixel range. The procedure was repeated for each slit width. The peak wavelengths were determined from the resulting spectra and compared with the  $X$  position. To determine the center of the NP from the coregistration camera, the red, green, and blue planes of the color image were summed to create a composite intensity image. The intensities were then integrated along both the  $X$  and the  $Y$  directions, and the NP image position was considered to be the pixel of peak integrated intensity. The positions of the NP images were also determined for the measurement of total uncertainty, with the standard deviations of the measured  $X$  positions across the measurements taken as the  $X$  position variabilities.

To develop a better understanding of the measured  $X$  differentials, we modeled the effects on the measured spectrum of slit width and NP position relative to the center of the slit. The model uses the on-axis point-spread function (PSF) of each objective for a NP with a representative spectrum (Lorentzian of 100 nm width, peaking at 640 nm), thereby accounting for both the spatial and the spectral variations in the diffraction-limited spot. The PSFs were spatially truncated according to the NP position and slit width under consideration. The measurement by a dispersive spectrometer is simulated by using the dispersion equation

$$X_{\text{detector}} = X_{\text{PSF}} + \alpha(\lambda - \lambda_{\text{center}}), \quad (2)$$

where  $X_{\text{detector}}$  is the location on the spectrometer CCD,  $X_{\text{PSF}}$  is the spatial location within the PSF,  $\alpha$  is the dispersion of the grating,  $\lambda$  is the wavelength of light, and  $\lambda_{\text{center}}$  is the center wavelength of the spectrometer.

To measure the  $Z$  position differential ( $\partial\lambda_{\text{pk}}/\partial Z$ ), spectra from single NPs were acquired as the objective focus knob was moved incrementally in 0.5  $\mu\text{m}$  steps through the best focus. The step value was chosen because it is half of the finest scale for the focus knob position. It is also less than the objectives' depths-of-field, which are 1.2 and 1.5  $\mu\text{m}$  for the 40 $\times$  and 100 $\times$  objectives, respectively. Mechanical hysteresis was avoided by moving the objective in only one direction throughout each series of measurements. The peak wavelengths were determined from the resulting spectra and compared with the focus knob position. The results were referenced to the best apparent focus, as determined from the coregistration images.

The uncertainty in the  $Y$  position of the NP relative to the spectrometer slit has a different origin from that of the  $X$  and  $Z$  position uncertainties. For slit-based imaging spectrometers, the image of a given wavelength at the detection plane exhibits a parabolic curvature with position along the slit. When this effect is not corrected by using a premeasured calibration, it introduces uncertainty in the measurement of the peak position. To evaluate the  $Y$  position uncertainty,  $U_Y$ , a 1 mm core fiber coupled to a

mercury–argon calibration lamp (HG-1, Ocean Optics) was imaged through the 40 $\times$  objective. This provides a spatially uniform spectral source that fills the spectrometer field of view (FOV) and contains narrow spectral lines across the visible wavelength range. The minimum slit width of 10  $\mu\text{m}$  was used since the broadening of peaks owing to a wider slit makes the peak wavelength positions less certain. The spectral peaks for wavelengths at each end of the spectral range were mapped versus positions along the spectrometer slit to determine the spectral variations with the slit position.

#### E. Determination of Uncertainty Attributable to Analytical Factors

To determine the uncertainty,  $U_{\text{fit}}$ , attributable to our peak fitting algorithm, we analyzed theoretically determined (Mie) scattering spectra, calculated at 1 nm spectral steps, for Ag spheres of 40, 60, 80, and 100 nm diameters. To each spectrum we added randomly generated noise at specific levels, producing spectra with SNR values of 10, 100, and 1000. Thirty fitting iterations for each sphere size and SNR value were analyzed with the random noise regenerated for each iteration, to obtain a statistical measure of the peak fitting uncertainty.

An additional source of uncertainty is the determination of the raw NP and source spectra used in processing the signals. Since a single NP image covers multiple rows of the spectrometer CCD, a group of adjacent rows corresponding with the NP must be averaged to determine the raw NP spectrum. The raw spectrum is then divided by a source spectrum to determine the scattering spectrum. The source spectrum is also an average of spectral rows, but from an adjacent region without NPs. These postprocessing steps include a number of variables that must be optimized for best repeatability. The parameters that were varied in the analysis were the number of spectral rows averaged to determine the source and the NP spectra and the offset from the NP spectra used in determining the source spectrum (Table 2). Prior to this analysis, measured dark signals were first subtracted from all the data.

#### F. Determination of Sensing Threshold

As an estimate of the sensing threshold achievable with our scheme, we consider a basic detection experiment in which a single 80 nm diameter Au sphere

Table 2. Standard Deviations of Peak Wavelength over all Data

Slit Width ( $\mu\text{m}$ )	avg = 7, offset = 8 <sup>a</sup>	avg = 7, offset = 20	avg = 13, offset = 20
20	1.94	1.79	1.57
50	1.45	1.24	1.03
100	0.52	0.41	0.32

<sup>a</sup>Here “avg” indicates the number of spectral rows averaged to create the raw NP and source spectra; offset indicates the number of spectral rows from the row of maximum NP intensity to the first row used for the source spectrum.

immobilized on glass is used to detect the binding of streptavidin molecules. The threshold estimate is based on the fraction of sensing volume that must be occupied by the target protein to induce the minimum detectable wavelength shift in the current scheme. We assume a uniform sensing volume extending one radius from the surface of the NP<sup>15–17</sup> into the surrounding environment above the glass substrate. We approximate the effective RI of the media surrounding the NP as the RIs of water and streptavidin scaled by their respective volume ratios, with streptavidin molecules modeled as 5 nm diameter spheres having RIs of 1.52<sup>18</sup> (e.g., for a sample that is 5% streptavidin by volume, the effective RI is  $1.33 \times .95 + 1.52 \times .05 = 1.34$ ). To determine the effect of the streptavidin on the resonance spectrum, we multiply the effective RI by a sensitivity of 120 nm/RI unit, which we have experimentally determined for 80 nm gold particles bound to glass. The resulting value is the theoretical surface plasmon resonance (SPR) wavelength shift induced by the presence of the streptavidin molecules, which is shown as

$$\lambda_{\text{shift}} = [1.33(1 - p) + 1.52p]S, \quad (3)$$

where  $\lambda_{\text{shift}}$  is the SPR peak shift,  $p$  is the volume ratio of streptavidin, and  $S$  is the particle wavelength sensitivity. The differential of Eq. (3) yields

$$\Delta\lambda_{\text{shift}} = 0.19S\Delta p, \quad (4)$$

where  $\Delta\lambda_{\text{shift}}$  is the change in the SPR peak location caused by an increase in the volume fraction of the streptavidin molecules,  $\Delta p$ . The change in streptavidin's volume fraction can be expressed in a number of molecules, which is shown as

$$\Delta p = (\Delta n v_s)/V, \quad (5)$$

where  $\Delta n$  is the change in the number of streptavidin molecules,  $v_s$  is the size of a streptavidin molecule, and  $V$  is the NP sensing volume. Substituting this into Eq. (4) and solving for  $\Delta n$  yields Eq. (6), which describes the molecular sensing threshold of a single NP sensing system:

$$\Delta n = (\Delta\lambda_{\text{shift}}V)/(0.19Sv_s). \quad (6)$$

By taking  $\Delta\lambda_{\text{shift}}$  as the minimum detectable peak shift, or the SPR peak measurement uncertainty, we can determine the relationship between our peak measurement uncertainty and the detection threshold for streptavidin molecules,  $\Delta n$ .

### 3. Results

#### A. Measurement of Total Uncertainty

The direct measurement of the total uncertainty (Fig. 1) reveals that the uncertainty in the peak wavelength determination decreases as the slit width

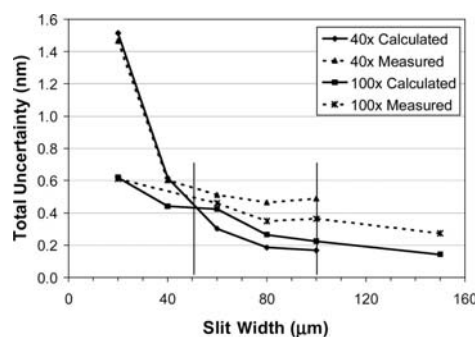


Fig. 1. Calculated and measured total uncertainties versus slit width for 40× and 100× objectives. The vertical lines on the left and right (50 and 100 μm) represent the distance between the first minima of NP diffraction-limited spots, at the image plane, for the 40× and 100× objectives, respectively. The calculated values match the measured values well for most data points, indicating that the calculation method accurately accounts for the dominant factors influencing the total uncertainty. The discrepancy for some data points for the 40× objective is attributed to variability in focus.

increases for both the 40× and the 100× objectives. The uncertainty for the 40× objective approaches a minimum measured value of approximately 0.5 nm and comes within 20% of that minimum value at a slit width of 40 μm. The uncertainty for the 100× objective approaches a minimum measured value of approximately 0.3 nm and falls within 20% of that minimum value at a slit width of 80 μm.

Figure 1 also presents a comparison of the calculated and measured total uncertainties. The calculated total uncertainties result from Eq. (1), with the factor values presented in Tables 3 through 5 for each slit width and objective. The determination of these factors is discussed in detail in Subsection 3.B.

#### B. Measurement of Individual Differentials and Sources of Uncertainty

An analysis of the variation of the NP's peak scattering wavelength with  $X$  position relative to the slit provides differentials that are approximately linear over the detectable range (Fig. 2). The measured differentials decrease with increasing slit width from  $-2.7$  to  $-0.1$  nm/pixel (wavelength shift/sample displacement) for the 40× objective, and from  $-0.6$  to  $-0.1$  nm/pixel for the 100× objective. The  $X$  differentials asymptotically approach  $-0.1$  nm/pixel for both objectives (Fig. 3), reaching this value at slit widths of 80 and 100 μm, respectively, for the 40×

Table 3. Variabilities

$V_z$ (μm)		$V_x$ (μm)	
40×	100×	40×	100×
0.15	0.15	0.55	0.7

**Table 4. Differentials**

Slit Width ( $\mu\text{m}$ )	$\partial\lambda/\partial Z$ ( $\text{nm}/\mu\text{m}$ )		$\partial\lambda/\partial X$ ( $\text{nm}/\text{pixel}$ )	
	40 $\times$	100 $\times$	40 $\times$	100 $\times$
20	-1.9	-3.0	-2.70	-0.60
40	-1.8	-2.9	-1.00	
60	-1.3	-2.4	-0.40	-0.30
80	-1.0	-1.7	-0.15	
100	-0.7	-1.3	-0.20	-0.12
150		-0.6		-0.12

and 100 $\times$  objectives. The variabilities in  $X$  are taken as the standard deviations in the  $X$  position, as determined from an analysis of the coregistration images and are determined to be approximately 0.5 and 0.7 pixels for the 40 $\times$  and 100 $\times$  objectives, respectively (Table 3).

The Airy pattern model results (Fig. 4) predict a differential that is approximately parabolic and symmetric about the slit center position when using a 100 $\times$  objective and a 20  $\mu\text{m}$  slit. If a 100  $\mu\text{m}$  slit width is used instead, the predicted differential is approximately linear and equal to the reciprocal linear dispersion of the grating.

Analyzing the variation of the peak scattering wavelength with change of focus ( $Z$ ) provides differentials (Fig. 5) that are also approximately linear over the detected range. The differentials decrease with increasing slit width from  $-1.9$  to  $-0.7$   $\text{nm}/\mu\text{m}$  (wavelength shift/objective displacement) for the 40 $\times$  objective, and from  $-3.0$  to  $-0.6$   $\text{nm}/\mu\text{m}$  for the 100 $\times$  objective. The  $Z$  differentials for both objectives are minimized at the largest slit width measured for each objective (Fig. 3). The variability in  $Z$  or focus (Table 3) is not easily determined but is expected to be less than the objectives' depths of field, which are 1.2 and 1.5  $\mu\text{m}$  for the 40 $\times$  and 100 $\times$  objectives, respectively. A value of 0.15  $\mu\text{m}$  was used in the calculations, based on the typical repeatability achieved by an experienced microscope operator.

An analysis of the calibration source measurement reveals the expected parabolic variation in peak pixel versus  $Y$  position on the spectrometer slit. The variation for the spectral line at 435.833 nm, which is representative, is  $\pm 1$  pixel along the entire slit. However, acquisitions are collected only within a region

**Table 5. Factor Uncertainties**

Slit Width ( $\mu\text{m}$ )	$U_Z$ (nm)		$U_X$ (nm)		$U_Y$ (nm)	$U_{\text{fit}}$ (nm)
	40 $\times$	100 $\times$	40 $\times$	100 $\times$		
20	0.29	0.45	1.49	0.42	0.07	0.02
40	0.27	0.44	0.55		0.07	0.02
60	0.20	0.36	0.22	0.21	0.07	0.02
80	0.15	0.26	0.08		0.07	0.02
100	0.11	0.20	0.11	0.08	0.07	0.02
150		0.09		0.08	0.07	0.02

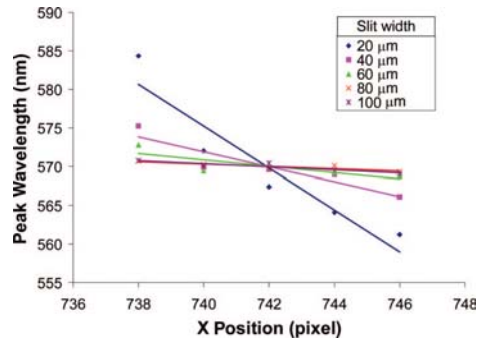


Fig. 2. (Color online) Variation in peak wavelength with NP  $X$  position for a 40 $\times$  objective at various slit widths. Linear fits reveal a decreasing slope, termed the differential, for the increasing slit width.

corresponding to the coregistration camera FOV, which is less than the spectrometer FOV. For the data presented here, data were collected across most of the coregistration camera FOV, giving spectral acquisitions between rows 80 and 300 of the spectrometer. A parabolic fit to the data in this range yields a standard deviation of 0.19 pixel, for an uncertainty  $U_Y$  of approximately 0.08 nm.

An analysis of the effect of the SNR (Fig. 6) on the uncertainty  $U_{\text{fit}}$  in fitting the peak reveals a linear dependence of the logarithm of peak uncertainty on the logarithm of SNR. The trend was examined for SNR values of 10, 100, and 1000. For the experimental data collected in this study a SNR value of 60–80 was achieved, providing peak fitting uncertainties of approximately 0.02 nm.

An analysis of the parameters used in determining the source and raw NP spectra (Table 2) indicate

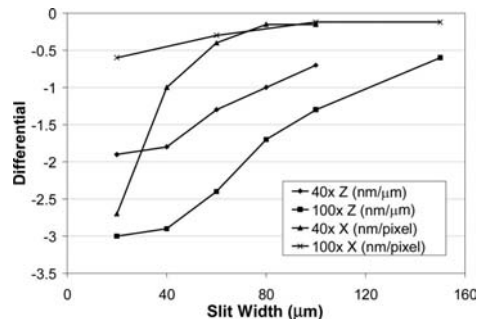


Fig. 3. Differentials due to  $X$  and  $Z$  (focus) positions versus slit width. The differentials with  $X$  approach an asymptotic value of approximately  $-0.1$   $\text{nm}/\text{pixel}$  ( $-0.02$   $\text{nm}/\mu\text{m}$ ), reaching that value for the 40 $\times$  and 100 $\times$  objectives at 80 and 100  $\mu\text{m}$ , respectively. This value matches the spectrometer grating's reciprocal linear dispersion. The differentials with  $Z$  reach their minimum values for the 40 $\times$  and 100 $\times$  objectives at slit widths of 100 and 150  $\mu\text{m}$ , respectively, which were the largest slit widths measured.

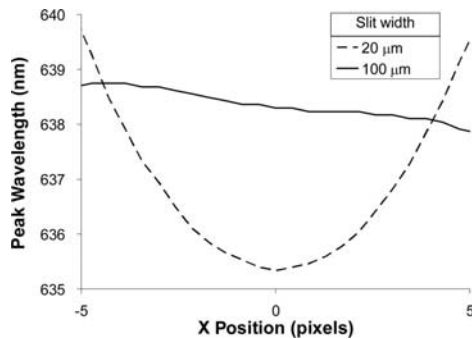


Fig. 4. On-axis Airy model predictions of the spectrometer slit width effect on spectral peak uncertainty due to  $X$  position for a  $100\times$  objective. For the  $20\ \mu\text{m}$  slit width, the predominant effect is truncation of the Airy pattern's radially dependent spectral content, which produces a symmetric variation in peak wavelength for NP image positions offset from the slit center position. Comparison with the experimental results for this case supports the conclusion of the comatic effects' dominance in the experimental results. For the  $100\ \mu\text{m}$  slit width, the predominant effect is a shift in the measured spectrum attributable to spatial shifts of the NP image. For both experimental and theoretical results, the spectral shift is roughly linear with the spatial shift and is equal to the spectrometer grating's reciprocal linear dispersion.

that, for the  $100\times$  objective, the uncertainty is minimized when the source spectrum is drawn from a region offset by 20 lines from the spectral row giving the maximum intensity for a given NP, and when 13 rows are averaged to create both the source and the raw NP spectra. A similar analysis for the  $40\times$  objective provided an optimal source spectrum drawn from a region offset by ten rows from the NP spectral row of maximum intensity, with nine rows averaged to create both the source and the raw NP spectra. These parameters were used for the total uncertainty determinations reported for each objective.

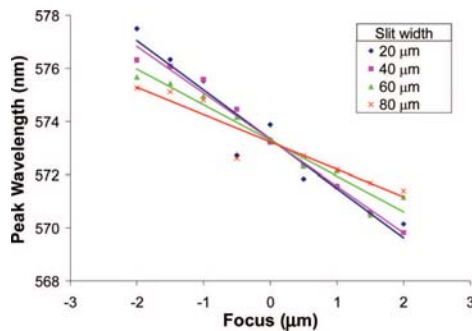


Fig. 5. (Color online) Variation in peak position with  $Z$  (focus) for a  $40\times$  objective and various slit widths. Linear fits reveal a decreasing slope, termed the differential, for increasing the slit width.

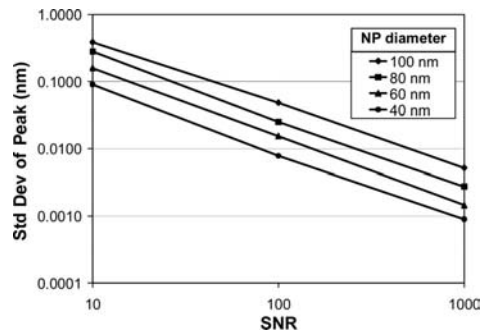


Fig. 6. Peak fitting uncertainties for Mie spectra with random noise applied to achieve a desired SNR value. The uncertainties provide a measure of the contribution of peak fitting to the total uncertainty. The uncertainties are the standard deviations in 30 peak measurements of a spectrum after application of random noise of appropriate value to achieve the desired SNR.

Having determined the total peak uncertainty in our sensing scheme, we are able to approximate our molecular detection threshold. To do so, we use Eq. (6) with  $v_s = 65\ \text{nm}^3$ ,  $V = 1.54 \times 10^9\ \text{nm}^3$ , and  $S = 120\ \text{nm}/\text{RI unit}$ . The lowest measured uncertainty, which corresponds to the  $100\times$  objective and a slit width of  $150\ \mu\text{m}$ , gives  $\Delta\lambda_{\text{shift}} = 0.3\ \text{nm}$ . Together, these parameters yield a sensing threshold of approximately 310 streptavidin molecules.

#### 4. Discussion

As our results indicate, large slit widths minimize the total measured uncertainties, providing uncertainties of 0.5 and 0.3 nm for the  $40\times$  and  $100\times$  objectives, respectively, for the largest slit widths in this study. In addition, the total uncertainty is well characterized by the individual factor uncertainties (Fig. 1), with focus and position being the most significant factors in the total uncertainty (Table 5). The minimum possible uncertainty, which is given by the noise-limited case (Fig. 6), may be achieved by increasing the spectrometer slit width, thereby minimizing the dominant factors' differentials ( $\partial\lambda/\partial X$  and  $\partial\lambda/\partial Z$ ), and by reducing the  $X$  and  $Z$  variabilities with appropriate hardware. This minimum or noise-limited uncertainty may then be used to determine the theoretical sensing threshold.

We have calculated that our current scheme's lowest measured uncertainty of  $\Delta\lambda_{\text{shift}} = 0.3\ \text{nm}$  yields a molecular detection threshold of approximately 310 streptavidin molecules. It is important to note that this approximation ignores the radial dependence of the NP RI sensitivity profile, which decays exponentially with distance from the NP surface. However, a realistic sensor will provide preferential binding of the target molecules to the NP surface. In addition, typical protocols incorporate a rinsing procedure, so that all the detected molecules are roughly an equal distance from the NP surface, in regions of comparable sensitivity. It is therefore reasonable to assume that the

sensitivity is uniform and that the measured signal is linear with the number of molecules bound.

Perhaps more important than the utility of this approximation in determining the absolute system detection threshold is that it provides insight into mechanisms for possible threshold reduction. For example, although much research in recent years has been dedicated to designing NPs with high sensitivity, sensitivity is only one of several variables that can reduce the sensing threshold of a biosensing system. In fact, integrating the most sensitive reported NPs for scatter in the visible range would reduce the sensing threshold by, at most, a factor of 3.<sup>19</sup> However, our analysis of peak measurement uncertainty indicates that the noise-limited case for our detection scheme is 0.02 nm, which correlates to a sensing threshold of approximately 20 molecules, suggesting that a reduction in peak measurement uncertainty can lower the sensing threshold by as much as a factor of 15.

As shown in Figs. 2 and 3, the  $X$  position of the NP has a significant effect on the peak wavelength, an effect that is approximately linear with position and that is minimized for larger slit widths. The results of the Airy pattern model are helpful in interpreting these results. The model illustrates two effects on the measured peak wavelength. The first is the truncation by the slit of the Airy pattern's radially dependent spectral content and a corresponding shift in the measured spectrum. This effect is apparent in the case of imaging a PSF at high magnification onto a narrow (20  $\mu\text{m}$ ) slit, in which case the differential is roughly parabolic and symmetric about the position of the slit center (Fig. 4). The second effect, which is attributable to the spectrometer grating, is a spectral shift in the measured spectrum upon a spatial shift of the NP image. The differential in this case approaches the reciprocal linear dispersion of the grating. This effect becomes more apparent as the slit gets large compared to the image of the PSF, as shown in the plot of the peak wavelength as a function of PSF translation across a 100  $\mu\text{m}$  slit (Fig. 4).

Both the model and the experimental results show a linear  $X$  differential that is equal to the grating dispersion for large slit widths (the grating dispersion is 0.019 nm/ $\mu\text{m}$ , and the minimum measured differentials are 0.032 and 0.026 nm/ $\mu\text{m}$  for the 40 $\times$  and 100 $\times$  objectives, respectively). However, the experimental results show a differential that is approximately linear for small slit widths, while the on-axis Airy pattern model predicts a differential that is parabolic. We attribute this effect to comatic aberration, which results from imaging at off-axis points and causes the image to exhibit a skewed spectral dependence away from the optical axis. In evaluating the experimental observation of coma, it is noteworthy that spectral shifts of the order of nanometers require a relatively small degree of coma, so the skewing is not expected to be apparent in either the coregistration or spectral images. We observe that the reduced spectral truncation of a large slit width reduces the

contribution of coma, allowing the differential to approach the minimum value set by the grating.

Two approaches may be used to minimize the peak uncertainty owing to variation in the  $X$  position: minimizing the  $X$  position differential or the  $X$  position variability. As we have shown, the differential may be reduced by increasing the slit width. Reducing the variability suggests implementing a sample stage with feedback to ensure precise sample placement. Feedback based on image analysis may provide adequate stability and positioning certainty, but this approach is generally slower than hardware-based approaches and requires an image from the coregistration camera for each correction. Alternatively, stages with hardware-based feedback, especially high-precision piezoelectrically controlled versions, can provide subnanometer resolution and repeatability of less than 5 nm (e.g., Physik Instrumente P541.2CD piezo stage). Positioning repeatability of this precision would reduce the uncertainty attributable to the  $X$  position to approximately 0.005 nm, an order of magnitude below the uncertainty attributable to fitting the peak.

The objective focus ( $Z$  position) also significantly affects the peak wavelength, as shown in Figs. 3 and 5, and the effect is again minimized for a large slit width. The focus effect is attributable to the variation with focus of the spatial distribution of the spectral content of the PSF. Minimizing the uncertainty attributable to focus may be accomplished by minimizing either the differential or the focus variability. As shown, the differential may be decreased with a larger slit width. Decreasing the uncertainty suggests implementing an autofocus module with feedback. Software-based autofocus routines do not provide the desired repeatability, which is substantially less than the objective's depth of field. However, recently released hardware-based autofocus options can limit drift to less than 40 nm/h (e.g., the Applied Scientific Instruments CRIFF system). Such low variability in the  $Z$  position yields peak wavelength uncertainties owing to  $Z$  of approximately 0.004 nm, an order of magnitude below the uncertainty attributable to fitting the peak.

The spectrometer exhibits the expected slit curvature along the  $Y$  direction, which results in a parabolic distribution of the calibration source peak wavelength along the slit. If a single calibration file is used for all the slit positions, as in the case of the presented data, a variation in the  $Y$  position introduces uncertainty in the peak position. However, the peak uncertainty due to the  $Y$  position is 0.08 nm, which is considerably less than the uncertainties due to  $X$  and  $Z$  in the current setup. Nonetheless, the variability due to the  $Y$  position may be corrected by establishing a wavelength calibration file that accounts for slit position.

As shown in Table 2, using a source drawn from a dark region of the spectral image sufficiently removed from the particle region provides the most repeatable peak measurements. While this approach reduces uncertainty in peak wavelength determination, it also decreases the spectral image FOV avail-

able for sample spectra. Table 2 also indicates that averaging over more spectral lines decreases uncertainty in the determination of peak wavelength. Again, this reduces spatial resolution and, therefore, the number of particles that can be scanned at once. However, we have found this to be the most repeatable means of source correcting the raw NP spectra.

Figure 6 shows the optimal case of noise-limited uncertainty. The statistical analysis of fitting a Gaussian peak to data indicates that the uncertainty  $\sigma_c$  on the peak position is given by  $\sigma_c = \sigma_x/\sqrt{N}$ , where  $\sigma_x$  is the Gaussian width, and  $N$  is the number of individual events recorded in the Gaussian distribution.<sup>20</sup> The dependence on the resonance peak width indicates that the advantages for the sensing threshold of a NP with high sensitivity may be offset if the NP also exhibits a broad peak, since broader peaks result in increased peak location uncertainty. This does not discount the importance of NP sensitivity, but does indicate that other factors of the NP resonance are important in determining sensing threshold. For a shot-noise limited measurement,  $\sqrt{N}$  is equal to the measurement SNR, so the uncertainty in peak position may be cast in the form:  $\sigma_c = \sigma_x/\text{SNR}$ , indicating a linear dependence of the logarithm of the uncertainty on the logarithm of the SNR. Our experimental determination shows the same dependence. The experimental spectra used in the analyses presented in this paper have SNR values of approximately 60 to 80, which correlates with noise-limited uncertainties of 0.02 nm (Fig. 6). As the contributions of the remaining individual factors in total uncertainty are reduced, the noise-limited uncertainty will become the dominant factor.

We see reduced agreement between the calculated and the measured uncertainties for the 40 $\times$  objective (Fig. 1) for some data points. This discrepancy may be attributable to the high dependence of total uncertainty on focus variability. Using a variability of 0.4 to 0.6  $\mu\text{m}$ , rather than 0.15  $\mu\text{m}$ , in the calculation produces a better match at those data points. Given the large depths of field of the objectives, these variability values are not unreasonable.

It is worth noting that temperature is an additional factor that affects the accuracy of measured nanoparticle spectra. Two temperature-dependent effects may alter NP resonance. The first is NP melting, which is a significant factor for particle diameters of approximately 20 nm or smaller. For these sizes, the melting temperature of the NPs is dramatically reduced from the bulk melting temperature,<sup>21</sup> and NP melting may be induced by microscope illumination. For larger NPs, temperature-induced shifts may be caused by the temperature dependence of the NP immersion medium RI. The immersion oil (Immersion 518F, Zeiss) used in these experiments has a temperature coefficient of  $3.8 \times 10^{-4}/\text{K}$ , which yields a peak shift of approximately 0.1 nm for a 5 K temperature increase (based on analysis of Mie spectra for an 80 nm Au sphere). Temperature fluctuations may result from NP absorption and heating, which occurs

over time scales of the order of picoseconds<sup>21</sup> and therefore adds little variability, or from source variations and/or bulk heating of the medium on longer time scales, which could introduce uncertainty in peak measurement.

## 5. Conclusion

We have presented an analysis of factors that influence the uncertainty in measurement of peak wavelength of plasmon resonant NPs. These factors include objective focus, NP location relative to the spectrometer slit, spectrometer slit width, and post-processing parameters. We observe an approximately linear  $X$  differential ( $\partial\lambda/\partial X$ ), which we attribute to a combination of comatic aberration and the translation of spatial shifts into apparent spectral shifts by the spectrometer grating. We have shown that within the depth of focus of the objective there is an approximately linear  $Z$  differential ( $\partial\lambda/\partial Z$ ). We have shown that the slit imaging spectrometer exhibits the expected dependence on the image's slit position ( $Y$ ), and we have found that this dependence accounts for only a small variation in peak wavelength, which can be accounted for in calibration. We have also calculated the uncertainty attributable to the fitting of typical spectra. By applying each of these factors to the calculation of total uncertainty, we have shown a good match to the experimental measurement of total uncertainty, indicating that we have identified the major contributors to total uncertainty. Finally, we have demonstrated experimental methods to optimize the slit width for peak wavelength uncertainty as a path to noise-limited measurement. The described analysis reveals that, for a 100 $\times$  objective, a slit width of 150  $\mu\text{m}$  minimizes the total uncertainty, providing a minimum reliably detected wavelength shift of 0.3 nm. Further analysis indicates that, based on this uncertainty, the detection threshold for a representative case of streptavidin binding 80 nm Au NPs on glass is approximately 310 molecules, but if sources of uncertainty are reduced to yield shot noise-limited uncertainty of 0.02 nm, a detection of binding from 20 molecules is possible. We believe the analyses described here are important for the further development of wavelength-dependent NP biosensors and provide an important framework for understanding their detection thresholds.

The authors thank John Pyhtila, Billy Hwang, and Mark Gu for their help with data acquisition and analysis; Michael Lavine for helpful conversations on statistical analysis of peak fitting; the Centers for Disease Control for financial support through grant NCID R01 CI-00097-01; and the Beverley and Clarence Chandran Research Award for financial support.

## References

1. A. J. Haes, D. A. Stuart, S. M. Nie, and R. P. Van Duyne, "Using solution-phase nanoparticles, surface-confined nanoparticle arrays, and single nanoparticles as biological sensing platforms," *J. Fluoresc.* **14**, 355–367 (2004).
2. G. Raschke, S. Kowarik, T. Franzl, C. Sonnichsen, T. A. Klar, J. Feldmann, A. Nichtl, and K. Kurzinger, "Biomolecular rec-

- ognition based on single gold nanoparticle light scattering," *Nano. Lett.* **3**, 935–938 (2003).
3. A. D. McFarland and R. P. Van Duyne, "Single silver nanoparticles as real-time optical sensors with zeptomole sensitivity," *Nano. Lett.* **3**, 1057–1062 (2003).
  4. C. Sonnichsen, S. Geier, N. E. Hecker, G. von Plessen, J. Feldmann, H. Ditlbacher, B. Lamprecht, J. R. Krenn, F. R. Aussenegg, V. Z. H. Chan, J. P. Spatz, and M. Moller, "Spectroscopy of single metallic nanoparticles using total internal reflection microscopy," *Appl. Phys. Lett.* **77**, 2949–2951 (2000).
  5. T. Itoh, T. Asahi, and H. Masuhara, "Direct demonstration of environment-sensitive surface plasmon resonance band in single gold nanoparticles," *Jpn. J. Appl. Phys. Part 2* **41**, L76–L78 (2002).
  6. H. Tamaru, H. Kuwata, H. T. Miyazaki, and K. Miyano, "Resonant light scattering from individual Ag nanoparticles and particle pairs," *Appl. Phys. Lett.* **80**, 1826–1828 (2002).
  7. J. J. Mock, M. Barbic, D. R. Smith, D. A. Schultz, and S. Schultz, "Shape effects in plasmon resonance of individual colloidal silver nanoparticles," *J. Chem. Phys.* **116**, 6755–6759 (2002).
  8. J. J. Mock, D. Smith, and S. Schultz, "Local refractive index dependence of plasmon resonance spectra from individual nanoparticles," *Nano. Lett.* **3**, 485–491 (2003).
  9. A. Curry, W. L. Hwang, and A. Wax, "Epi-illumination through the microscope objective applied to darkfield imaging and microspectroscopy of nanoparticle interaction with cells in culture," *Opt. Express* **14**, 6535–6542 (2006).
  10. N. Nath and A. Chilkoti, "Interfacial phase transition of an environmentally responsive elastin biopolymer adsorbed on functionalized gold nanoparticles studied by colloidal surface plasmon resonance," *J. Am. Chem. Soc.* **123**, 8197–8202 (2001).
  11. N. Nath and A. Chilkoti, "A colorimetric gold nanoparticle sensor to interrogate biomolecular interactions in real time on a surface," *Anal. Chem.* **74**, 504–509 (2002).
  12. C. Sonnichsen, B. Reinhard, J. Liphard, and A. Alivisatos, "A molecular ruler based on plasmon coupling of single gold and silver nanoparticles," *Nat. Biotechnol.* **23**, 741–745 (2005).
  13. A. Haes, W. Hall, L. Chang, W. Klein, and R. Van Duyne, "A localized surface plasmon resonance biosensor: First steps toward an assay for Alzheimer's disease," *Nano. Lett.* **4**, 1029–1034 (2004).
  14. A. Curry, G. Nusz, A. Chilkoti, and A. Wax, "Substrate effect on refractive index dependence of plasmon resonance for individual silver nanoparticles observed using darkfield microspectroscopy," *Opt. Express* **13**, 2668–2677 (2005).
  15. T. Okamoto, "Near-field spectral analysis of metallic beads," in *Near-Field Optics and Surface Plasmon Polaritons* (Springer, 2001), Vol. 81, pp. 97–122.
  16. D. D. Evanoff, R. L. White, and G. Chumanov, "Measuring the distance dependence of the local electromagnetic field from silver nanoparticles," *J. Phys. Chem. B* **108**, 1522–1524 (2004).
  17. M. Miller and A. Lazarides, "Controlling the sensing volume of metal nanosphere molecular sensors," in *Materials Research Society Symposium*, J. L. David, P. Taylor, D. McIlroy, L. Merhari, J. B. Pendry, J. T. Borenstein, P. Grodzinski, L. P. Lee, and Z. L. Wang, eds. (Materials Research Society, 2004), paper R6.5.
  18. J. Voros, "The density and refractive index of adsorbing protein layers," *Biophys. J.* **87**, 553–561 (2004).
  19. M. M. Miller and A. A. Lazarides, "Sensitivity of metal nanoparticle surface plasmon resonance to the dielectric environment," *J. Phys. Chem. B* **109**, 21556–21565 (2005).
  20. A. Davies and M. S. Levenson, "Estimating the root mean square of a wave front and its uncertainty," *Appl. Opt.* **40**, 6203–6209 (2001).
  21. M. Hu and G. V. Hartland, "Heat dissipation for Au particles in aqueous solution: Relaxation time versus size," *J. Phys. Chem. B* **106**, 7029–7033 (2002).

## References

1. Iqbal, S. S.; Mayo, M. W.; Bruno, J. G.; Bronk, B. V.; Batt, C. A.; Chambers, J. P., A review of molecular recognition technologies for detection of biological threat agents. *Biosensors & Bioelectronics* **2000**, 15, (11-12), 549-578.
2. Shiau, A. K.; Massari, M. E.; Ozbal, C. C., Back to basics: Label-free technologies for small molecule screening. *Combinatorial Chemistry & High Throughput Screening* **2008**, 11, (3), 231-237.
3. Ahmed, M. U.; Hossain, M. M.; Tamiya, E., Electrochemical biosensors for medical and food applications. *Electroanalysis* **2008**, 20, (6), 616-626.
4. Ebersole, R. C.; Ward, M. D., Amplified Mass Immunosorbent-Assay with a Quartz Crystal Microbalance. *Journal of the American Chemical Society* **1988**, 110, (26), 8623-8628.
5. Rodahl, M.; Hook, F.; Krozer, A.; Brzezinski, P.; Kasemo, B., Quartz-Crystal Microbalance Setup for Frequency and Q-Factor Measurements in Gaseous and Liquid Environments. *Review of Scientific Instruments* **1995**, 66, (7), 3924-3930.
6. Jonsson, M. P.; Jonsson, P.; Hook, F., Simultaneous Nanoplasmonic and Quartz Crystal Microbalance Sensing: Analysis of Biomolecular Conformational Changes and Quantification of the Bound Molecular Mass. *Analytical Chemistry* **2008**, 80, (21), 7988-7995.
7. Larsson, C.; Rodahl, M.; Hook, F., Characterization of DNA immobilization and subsequent hybridization on a 2D arrangement of streptavidin on a biotin-modified lipid bilayer supported on SiO<sub>2</sub>. *Analytical Chemistry* **2003**, 75, (19), 5080-5087.
8. BenDov, I.; Willner, I.; Zisman, E., Piezoelectric immunosensors for urine specimens of *Chlamydia trachomatis* employing quartz crystal microbalance microgravimetric analyses. *Analytical Chemistry* **1997**, 69, (17), 3506-3512.
9. Bizet, K.; Gabrielli, C.; Perrot, H., Biosensors based on piezoelectric transducers. *Analisis* **1999**, 27, (7), 609-616.
10. Wu, G. H.; Datar, R. H.; Hansen, K. M.; Thundat, T.; Cote, R. J.; Majumdar, A., Bioassay of prostate-specific antigen (PSA) using microcantilevers. *Nature Biotechnology* **2001**, 19, (9), 856-860.
11. Chou, S. S.; Kim, Y. Y.; Srivastava, A.; Murphy, B.; Balogun, O.; Tark, S. H.; Shekhawat, G.; Dravid, V. P., Microcantilever array with embedded metal oxide semiconductor field effect transistor actuators for deflection control, deflection sensing, and high frequency oscillation. *Applied Physics Letters* **2009**, 94, (22).

12. Cooper, M. A., Non-optical screening platforms: the next wave in label-free screening? *Drug Discovery Today* **2006**, 11, (23-24), 1068-1074.
13. Sadik, O. A.; Aluoch, A. O.; Zhou, A. L., Status of biomolecular recognition using electrochemical techniques. *Biosensors & Bioelectronics* **2009**, 24, (9), 2749-2765.
14. Newman, J. D.; Turner, A. P. F., Home blood glucose biosensors: a commercial perspective. *Biosensors and Bioelectronics* **2005**, 20, (12), 2435-2453.
15. Wang, J., Electrochemical biosensors: Towards point-of-care cancer diagnostics. *Biosensors and Bioelectronics* **2006**, 21, (10), 1887-1892.
16. Musameh, M.; Wang, J.; Merkoci, A.; Lin, Y., Low-potential stable NADH detection at carbon-nanotube-modified glassy carbon electrodes. *Electrochemistry Communications* **2002**, 4, (10), 743-746.
17. Dequaire, M.; Degrand, C.; Limoges, B., An Electrochemical Metalloimmunoassay Based on a Colloidal Gold Label. *Analytical Chemistry* **2000**, 72, (22), 5521-5528.
18. Yogeswaran, U.; Chen, S.-M., A Review on the Electrochemical Sensors and Biosensors Composed of Nanowires as Sensing Material. *Sensors* **2008**, 8, (1), 290-313.
19. Stewart, M. E.; Anderton, C. R.; Thompson, L. B.; Maria, J.; Gray, S. K.; Rogers, J. A.; Nuzzo, R. G., Nanostructured plasmonic sensors. *Chemical Reviews* **2008**, 108, (2), 494-521.
20. Kneipp, K.; Kneipp, H.; Itzkan, I.; Dasari, R. R.; Feld, M. S., Ultrasensitive chemical analysis by Raman spectroscopy. *Chemical Reviews* **1999**, 99, (10), 2957-+.
21. Fleischm.M; Hendra, P. J.; McQuilla.Aj, Raman-Spectra of Pyridine Adsorbed at a Silver Electrode. *Chemical Physics Letters* **1974**, 26, (2), 163-166.
22. Albrecht, M. G.; Creighton, J. A., Anomalously intense Raman spectra of pyridine at a silver electrode. *Journal of the American Chemical Society* **2002**, 99, (15), 5215-5217.
23. Jeanmaire, D. L.; Van Duyne, R. P., Surface raman spectroelectrochemistry: Part I. Heterocyclic, aromatic, and aliphatic amines adsorbed on the anodized silver electrode. *Journal of Electroanalytical Chemistry* **1977**, 84, (1), 1-20.
24. Haynes, C. L.; McFarland, A. D.; Van Duyne, R. P., Surface-enhanced Raman spectroscopy. *Analytical Chemistry* **2005**, 77, (17), 338A-346A.
25. Lyandres, O.; Shah, N. C.; Yonzon, C. R.; Walsh, J. T.; Glucksberg, M. R.; Van Duyne, R. P., Real-time glucose sensing by surface-enhanced Raman

- spectroscopy in bovine plasma facilitated by a mixed decanethiol/mercaptohexanol partition layer. *Analytical Chemistry* **2005**, 77, (19), 6134-6139.
26. Stuart, D. A.; Yonzon, C. R.; Zhang, X. Y.; Lyandres, O.; Shah, N. C.; Glucksberg, M. R.; Walsh, J. T.; Van Duyne, R. P., Glucose sensing using near-infrared surface-enhanced Raman spectroscopy: Gold surfaces, 10-day stability, and improved accuracy. *Analytical Chemistry* **2005**, 77, (13), 4013-4019.
  27. Vo-Dinh, T.; Allain, L. R.; Stokes, D. L., Cancer gene detection using surface-enhanced Raman scattering (SERS). *Journal Of Raman Spectroscopy* **2002**, 33, (7), 511-516.
  28. Han, X. X.; Zhao, B.; Ozaki, Y., Surface-enhanced Raman scattering for protein detection. *Analytical and Bioanalytical Chemistry* **2009**, 394, (7), 1719-1727.
  29. Zhang, X. Y.; Young, M. A.; Lyandres, O.; Van Duyne, R. P., Rapid detection of an anthrax biomarker by surface-enhanced Raman spectroscopy. *Journal of the American Chemical Society* **2005**, 127, (12), 4484-4489.
  30. Kneipp, K.; Wang, Y.; Kneipp, H.; Perelman, L. T.; Itzkan, I.; Dasari, R.; Feld, M. S., Single molecule detection using surface-enhanced Raman scattering (SERS). *Physical Review Letters* **1997**, 78, (9), 1667-1670.
  31. Xu, H. X.; Bjerneld, E. J.; Kall, M.; Borjesson, L., Spectroscopy of single hemoglobin molecules by surface enhanced Raman scattering. *Physical Review Letters* **1999**, 83, (21), 4357-4360.
  32. Rich, R. L.; Myszka, D. G., Survey of the year 2007 commercial optical biosensor literature. *Journal of Molecular Recognition* **2008**, 21, (6), 355-400.
  33. Liedberg, B.; Nylander, C.; Lundstrom, I., Surface-Plasmon Resonance for Gas-Detection and Biosensing. *Sensors and Actuators* **1983**, 4, (2), 299-304.
  34. Malmqvist, M., Biospecific Interaction Analysis Using Biosensor Technology. *Nature* **1993**, 361, (6408), 186-187.
  35. Malmborg, A. C.; Michaelsson, A.; Ohlin, M.; Jansson, B.; Borrebaeck, C. A. K., Real-Time Analysis of Antibody Antigen Reaction-Kinetics. *Scandinavian Journal of Immunology* **1992**, 35, (6), 643-650.
  36. Hoa, X. D.; Kirk, A. G.; Tabrizian, M., Towards integrated and sensitive surface plasmon resonance biosensors: A review of recent progress. *Biosensors and Bioelectronics* **2007**, 23, (2), 151-160.
  37. Rothenhausler, B.; Knoll, W., Surface-Plasmon Microscopy. *Nature* **1988**, 332, (6165), 615-617.

38. Johansen, K.; Arwin, H.; Lundstrom, I.; Liedberg, B., Imaging surface plasmon resonance sensor based on multiple wavelengths: Sensitivity considerations. *Review of Scientific Instruments* **2000**, 71, (9), 3530-3538.
39. Singh, B. K.; Hillier, A. C., Multicolor surface plasmon resonance imaging of ink jet-printed protein microarrays. *Analytical Chemistry* **2007**, 79, (14), 5124-5132.
40. Shen, G. Y.; Han, Z. Q.; Liu, W.; Chen, Y., Color surface plasmon resonance imaging of protein microdot arrays. *Chemistry Letters* **2007**, 36, (7), 926-927.
41. Bohren, C. F.; Huffman, D. R., *Absorption and Scattering of Light by Small Particles*. Wiley-VCH Weinheim, 2004.
42. Yguerabide, J.; Yguerabide, E. E., Light-scattering submicroscopic particles as highly fluorescent analogs and their use as tracer labels in clinical and biological applications - II. Experimental characterization. *Analytical Biochemistry* **1998**, 262, (2), 157-176.
43. Link, S.; El-Sayed, M. A., Spectral properties and relaxation dynamics of surface plasmon electronic oscillations in gold and silver nanodots and nanorods. *Journal of Physical Chemistry B* **1999**, 103, (40), 8410-8426.
44. Ershov, B. G.; Sukhov, N. L., Effect of the size and shape of platinum nanoparticles on their optical absorption spectra in aqueous solutions. *Russian Journal of Physical Chemistry* **2001**, 75, (8), 1303-1306.
45. Kapoor, S.; Palit, D. K.; Mukherjee, T., Preparation, characterization and surface modification of Cu metal nanoparticles. *Chemical Physics Letters* **2002**, 355, (3-4), 383-387.
46. Link, S.; Mohamed, M. B.; El-Sayed, M. A., Simulation of the Optical Absorption Spectra of Gold Nanorods as a Function of Their Aspect Ratio and the Effect of the Medium Dielectric Constant. *Journal of Physical Chemistry B* **1999**, 103, 3073-3077.
47. Sonnichsen, C.; Alivisatos, A. P., Gold nanorods as novel nonbleaching plasmon-based orientation sensors for polarized single-particle microscopy. *Nano Letters* **2005**, 5, (2), 301-304.
48. Mock, J. J.; Barbic, M.; Smith, D. R.; Schultz, D. A.; Schultz, S., Shape Effects in Plasmon Resonance of Individual Colloidal Silver Nanoparticles. *Journal of Chemical Physics* **2002**, 116, (15).
49. Frederix, F.; Friedt, J. M.; Choi, K. H.; Laureyn, W.; Campitelli, A.; Mondelaers, D.; Maes, G.; Borghs, G., Biosensing based on light absorption of nanoscaled gold and silver particles. *Analytical Chemistry* **2003**, 75, (24), 6894-6900.

50. Jana, N. R.; Gearheart, L.; Murphy, C. J., Seed-Mediated Growth Approach for Shape-Controlled Synthesis of Spheroidal and Rod-like Gold Nanoparticles Using a Surfactant Template. *Advanced Materials* **2001**, 13, (18), 1389-1393.
51. Natan, M. J.; Grabar, K. C.; Smith, P. C.; Musick, M. D.; Davis, J. A.; Walter, D. G.; Jackson, M. A.; Guthrie, A. P., Kinetic control of interparticle spacing in Au colloid-based surfaces: Rational nanometer-scale architecture. *Journal of the American Chemical Society* **1996**, 118, (5), 1148-1153.
52. Xia, Y. N.; Wiley, B.; Herricks, T.; Sun, Y. G., Polyol synthesis of silver nanoparticles: Use of chloride and oxygen to promote the formation of single-crystal, truncated cubes and tetrahedrons. *Nano Letters* **2004**, 4, (9), 1733-1739.
53. Chen, S. H.; Li, D. G.; Zhao, S. Y.; Hou, X. M.; Ma, H. Y.; Yang, X. G., Simple method for preparation of cubic Ag nanoparticles and their self-assembled films. *Thin Solid Films* **2004**, 460, (1-2), 78-82.
54. Malinsky, M. D.; Kelly, K. L.; Schatz, G. C.; Van Duyne, R. P., Chain length dependence and sensing capabilities of the localized surface plasmon resonance of silver nanoparticles chemically modified with alkanethiol self-assembled monolayers. *Journal Of The American Chemical Society* **2001**, 123, (7), 1471-1482.
55. Averitt, R. D.; Westcott, S. L.; Halas, N. J., Linear optical properties of gold nanoshells. *Journal of the Optical Society of America B-Optical Physics* **1999**, 16, (10), 1824-1832.
56. Raschke, G.; Brogl, S.; Sussha, A. S.; Rogach, A. L.; Klar, T. A.; Feldmann, J.; Fieres, B.; Petkov, N.; Bein, T.; Nichtl, A.; Kurzinger, K., Gold nanoshells improve single nanoparticle molecular sensors. *Nano Letters* **2004**, 4, (10), 1853-1857.
57. Shumaker-Parry, J. S.; Rochholz, H.; Kreiter, M., Fabrication of crescent-shaped optical antennas. *Advanced Materials* **2005**, 17, (17), 2131-+.
58. Chou, S. Y.; Krauss, P. R.; Zhang, W.; Guo, L. J.; Zhuang, L., Sub-10 nm imprint lithography and applications. *Journal of Vacuum Science & Technology B* **1997**, 15, (6), 2897-2904.
59. Hao, E.; Schatz, G. C., Electromagnetic fields around silver nanoparticles and dimers. *Journal of Chemical Physics* **2004**, 120, (1), 357-366.
60. Xiao, J. J.; Huang, J. P.; Yu, K. W., Optical response of strongly coupled metal nanoparticles in dimer arrays. *Physical Review B* **2005**, 71, (4).
61. Jensen, T.; Kelly, L.; Lazarides, A.; Schatz, G. C., Electrodynamics of noble metal nanoparticles and nanoparticle clusters. *Journal Of Cluster Science* **1999**, 10, (2), 295-317.

62. Prikulis, J.; Svedberg, F.; Kall, M.; Enger, J.; Ramser, K.; Goksor, M.; Hanstorp, D., Optical spectroscopy of single trapped metal nanoparticles in solution. *Nano Letters* **2004**, 4, (1), 115-118.
63. Storhoff, J. J.; Elghanian, R.; Mucic, R. C.; Mirkin, C. A.; Letsinger, R. L., One-pot colorimetric differentiation of polynucleotides with single base imperfections using gold nanoparticle probes. *Journal of the American Chemical Society* **1998**, 120, (9), 1959-1964.
64. Mock, J. J.; Hill, R. T.; Degiron, A.; Zauscher, S.; Chilkoti, A.; Smith, D. R., Distance-Dependent Plasmon Resonant Coupling between a Gold Nanoparticle and Gold Film. *Nano Lett.* **2008**.
65. Henglein, A.; Meisel, D., Spectrophotometric observations of the adsorption of organosulfur compounds on colloidal silver nanoparticles. *Journal of Physical Chemistry B* **1998**, 102, (43), 8364-8366.
66. Linnert, T.; Mulvaney, P.; Henglein, A., Surface-Chemistry of Colloidal Silver - Surface-Plasmon Damping by Chemisorbed I-, Sh-, and C6h5s. *Journal of Physical Chemistry* **1993**, 97, (3), 679-682.
67. Kamat, P. V., Photophysical, photochemical and photocatalytic aspects of metal nanoparticles. *Journal of Physical Chemistry B* **2002**, 106, (32), 7729-7744.
68. Kreibig, U.; Gartz, M.; Hilger, A., Mie resonances: Sensors for physical and chemical cluster interface properties. *Berichte Der Bunsen-Gesellschaft-Physical Chemistry Chemical Physics* **1997**, 101, (11), 1593-1604.
69. Englebienne, P., Use of colloidal gold surface plasmon resonance peak shift to infer affinity constants from the interactions between protein antigens and antibodies specific for single or multiple epitopes. *Analyst* **1998**, 123, (7), 1599-1603.
70. Nath, N.; Chilkoti, A., A colorimetric gold nanoparticle sensor to interrogate biomolecular interactions in real time on a surface. *Analytical Chemistry* **2002**, 74, (3), 504-509.
71. Nath, N.; Chilkoti, A., Label-free biosensing by surface plasmon resonance of nanoparticles on glass: Optimization of nanoparticle size. *Analytical Chemistry* **2004**, 76, (18), 5370-5378.
72. Marinakos, S. M.; Chen, S.; Chilkoti, A., Plasmonic Detection of a Model Analyte in Serum by a Gold Nanorod Sensor. *Analytical Chemistry* **2007**, 79, (14), 5278-5283.
73. Haes, A. J.; Stuart, D. A.; Nie, S. M.; Van Duyne, R. P., Using solution-phase nanoparticles, surface-confined nanoparticle arrays and single nanoparticles as biological sensing platforms. *Journal of Fluorescence* **2004**, 14, (4), 355-367.

74. Haes, A. J.; Van Duyne, R. P., A nanoscale optical biosensor: Sensitivity and selectivity of an approach based on the localized surface plasmon resonance spectroscopy of triangular silver nanoparticles. *Journal Of The American Chemical Society* **2002**, 124, (35), 10596-10604.
75. Nusz, G. J.; Marinakos, S. M.; Curry, A. C.; Dahlin, A.; Höök, F.; Wax, A.; Chilkoti, A., Label-Free Plasmonic Detection of Biomolecular Binding by a Single Gold Nanorod. *Analytical Chemistry* **2008**, 80, (4), 984-989.
76. McFarland, A. D.; Van Duyne, R. P., Single silver nanoparticles as real-time optical sensors with zeptomole sensitivity. *Nano Letters* **2003**, 3, (8), 1057-1062.
77. Rindzevicius, T.; Alaverdyan, Y.; Dahlin, A.; Hook, F.; Sutherland, D. S.; Kall, M., Plasmonic sensing characteristics of single nanometric holes. *Nano Letters* **2005**, 5, (11), 2335-2339.
78. Piliarik, M.; Vala, M.; Tichy, I.; Homola, J., Compact and low-cost biosensor based on novel approach to spectroscopy of surface plasmons. *Biosensors & Bioelectronics* **2009**, 24, (12), 3430-3435.
79. Jung, L. S.; Campbell, C. T.; Chinowsky, T. M.; Mar, M. N.; Yee, S. S., Quantitative interpretation of the response of surface plasmon resonance sensors to adsorbed films. *Langmuir* **1998**, 14, (19), 5636-5648.
80. Nusz, G. J.; Curry, A. C.; Marinakos, S. M.; Wax, A.; Chilkoti, A., Rational Selection of Gold Nanorod Geometry for Label-Free Plasmonic Biosensors. *ACS Nano* **2009**, 0, (0).
81. Liedberg, B.; Lundstrom, I.; Stenberg, E., Principles of Biosensing with an Extended Coupling Matrix and Surface-Plasmon Resonance. *Sensors and Actuators B-Chemical* **1993**, 11, (1-3), 63-72.
82. Imura, K.; Okamoto, H.; Nagahra, T., Plasmon Mode Imaging of Single Gold Nanorods. *JACS Communications* **2004**.
83. Tseng, A. A.; Diaz, R. E.; Chen, C. D.; Wu, C. S., Fabrication of microbowtie structures for optical probing of nanoscale objects. *Microsystem Technologies-Micro-and Nanosystems-Information Storage and Processing Systems* **2003**, 9, (5), 335-339.
84. Lu, Y.; Liu, G. L.; Kim, J.; Meija, Y. X.; Lee, L. P., Nanophotonic Crescent Moon Structures with Sharp Edge for Ultrasensitive Biomolecular Detection by Local Electromagnetic Field Enhancement Effect. *Nano Letters* **2005**, 5, (1), 119-124.
85. Gillis, E. H.; Gosling, J. P.; Sreenan, J. M.; Kane, M., Development and validation of a biosensor-based immunoassay for progesterone in bovine milk. *Journal of Immunological Methods* **2002**, 267, (2), 131-138.

86. Rosi, N. L.; Mirkin, C. A., Nanostructures in biodiagnostics. *Chemical Reviews* **2005**, 105, (4), 1547-1562.
87. Mitchell, J. S.; Wu, Y. Q.; Cook, C. J.; Main, L., Sensitivity enhancement of surface plasmon resonance biosensing of small molecules. *Analytical Biochemistry* **2005**, 343, (1), 125-135.
88. Neely, A.; Perry, C.; Varisli, B.; Singh, A. K.; Arbnesi, T.; Senapati, D.; Kalluri, J. R.; Ray, P. C., Ultrasensitive and Highly Selective Detection of Alzheimer's Disease Biomarker Using Two-Photon Rayleigh Scattering Properties of Gold Nanoparticle. *Acs Nano* **2009**, 3, (9), 2834-2840.
89. Kreuzer, M. P.; Quidant, R.; Salvador, J. P.; Marco, M. P.; Badenes, G., Colloidal-based localized surface plasmon resonance (LSPR) biosensor for the quantitative determination of stanzolol. *Analytical and Bioanalytical Chemistry* **2008**, 391, (5), 1813-1820.
90. Fu, J. X.; Park, B.; Zhao, Y. P., Limitation of a localized surface plasmon resonance sensor for Salmonella detection. *Sensors and Actuators B-Chemical* **2009**, 141, (1), 276-283.
91. Wu, H. T.; Chen, Y. L.; Huang, Y. C.; Liu, W. C.; Ng, M. Y.; Chang, Y. F.; Hsieh, B. Y.; Chou, C., Colloid-gold nanoparticle enhanced detection sensitivity of paired surface plasma waves biosensor - art. no. 64470S. In *Nanoscale Imaging, Spectroscopy, Sensing, and Actuation for Biomedical Applications IV*, Cartwright, A. N.; Nicolau, D. V., Eds. Spie-Int Soc Optical Engineering: Bellingham, 2007; Vol. 6447, pp S4470-S4470.
92. Lee, J. H.; Kang, D. Y.; Lee, T.; Kim, S. U.; Oh, B. K.; Choi, J. W., Signal Enhancement of Surface Plasmon Resonance Based Immunosensor Using Gold Nanoparticle-Anti body Complex for beta-Amyloid (1-40) Detection. *Journal of Nanoscience and Nanotechnology* **2009**, 9, (12), 7155-7160.
93. Hayashida, M.; Yamaguchi, A.; Misawa, H., High sensitivity and large dynamic range surface plasmon resonance sensing for DNA hybridization using Au-nanoparticle-attached probe DNA. *Japanese Journal of Applied Physics Part 2-Letters & Express Letters* **2005**, 44, (50-52), L1544-L1546.
94. Yuan, J.; Oliver, R.; Aguilar, M. I.; Wu, Y. Q., Surface Plasmon Resonance Assay for Chloramphenicol. *Analytical Chemistry* **2008**, 80, (21), 8329-8333.
95. Rueda, A.; Stemmler, M.; Bauer, R.; Mullen, K.; Fogel, Y.; Kreiter, M., Optical resonances of gold nanoparticles on a gold surface: quantitative correlation of geometry and resonance wavelength. *New Journal of Physics* **2008**, 10.
96. Nordlander, P.; Le, F., Plasmonic structure and electromagnetic field enhancements in the metallic nanoparticle-film system. *Applied Physics B-Lasers and Optics* **2006**, 84, (1-2), 35-41.

97. Lyon, L. A.; Musick, M. D.; Smith, P. C.; Reiss, B. D.; Pena, D. J.; Natan, M. J., Surface plasmon resonance of colloidal Au-modified gold films. *Sensors and Actuators B-Chemical* **1999**, 54, (1-2), 118-124.
98. Choi, S. W.; Kim, H. S.; Kang, W. S.; Kim, J. H.; Cho, Y. J.; Kim, J. H., Sensitivity Enhancement by Au Nanoparticles in Surface Plasmon Resonance Chemical Sensors. *Journal of Nanoscience and Nanotechnology* **2008**, 8, (9), 4569-4573.
99. He, L.; Smith, E. A.; Natan, M. J.; Keating, C. D., The distance-dependence of colloidal Au-amplified surface plasmon resonance. *Journal of Physical Chemistry B* **2004**, 108, (30), 10973-10980.
100. Jung, J.; Na, K.; Lee, J.; Kim, K. W.; Hyun, J., Enhanced surface plasmon resonance by Au nanoparticles immobilized on a dielectric SiO<sub>2</sub> layer on a gold surface. *Analytica Chimica Acta* **2009**, 651, (1), 91-97.
101. Anker, J. N.; Hall, W. P.; Lyandres, O.; Shah, N. C.; Zhao, J.; Van Duyne, R. P., Biosensing with plasmonic nanosensors. *Nature Materials* **2008**, 7, (6), 442-453.
102. Ligler, F. S., Perspective on Optical Biosensors and Integrated Sensor Systems. *Analytical Chemistry* **2009**, 81, (2), 519-526.
103. Sepulveda, B.; Angelome, P. C.; Lechuga, L. M.; Liz-Marzan, L. M., LSPR-based nanobiosensors. *Nano Today* **2009**, 4, (3), 244-251.
104. Turkevich, J.; Stevenson, P. C.; Hillier, J., A Study of the Nucleation and Growth Processes in the Synthesis of Colloidal Gold. *Discussions of the Faraday Society* **1951**, 11, 55-75.
105. Zhang, Q. B.; Tan, Y. N.; Xie, J. P.; Lee, J. Y., Colloidal Synthesis of Plasmonic Metallic Nanoparticles. *Plasmonics* **2009**, 4, (1), 9-22.
106. Dahl, J. A.; Maddux, B. L. S.; Hutchison, J. E., Toward Greener Nanosynthesis. *Chemical Reviews* **2007**, 107, (6), 2228-2269.
107. Hirsch, L. R.; Jackson, J. B.; Lee, A.; Halas, N. J.; West, J., A whole blood immunoassay using gold nanoshells. *Analytical Chemistry* **2003**, 75, (10), 2377-2381.
108. Yu, C. X.; Irudayaraj, J., Multiplex biosensor using gold nanorods. *Analytical Chemistry* **2007**, 79, (2), 572-579.
109. Nath, N.; Chilkoti, A., Label Free Colorimetric Biosensing Using Nanoparticles. *Journal of Fluorescence* **2004**, 14, (4), 377-389.
110. Lee, S.; Mayer, K. M.; Hafner, J. H., Improved Localized Surface Plasmon Resonance Immunoassay with Gold Bipyramid Substrates. *Analytical Chemistry* **2009**, 81, (11), 4450-4455.

111. Arai, T.; Kumar, P. K. R.; Rockstuhl, C.; Awazu, K.; Tominaga, J., An optical biosensor based on localized surface plasmon resonance of silver nanostructured films. *Journal of Optics a-Pure and Applied Optics* **2007**, 9, (7), 699-703.
112. Kim, D. K.; Kerman, K.; Hiep, H. M.; Saito, M.; Yamamura, S.; Takamura, Y.; Kwon, Y. S.; Tamiya, E., Label-free optical detection of aptamer-protein interactions using gold-capped. *Analytical Biochemistry* **2008**, 379, (1), 1-7.
113. Vestergaard, M.; Kerman, K.; Kim, D. K.; Hiep, H. M.; Tamiya, E., Detection of Alzheimer's tau protein using localised surface plasmon resonance-based immunochip. *Talanta* **2008**, 74, (4), 1038-1042.
114. Dahlin, A.; Zach, M.; Rindzevicius, T.; Kall, M.; Sutherland, D. S.; Hook, F., Localized surface plasmon resonance sensing of lipid-membrane-mediated biorecognition events. *Journal Of The American Chemical Society* **2005**, 127, (14), 5043-5048.
115. Dahlin, A. B.; Chen, S.; Jonsson, M. P.; Gunnarsson, L.; Kalil, M.; Hol'ok, F., High-Resolution Microspectroscopy of Plasmonic Nanostructures for Miniaturized Biosensing. *Analytical Chemistry* **2009**.
116. Dahlin, A. B.; Tegenfeldt, J. O.; Hook, F., Improving the instrumental resolution of sensors based on localized surface plasmon resonance. *Analytical Chemistry* **2006**, 78, (13), 4416-4423.
117. Sherry, L. J.; Jin, R. C.; Mirkin, C. A.; Schatz, G. C.; Van Duyne, R. P., Localized surface plasmon resonance spectroscopy of single silver triangular nanoprisms. *Nano Letters* **2006**, 6, (9), 2060-2065.
118. Haes, A. J.; Van Duyne, R. P.; Zou, S. L.; Schatz, G. C., A nanoscale optical biosensor: The long range distance dependence of the localized surface plasmon resonance of noble metal nanoparticles. *Journal of Physical Chemistry B* **2004**, 108, (1), 109-116.
119. Haes, A. J.; Van Duyne, R. P.; Zou, S. L.; Schatz, G. C., Nanoscale optical biosensor: Short range distance dependence of the localized surface plasmon resonance of noble metal nanoparticles. *Journal of Physical Chemistry B* **2004**, 108, (22), 6961-6968.
120. Haes, A. J.; Chang, L.; Klein, W. L.; Van Duyne, R. P., Detection of a biomarker for Alzheimer's disease from synthetic and clinical samples using a nanoscale optical biosensor. *Journal of the American Chemical Society* **2005**, 127, (7), 2264-2271.
121. Larsson, E. M.; Alegret, J.; Kall, M.; Sutherland, D. S., Sensing characteristics of NIR localized surface plasmon resonances in gold nanorings for application as ultrasensitive biosensors. *Nano Letters* **2007**, 7, (5), 1256-1263.

122. Krishnan, S.; Weinman, C. J.; Ober, C. K., Advances in polymers for anti-biofouling surfaces. *Journal of Materials Chemistry* **2008**, 18, (29), 3405-3413.
123. Wisniewski, N.; Reichert, M., Methods for reducing biosensor membrane biofouling. *Colloids and Surfaces B: Biointerfaces* **2000**, 18, (3-4), 197-219.
124. Prime, K. L.; Whitesides, G. M., Adsorption of Proteins onto Surfaces Containing End-Attached Oligo(Ethylene Oxide) - a Model System Using Self-Assembled Monolayers. *Journal of the American Chemical Society* **1993**, 115, (23), 10714-10721.
125. Harder, P.; Grunze, M.; Dahint, R.; Whitesides, G. M.; Laibinis, P. E., Molecular conformation in oligo(ethylene glycol)-terminated self-assembled monolayers on gold and silver surfaces determines their ability to resist protein adsorption. *Journal of Physical Chemistry B* **1998**, 102, (2), 426-436.
126. Jung, L. S.; Nelson, K. E.; Campbell, C. T.; Stayton, P. S.; Yee, S. S.; Perez-Luna, V.; Lopez, G. P., Surface plasmon resonance measurement of binding and dissociation of wild-type and mutant streptavidin on mixed biotin-containing alkylthiolate monolayers. *Sensors and Actuators B-Chemical* **1999**, 54, (1-2), 137-144.
127. Baci, C. L.; Becker, J.; Janshoff, A.; Sonnichsen, C., Protein-membrane interaction probed by single plasmonic nanoparticles. *Nano Letters* **2008**, 8, (6), 1724-1728.
128. Chu, X.; Xiang, Z. F.; Fu, X.; Wang, S. P.; Shen, G. L.; Yu, R. Q., Silver-enhanced colloidal gold metalloimmunoassay for *Schistosoma japonicum* antibody detection. *Journal of Immunological Methods* **2005**, 301, (1-2), 77-88.
129. Gervais, T.; Jensen, K. F., Mass transport and surface reactions in microfluidic systems. *Chemical Engineering Science* **2006**, 61, (4), 1102-1121.
130. Dejardin, P.; Vasina, E. N., An accurate simplified data treatment for the initial adsorption kinetics in conditions of laminar convection in a slit: application to protein adsorption. *Colloids and Surfaces B-Biointerfaces* **2004**, 33, (2), 121-127.
131. Nair, P. R.; Alam, M. A., Performance limits of nanobiosensors. *Applied Physics Letters* **2006**, 88, (23).
132. Cui, Y.; Wei, Q. Q.; Park, H. K.; Lieber, C. M., Nanowire nanosensors for highly sensitive and selective detection of biological and chemical species. *Science* **2001**, 293, (5533), 1289-1292.
133. Gu, L. Q.; Braha, O.; Conlan, S.; Cheley, S.; Bayley, H., Stochastic sensing of organic analytes by a pore-forming protein containing a molecular adapter. *Nature* **1999**, 398, (6729), 686-690.

134. Besteman, K.; Lee, J. O.; Wiertz, F. G. M.; Heering, H. A.; Dekker, C., Enzyme-coated carbon nanotubes as single-molecule biosensors. *Nano Letters* **2003**, 3, (6), 727-730.
135. Bayley, H.; Martin, C. R., Resistive-pulse sensing - From microbes to molecules. *Chemical Reviews* **2000**, 100, (7), 2575-2594.
136. Curry, A.; Nusz, G.; Chilkoti, A.; Wax, A., Analysis of Total Uncertainty in Spectral Peak Measurements for Plasmonic Nanoparticle-Based Biosensors. *Applied Optics* **2007**, 46, (10), 1931-1939.
137. Mock, J. J.; Smith, D. R.; Schultz, S., Local refractive index dependence of plasmon resonance spectra from individual nanoparticles. *Nano Letters* **2003**, 3, (4), 485-491.
138. Kelly, K. L.; Coronado, E.; Zhao, L. L.; Schatz, G. C., The optical properties of metal nanoparticles: The influence of size, shape, and dielectric environment. *Journal of Physical Chemistry B* **2003**, 107, (3), 668-677.
139. Khlebtsov, N. G.; Trachuk, L. A.; Mel'nikov, A. G., The effect of the size, shape, and structure of metal nanoparticles on the dependence of their optical properties on the refractive index of a disperse medium. *Optics and Spectroscopy* **2005**, 98, (1), 77-83.
140. Zhu, J., Shape dependent full width at half maximum of the absorption band in gold nanorods. *Physics Letters A* **2005**, 339, (6), 466-471.
141. Link, S.; El-Sayed, M. A., Shape and size dependence of radiative, non-radiative and photothermal properties of gold nanocrystals. *International Reviews In Physical Chemistry* **2000**, 19, (3), 409-453.
142. Miller, M. M.; Lazarides, A. A., Sensitivity of metal nanoparticle surface plasmon resonance to the dielectric environment. *Journal Of Physical Chemistry B* **2005**, 109, (46), 21556-21565.
143. Prescott, S. W.; Mulvaney, P., Gold nanorod extinction spectra. *Journal of Applied Physics* **2006**, 99, (12).
144. Wax, A.; Sokolov, K., Molecular imaging and darkfield microspectroscopy of live cells using gold plasmonic nanoparticles. *Laser & Photonics Reviews* **2009**, 3, (1-2), 146-158.
145. Armani, A. M.; Kulkarni, R. P.; Fraser, S. E.; Flagan, R. C.; Vahala, K. J., Label-free, single-molecule detection with optical microcavities. *Science* **2007**, 317, (5839), 783-787.

146. Unger, A.; Rietzler, U.; Berger, R.; Kreiter, M., Sensitivity of Crescent-Shaped Metal Nanoparticles to Attachment of Dielectric Colloids. *Nano Letters* **2009**, 9, (6), 2311-2315.
147. Raschke, G.; Kowarik, S.; Franzl, T.; Sonnichsen, C.; Klar, T. A.; Feldmann, J.; Nichtl, A.; Kurzinger, K., Biomolecular recognition based on single gold nanoparticle light scattering. *Nano Letters* **2003**, 3, (7), 935-938.
148. Bally, M.; Halter, M.; Voros, J.; Grandin, H. M., Optical microarray biosensing techniques. *Surface and Interface Analysis* **2006**, 38, (11), 1442-1458.
149. Qavi, A. J.; Washburn, A. L.; Byeon, J. Y.; Bailey, R. C., Label-free technologies for quantitative multiparameter biological analysis. *Analytical and Bioanalytical Chemistry* **2009**, 394, (1), 121-135.
150. LaBaer, J.; Ramachandran, N., Protein microarrays as tools for functional proteomics. *Current Opinion in Chemical Biology* **2005**, 9, (1), 14-19.
151. Yeatman, E.; Ash, E. A., Surface-Plasmon Microscopy. *Electronics Letters* **1987**, 23, (20), 1091-1092.
152. Paul, S.; Vadgama, P.; Ray, A. K., Surface plasmon resonance imaging for biosensing. *Iet Nanobiotechnology* **2009**, 3, (3), 71-80.
153. Homola, J., Surface plasmon resonance sensors for detection of chemical and biological species. *Chemical Reviews* **2008**, 108, (2), 462-493.
154. Shumaker-Parry, J. S.; Aebersold, R.; Campbell, C. T., Parallel, quantitative measurement of protein binding to a 120-element double-stranded DNA array in real time using surface plasmon resonance microscopy. *Analytical Chemistry* **2004**, 76, (7), 2071-2082.
155. Spadavecchia, J.; Manera, M. G.; Quaranta, F.; Siciliano, P.; Rella, R., Surface plasmon resonance imaging of DNA based biosensors for potential applications in food analysis. *Biosensors & Bioelectronics* **2005**, 21, (6), 894-900.
156. Lee, H. J.; Goodrich, T. T.; Corn, R. M., SPR Imaging Measurements of 1-D and 2-D DNA Microarrays Created from Microfluidic Channels on Gold Thin Films. *Analytical Chemistry* **2001**, 73, (22), 5525-5531.
157. Lee, H. J.; Li, Y.; Wark, A. W.; Corn, R. M., Enzymatically amplified surface plasmon resonance imaging detection of DNA by exonuclease III digestion of DNA microarrays. *Analytical Chemistry* **2005**, 77, (16), 5096-5100.
158. Lee, H. J.; Nedelkov, D.; Corn, R. M., Surface plasmon resonance imaging measurements of antibody arrays for the multiplexed detection of low molecular weight protein biomarkers. *Analytical Chemistry* **2006**, 78, (18), 6504-6510.

159. Grosjean, L.; Cherif, B.; Mercey, E.; Roget, A.; Levy, Y.; Marche, P. N.; Villiers, M. B.; Livache, T., A polypyrrole protein microarray for antibody-antigen interaction studies using a label-free detection process. *Analytical Biochemistry* **2005**, 347, (2), 193-200.
160. Yuk, J. S.; Hong, D. G.; Jung, H. I.; Ha, K. S., Application of spectral SPR imaging for the surface analysis of C-reactive protein binding. *Sensors and Actuators B-Chemical* **2006**, 119, (2), 673-675.
161. Yuk, J. S.; Kim, H. S.; Jung, J. W.; Jung, S. H.; Lee, S. J.; Kim, W. J.; Han, J. A.; Kim, Y. M.; Ha, K. S., Analysis of protein interactions on protein arrays by a novel spectral surface plasmon resonance imaging. *Biosensors & Bioelectronics* **2006**, 21, (8), 1521-1528.
162. Piliarik, M.; Vaisocherova, H.; Homola, J., Towards parallelized surface plasmon resonance sensor platform for sensitive detection of oligonucleotides. *Sensors and Actuators B-Chemical* **2007**, 121, (1), 187-193.
163. Wong, C. L.; Ho, H. P.; Yu, T. T.; Suen, Y. K.; Chow, W. W. Y.; Wu, S. Y.; Law, W. C.; Yuan, W.; Li, W. J.; Kong, S. K.; Lin, C., Two-dimensional biosensor arrays based on surface plasmon resonance phase imaging. *Applied Optics* **2007**, 46, (12), 2325-2332.
164. Beusink, J. B.; Lokate, A. M. C.; Besselink, G. A. J.; Pruijn, G. J. M.; Schasfoort, R. B. M., Angle-scanning SPR imaging for detection of biomolecular interactions on microarrays. *Biosensors & Bioelectronics* **2008**, 23, (6), 839-844.
165. Liu, G. L.; Doll, J. C.; Lee, L. P., High-speed multispectral imaging of nanoplasmonic array. *Optics Express* **2005**, 13, (21), 8520-8525.
166. Bingham, J. M.; Willets, K. A.; Shah, N. C.; Andrews, D. Q.; Van Duyne, R. P., Localized Surface Plasmon Resonance Imaging: Simultaneous Single Nanoparticle Spectroscopy and Diffusional Dynamics. *Journal of Physical Chemistry C* **2009**, 113, (39), 16839-16842.
167. Tetz, K. A.; Pang, L.; Fainman, Y., High-resolution surface plasmon resonance sensor based on linewidth-optimized nanohole array transmittance. *Optics Letters* **2006**, 31, (10), 1528-1530.
168. Bardin, F.; Bellemain, A.; Roger, G.; Canva, M., Surface plasmon resonance spectro-imaging sensor for biomolecular surface interaction characterization. *Biosensors & Bioelectronics* **2009**, 24, (7), 2100-2105.
169. Dostalek, J.; Homola, J., Surface plasmon resonance sensor based on an array of diffraction gratings for highly parallelized observation of biomolecular interactions. *Sensors and Actuators B-Chemical* **2008**, 129, (1), 303-310.

170. Becker, J.; Schubert, O.; Sonnichsen, C., Gold nanoparticle growth monitored in situ using a novel fast optical single-particle spectroscopy method. *Nano Letters* **2007**, 7, (6), 1664-1669.
171. Curry, A.; Nusz, G.; Chilkoti, A.; Wax, A., Substrate effect on refractive index dependence of plasmon resonance for individual silver nanoparticles observed using darkfield micro-spectroscopy. *Optics Express* **2005**, 13, (7), 2668-2677.
172. Sonnichsen, C.; Geier, S.; Hecker, N. E.; von Plessen, G.; Feldmann, J.; Dittbacher, H.; Lamprecht, B.; Krenn, J. R.; Aussenegg, F. R.; Chan, V. Z. H.; Spatz, J. P.; Moller, M., Spectroscopy of single metallic nanoparticles using total internal reflection microscopy. *Applied Physics Letters* **2000**, 77, (19), 2949-2951.
173. Schultz, D. A.; Mock, J. J.; Schultz, S.; Smith, D. R., Single-target molecule detection with nonbleaching multicolor optical immunolabels. *Proceedings of the National Academy of Sciences of the United States of America* **2000**, 97, (3), 996-1001.
174. Curry, A.; Hwang, W. L.; Wax, A., Epi-illumination through the microscope objective applied to darkfield imaging and microspectroscopy of nanoparticle interaction with cells in culture. *Optics Express* **2006**, 14, (14), 6535-6542.
175. Curry, A. C.; Crow, M.; Wax, A., Molecular imaging of epidermal growth factor receptor in live cells with refractive index sensitivity using dark-field microspectroscopy and immunotargeted nanoparticles. *Journal of Biomedical Optics* **2008**, 13, (1).
176. Rodriguez-Fernandez, J.; Novo, C.; Myroshnychenko, V.; Funston, A. M.; Sanchez-Iglesias, A.; Pastoriza-Santos, I.; Perez-Juste, J.; de Abajo, F. J. G.; Liz-Marzan, L. M.; Mulvaney, P., Spectroscopy, Imaging, and Modeling of Individual Gold Decahedra. *Journal of Physical Chemistry C* **2009**, 113, (43), 18623-18631.
177. Yguerabide, J.; Yguerabide, E. E., Light-scattering submicroscopic particles as highly fluorescent analogs and their use as tracer labels in clinical and biological applications - I. Theory. *Analytical Biochemistry* **1998**, 262, (2), 137-156.
178. Chumanov, G.; Sokolov, K.; Gregory, B. W.; Cotton, T. M., Colloidal Metal Films as a Substrate for Surface-Enhanced Spectroscopy. *Journal of Physical Chemistry* **1995**, 99, (23), 9466-9471.
179. Nikoobakht, B.; El-Sayed, M. A., Preparation and Growth Mechanism of Gold Nanorods (NRs) Using Seed-Mediated Growth Method. *Chemistry of Materials* **2003**, 15, (10), 1957-1962.

180. Hafner, J. H.; Nehl, C. L.; Grady, N. K.; Goodrich, G. P.; Tam, F.; Halas, N. J., Scattering Spectra of Single Gold Nanoshells. *Nano Letters* **2004**, 4, (12), 2355-2359.
181. Lee, K. S.; El-Sayed, M. A., Dependence of the enhanced optical scattering efficiency relative to that of absorption for gold metal nanorods on aspect ratio, size, end-cap shape, and medium refractive index. *Journal of Physical Chemistry B* **2005**, 109, (43), 20331-20338.
182. Chilkoti, A.; Stayton, P. S., Molecular-Origins of the Slow Streptavidin-Biotin Dissociation Kinetics. *Journal of the American Chemical Society* **1995**, 117, (43), 10622-10628.
183. Stayton, P. S.; Freitag, S.; Klumb, L. A.; Chilkoti, A.; Chu, V.; Penzotti, J. E.; To, R.; Hyre, D.; Le Trong, I.; Lybrand, T. P.; Stenkamp, R. E., Streptavidin-biotin binding energetics. *Biomolecular Engineering* **1999**, 16, (1-4), 39-44.
184. Evanoff, D. D.; White, R. L.; Chumanov, G., Measuring the distance dependence of the local electromagnetic field from silver nanoparticles. *Journal of Physical Chemistry B* **2004**, 108, (5), 1522-1524.
185. Stenberg, E.; Persson, B.; Roos, H.; Urbaniczky, C., Quantitative determination of surface concentration of protein with surface plasmon resonance using radiolabeled proteins. *Journal of Colloid and Interface Science* **1991**, 143, (2), 513-526.
186. Vollmer, F.; Braun, D.; Libchaber, A.; Khoshsima, M.; Teraoka, I.; Arnold, S., Protein detection by optical shift of a resonant microcavity. *Applied Physics Letters* **2002**, 80, (21), 4057-4059.
187. Chen, C.-D.; Cheng, S.-F.; Chau, L.-K.; Wang, C. R. C., Sensing capability of the localized surface plasmon resonance of gold nanorods. *Biosensors & Bioelectronics* **2007**, 22, 926-932.
188. Jana, N. R.; Gearheart, L.; Murphy, C. J., Wet Chemical Synthesis of High Aspect Ratio Cylindrical Gold Nanorods. *Journal of Physical Chemistry B* **2001**, 105, (19), 4065-4067.
189. Busbee, B. D.; Obare, S. O.; Murphy, C. J., An Improved Synthesis of High-Aspect-Ratio Gold Nanorods. *Advanced Materials* **2003**, 15, (5), 414-416.
190. Sau, T. K.; Murphy, C. J., Room temperature, high-yield synthesis of multiple shapes of gold nanoparticles in aqueous solution. *Journal Of The American Chemical Society* **2004**, 126, (28), 8648-8649.
191. Link, S.; Mohamed, M. B.; El-Sayed, M. A., Simulation of the Optical Absorption Spectra of Gold Nanorods as a Function of Their Aspect Ratio and the Effect of

- the Medium Dielectric Constant. *Journal of Physical Chemistry B* **1999**, 103, (16), 3073-3077.
192. Weissleder, R., A Clearer Vision for *in vivo* Imaging. *Nature Biotechnology* **2001**, 19, (4), 316-317.
193. Jackson, J. B.; Westcott, S. L.; Hirsch, L. R.; West, J. L.; Halas, N. J., Controlling the surface enhanced Raman effect via the nanoshell geometry. *Applied Physics Letters* **2003**, 82, (2), 257-259.
194. Hanarp, P.; Kall, M.; Sutherland, D. S., Optical properties of short range ordered arrays of nanometer gold disks prepared by colloidal lithography. *Journal of Physical Chemistry B* **2003**, 107, (24), 5768-5772.
195. Aizpurua, J.; Hanarp, P.; Sutherland, D. S.; Kall, M.; Bryant, G. W.; de Abajo, F. J. G., Optical properties of gold nanorings. *Physical Review Letters* **2003**, 90, (5).
196. Novo, C.; Gomez, D.; Perez-Juste, J.; Zhang, Z. Y.; Petrova, H.; Reismann, M.; Mulvaney, P.; Hartland, G. V., Contributions from radiation damping and surface scattering to the linewidth of the longitudinal plasmon band of gold nanorods: a single particle study. *Physical Chemistry Chemical Physics* **2006**, 8, (30), 3540-3546.
197. Kuwata, H.; Tamaru, H.; Esumi, K.; Miyano, K., Resonant light scattering from metal nanoparticles: Practical analysis beyond Rayleigh approximation. *Applied Physics Letters* **2003**, 83, (22), 4625-4627.
198. Xu, X. D.; Cortie, M. B., Shape change and color gamut in gold nanorods, dumbbells, and dog bones. *Advanced Functional Materials* **2006**, 16, (16), 2170-2176.
199. Yan, B. H.; Yang, Y.; Wang, Y. C., Comment on "Simulation of the optical absorption spectra of gold nanorods as a function of their aspect ratio and the effect of the medium dielectric constant". *Journal of Physical Chemistry B* **2003**, 107, (34), 9159-9159.
200. Link, S.; El-Sayed, M. A.; Mohamed, M. B., Simulation of the optical absorption spectra of gold nanorods as a function of their aspect ratio and the effect of the medium dielectric constant (vol 103B, pg 3073, 1999). *Journal of Physical Chemistry B* **2005**, 109, (20), 10531-10532.
201. Whitney, A. V.; Elam, J. W.; Zou, S. L.; Zinovev, A. V.; Stair, P. C.; Schatz, G. C.; Van Duyne, R. P., Localized surface plasmon resonance nanosensor: A high-resolution distance-dependence study using atomic layer deposition. *Journal of Physical Chemistry B* **2005**, 109, (43), 20522-20528.
202. Gans, R., The shape of ultra microscopic gold particles. *Annalen Der Physik* **1912**, 37, (5), 881-900.

203. Mie, G., Beiträge zur Optik trüber Medien, speziell kolloidaler Metallösungen. *Ann. Physik* **1908**, 25, 377-445.
204. Hicks, E. M.; Zhang, X. Y.; Zou, S. L.; Lyandres, O.; Spears, K. G.; Schatz, G. C.; Van Duyne, R. P., Plasmonic properties of film over nanowell surfaces fabricated by nanosphere lithography. *Journal Of Physical Chemistry B* **2005**, 109, (47), 22351-22358.
205. Miller, M. M.; Lazarides, A. A., Sensitivity of metal nanoparticle plasmon resonance band position to the dielectric environment as observed in scattering. *Journal of Optics a-Pure and Applied Optics* **2006**, 8, (4), S239-S249.
206. Neish, C. S.; Martin, I. L.; Henderson, R. M.; Edwardson, J. M., Direct visualization of ligand-protein interactions using atomic force microscopy. *British Journal of Pharmacology* **2002**, 135, (8), 1943-1950.
207. Chien, F. C.; Chen, S. J., Direct determination of the refractive index and thickness of a bilayer based on coupled waveguide-surface plasmon resonance mode. *Optics Letters* **2006**, 31, (2), 187-189.
208. Weber, P. C.; Ohlendorf, D. H.; Wendoloski, J. J.; Salemme, F. R., Structural Origins of High-Affinity Biotin Binding to Streptavidin. *Science* **1989**, 243, (4887), 85-88.
209. Hendrickson, W. A.; Pahler, A.; Smith, J. L.; Satow, Y.; Merritt, E. A.; Phizackerley, R. P., Crystal-Structure of Core Streptavidin Determined from Multiwavelength Anomalous Diffraction of Synchrotron Radiation. *Proceedings of the National Academy of Sciences of the United States of America* **1989**, 86, (7), 2190-2194.
210. Hinrichsen, E. L.; Feder, J.; Jossang, T., Geometry of Random Sequential Adsorption. *Journal of Statistical Physics* **1986**, 44, (5-6), 793-827.
211. Jung, L. S.; Nelson, K. E.; Stayton, P. S.; Campbell, C. T., Binding and dissociation kinetics of wild-type and mutant streptavidins on mixed biotin-containing alkylthiolate monolayers. *Langmuir* **2000**, 16, (24), 9421-9432.
212. Kim, Y. P.; Hong, M. Y.; Kim, J.; Oh, E.; Shon, H. K.; Moon, D. W.; Kim, H. S.; Lee, T. G., Quantitative analysis of surface-immobilized protein by TOF-SIMS: Effects of protein orientation and trehalose additive. *Analytical Chemistry* **2007**, 79, (4), 1377-1385.
213. Link, S.; El-Sayed, M. A., Spectroscopic determination of the melting energy of a gold nanorod. *Journal of Chemical Physics* **2001**, 114, (5), 2362-2368.
214. Chang, S. S.; Shih, C. W.; Chen, C. D.; Lai, W. C.; Wang, C. R. C., The shape transition of gold nanorods. *Langmuir* **1999**, 15, (3), 701-709.

215. Muskens, O. L.; Bachelier, G.; Del Fatti, N.; Vallee, F.; Brioude, A.; Jiang, X. C.; Pileni, M. P., Quantitative absorption spectroscopy of a single gold nanorod. *Journal of Physical Chemistry C* **2008**, 112, (24), 8917-8921.
216. Beeram, S. R.; Zamborini, F. P., Selective Attachment of Antibodies to the Edges of Gold Nanostructures for Enhanced Localized Surface Plasmon Resonance Biosensing. *Journal of the American Chemical Society* **2009**, 131, (33), 11689-+.
217. Frank Jeyson, H.; Srujan Kumar, D.; Ozalp, V. C.; Alessandro, P.; Ciara, K. O. S.; Thomas, A. K.; Ioannis, K., Label free optical sensor for Avidin based on single gold nanoparticles functionalized with aptamers. *Journal of Biophotonics* **2009**, 2, (4), 227-231.
218. Hardeberg, J. Y.; Schmitt, F.; Brettel, H., Multispectral color image capture using a liquid crystal tunable filter. *Optical Engineering* **2002**, 41, (10), 2532-2548.
219. Mejac, I.; Bryan, W. W.; Lee, T. R.; Tran, C. D., Visualizing the Size, Shape, Morphology, and Localized Surface Plasmon Resonance of Individual Gold Nanoshells by Near-Infrared Multispectral Imaging Microscopy. *Analytical Chemistry* **2009**.
220. Zhou, G. Y.; Cheo, K. K. L.; Du, Y.; Chau, F. S.; Feng, H. H.; Zhang, Q. X., Hyperspectral imaging using a microelectricalmechanical-systems-based in-plane vibratory grating scanner with a single photodetector. *Optics Letters* **2009**, 34, (6), 764-766.
221. Nieves, J. L.; Valero, E. M.; Hernandez-Andres, J.; Romero, J., Recovering fluorescent spectra with an RGB digital camera and color filters using different matrix factorizations. *Applied Optics* **2007**, 46, (19), 4144-4154.
222. Schief, W. R.; Edwards, T.; Frey, W.; Koppenol, S.; Stayton, P. S.; Vogel, V., Two-dimensional crystallization of streptavidin: in pursuit of the molecular origins of structure, morphology, and thermodynamics. *Biomolecular Engineering* **1999**, 16, (1-4), 29-38.
223. Heidary, K.; Caulfield, H. J., Spectral sensitivity design for maximum colour separation in artificial colour systems. *Int Image Processing* **2009**, 3, (3), 135-146.
224. Nelson, M. P.; Aust, J. F.; Dobrowolski, J. A.; Verly, P. G.; Myrick, M. L., Multivariate optical computation for predictive spectroscopy. *Analytical Chemistry* **1998**, 70, (1), 73-82.
225. Gehm, M. E.; John, R.; Brady, D. J.; Willett, R. M.; Schulz, T. J., Single-shot compressive spectral imaging with a dual-disperser architecture. *Optics Express* **2007**, 15, (21), 14013-14027.

226. Cull, C. F.; Choi, K.; Brady, D. J.; Oliver, T., Identification of fluorescent beads using a coded aperture snapshot spectral imager. *Appl. Opt.* 49, (10), B59-B70.
227. Guizar-Sicairos, M.; Thurman, S. T.; Fienup, J. R., Efficient subpixel image registration algorithms. *Opt. Lett.* **2008**, 33, (2), 156-158.
228. O'Haver, T. *Peak finding and measurement*, 2; <http://www.mathworks.com/matlabcentral/fileexchange/11755>; 2009.
229. Cao, Y. W.; Jin, R.; Mirkin, C. A., DNA-modified core-shell Ag/Au nanoparticles. *Journal of the American Chemical Society* **2001**, 123, (32), 7961-7962.
230. Unger, A.; Kreiter, M., Analyzing the Performance of Plasmonic Resonators for Dielectric Sensing. *Journal of Physical Chemistry C* **2009**, 113, (28), 12243-12251.
231. Ma, W. Y.; Yang, H.; Hilton, J. P.; Lin, Q.; Liu, J. Y.; Huang, L. X.; Yao, J., A numerical investigation of the effect of vertex geometry on localized surface plasmon resonance of nanostructures. *Opt. Express* 18, (2), 843-853.
232. Hucknall, A.; Kim, D. H.; Rangarajan, S.; Hill, R. T.; Reichert, W. M.; Chilkoti, A., Simple Fabrication of Protein Microarrays on Non-fouling Polymer Brushes With Femtomolar Sensitivity in Serum and Blood. *Advanced Materials* **2009**, *In Press*.
233. Hucknall, A.; Rangarajan, S.; Chilkoti, A., In pursuit of zero: polymer brushes that resist the adsorption of proteins. *Advanced Materials* **2009**, *In Press*.

## Biography

The world was first introduced to Gregory John Nusz on Tuesday September 16, 1980 in Buffalo, New York. Greg joined his older brother Jeff as the second failure in Tom and Elaine's quest for a daughter. A penchant for sunshine and fair weather brought the four to Denver where a third attempt was made at daughterly bliss. Alas - bad news comes in threes - and Danny was born. Elaine and her four boys moved to Hockessin, DE in 1986 where she was finally convinced that no matter how joyous a daughter might be, the risk of another boy was far too great. Greg grew up in Hockessin playing soccer, camping with the family, riding bikes with his posse, gallivanting in the forest behind the house and generally doing a moderately good job at staying out of trouble. A formative point in this time occurred at age 13 when Greg traveled with his soccer team to compete in a tournament in Copenhagen, Denmark. Upon routing the defending champion team from Sweden, coach Henry Fusco of the Kirkwood Power filled the championship trophy with beer - encouraging each player to have a drink in order of increasing height. Being the tallest lad on the team, Greg drank last and finished the cup - the final swallow cementing his love affair with soccer, with international travel and with beer.

Greg graduated Alexis I. duPont High School as a member of the 400-strong class of 1998. Greg was a proud trumpet player in the marching band, captain of the soccer team and received the class scholar-athlete award (primarily because his more scholarly, athletic friend Darin received the State award and was thus ineligible for the class award). Greg did not graduate as a member of the National Honors Society

because of a "permanent record" blemished by a three day suspension resulting from a fist-fight over a seat at a lunch table in the school cafeteria.

North Carolina State University received Greg as a Caldwell scholarship-supported double major in Mathematics and Math Education in the fall of 1998. Five years in Raleigh and six months backpacking in Australia later, Greg graduated with a 4.0 GPA with BS degrees in both Physics and Mathematics in the Spring of 2003 and published a peer-reviewed journal article on a biophysics project he had been conducting in a faculty optics lab under the guidance of professor Hans Hallen. Also in this time, Greg worked as an intern at the Space and Naval Warfare Research Lab in San Diego, California. While there, he labored on a secret government research project that will never work. He also came upon the realization that the U.S. government employs many semi-competent people focused on figuring out more efficient ways at blowing people up and that they don't need his help too.

After exploring each mile of Interstate 95 during the remainder of 2003, Greg focused his attention on finding more humane applications of technology. He serendipitously contacted Professor Ashutosh Chilkoti of Duke University who filled him in on the field of Biomedical Engineering and offered him a position as a graduate student investigating diagnostic applications of nanomaterials (a subject which the reader, by now, is presumably well acquainted). In his time at Duke, Greg was awarded a Chambers Fellowship for photonics research, and authored or co-authored five peer-reviewed articles, two-book chapters and one bad-ass thesis. Greg also received numerous poster and presentation awards from the three international and seven domestic conferences he was fortunate enough to attend. Also during his tenure as a graduate student, Greg spent six months in New Zealand fulfilling his required obligation

to complete an industrial internship required for his certification by the Center for Biomolecular and Tissue Engineering (Greg does not know anything about biomolecular or tissue engineering). His time completing the internship consisted partly of working for a biomedical device company (that got its big start generating computer models for Lord of the Rings characters), and partly backpacking, rock climbing and otherwise adventuring.

After graduation, Greg intends to scour the planet with partner Josie Bamford, and together they will heal the ails of the world – one medical device and one environmental impact assessment at a time. They will do this armed with bleeding-heart tendencies, youthful dedication, over-optimistic perspectives, and a smidge of good luck.